Marine and terrestrial influence on submarine groundwater discharge in coastal waters connected to a peatland

Dissertation
for the award of the degree
"Doctor rerum naturalium" (Dr.rer.nat.)

of the Georg-August-Universität Göttingen
within the doctoral program Geoscience
of the Georg-August University School of Science (GAUSS)
submitted by

Miriam Ibenthal

from Werne

Göttingen, 2019

Thesis Committee

Prof. Dr.-Ing. Thomas Ptak, Dept. Applied Geology, Geoscience Centre, University of Göttingen

Dr. Manon Janssen, Soil Physics, University of Rostock

Prof. Dr. Gudrun Massmann, Hydrogeology and Landscape Hydrology, University of Oldenburg

Members of the Examination Board

Reviewer: Prof. Dr.-Ing. Thomas Ptak, Dept. Applied Geology, Geoscience Centre, University of Göttingen

Second Reviewer: Prof. Dr. Gudrun Massmann, Hydrogeology and Landscape Hydrology, University of Oldenburg

Further members of the Examination Board:

Dr. Manon Janssen, Soil Physics, University of Rostock

Prof. Dr. Martin Sauter, Dept. Applied Geology, Geoscience Centre, University of Göttingen

Prof. Dr. Hans Ruppert, Dept. Sedimentology / Environmental Geology

Dr. Matthias Franz, Dept. Applied Geology, Geoscience Centre, University of Göttingen

Date of the oral examination: .....

Declaration of Authorship

I, Miriam Ibenthal, declare that this thesis titled, "Marine and terrestrial influence on submarine groundwater discharge in coastal waters connected to a peatland" and the work presented in it are my own. I confirm that:

- This work was done wholly or mainly while in candidature for a research degree at this University.
- Where any part of this thesis has previously been submitted for a degree or any other qualification at this University or any other institution, this has been clearly stated.
- Where I have consulted the published work of others, this is always clearly attributed.
- Where I have quoted from the work of others, the source is always given. With the exception of such quotations, this thesis is entirely my own work.
- I have acknowledged all main sources of help.
- Where the thesis is based on work done by myself jointly with others, I have made clear exactly what was done by others and what I have contributed myself.
- None of this work has been published before submission.

Signed:

Date:

Acknowledgements

First, I would like to thank my supervisors Manon Janssen, Thomas Ptak and Gudrun Massmann for the support and valuable discussions throughout the PhD.

I thank Robert Schmidtke, Christian Criegee, Bassel Sawaf, Alexander Riedel, Karl Ludwig Körber, Bosse Frithjof Ritschl, Fabian Beimowski, Anne Breznikar, Lennart Gosch, Julia Westphal and Matthias Kreuzburg for their exceptional help under often hard conditions in the field and Florence Christiansen, Maria Lipski and Anne Breznikar for their help and work in the lab. I further thank Mechthild Rittmeier, Evelyn Bolzmann, Stefan Köhler and Elena Heilmann for laboratory analyses.

I thank Jürgen Sültenfuß, Janek Greskowiak, Uli Maier, Jannes Kordilla and Tobias Licha for more valuable discussions.

I thank the members of Baltic TRANSCOAST and the Soil Physics working group for a wonderful time in Rostock.

In Göttingen I want to thank the members of the Applied Geology Department for providing a good work environment for the completion of this thesis.

I am most grateful for the support of my family and friends throughout the years in many aspects of life. I am more than thankful to Andrés for his motivation, patience, and humour.

Summary

In low-lying coastal fens, groundwater flow direction, water level and input of salts with seawater determine vegetation communities and greenhouse gas emissions, while the export of nutrients and carbon with submarine groundwater discharge influences biogeochemical processes in the shallow coastal sediments. Anthropogenic interferences like drainage and diking have strong impacts on water flow. This thesis aimed at an understanding of the hydro(geo)logical system in a rewetted coastal fen typical for the southern Baltic Sea, and its changes from the pristine state over phases of moderate and intensive drainage towards rewetting with implications for biogeochemical processes. The drivers and effects of short-term (weather-induced) and long-term (hydrological interferences) processes were differentiated and their importance for flow and transport identified.

Groundwater observation wells were installed both in the peat and underlying sand, and continuous readings of water level and electrical conductivity were combined with groundwater dating and analysis of the water composition (major ions, nutrients and carbon). Based on sediment cores, grain size analysis and hydraulic slug tests, a 3D numerical groundwater flow model was developed to investigate varying short-term and long-term groundwater flow patterns. Combined with analysed water composition, the consequences for transport and biogeochemistry in the peatland and at the coastal interface were estimated.

On the landside, the peat thickness, depth of ditches and their resulting hydraulic connectivity to the underlying aquifer, as well as the geometry of the aquifer, defined discharge zones of upwelling groundwater from the larger catchment as well as recharge zones. Long-term moderate and intensive drainage led to enhanced upwelling from an ancient glacial river valley with possible effects for local biogeochemistry.

The hydraulic state of the peatland and the confining outcropping peat defined the hydraulic gradient towards the sea with consequences for origin, location and amount of submarine groundwater discharge (SGD). SGD consisted mainly of recirculating seawater, followed by fresh SGD from a dune dike, and of nutrient-enriched water from the aquifer below the outcropping peat.

A transient simulation identified short-term vertical flow reversals in the peat on land and offshore with implications for dispersive mixing of different water sources. Flow was driven by variations in evapotranspiration, recharge and surface water discharge on the landside. Offshore, hydraulic head differences between the peatland and the Baltic Sea defined the flow direction. In the long-term, the

dominant flow direction, and hence the water source, depends on the hydrological state of the peatland and the mean sea level.

The results suggest that both long-term and short-term drivers for groundwater flow must be considered to explain biogeochemical patterns. The knowledge of the anthropogenic history, peat degradation, and aquifer geometry – especially in heterogeneous glacial deposits – is crucial to estimate the influence of different water sources on ecosystem functioning both on land- and seaside.

Content

List of figures

List of tables

1 Introduction

1.1 Motivation

1.1.1 Peatlands: carbon cycling and dependency on hydrological state

Peatlands are important carbon sinks. Peatlands of the northern hemisphere cover 3 % of the land surface and store 30% of the land-based organic carbon (Gorham 1995, Limpens et al. 2008). Undisturbed, pristine peatlands are a net CO_2 sink and produce CH_4, but in the long-term have the potential to attenuate global warming (Whiting and Chanton 2001). Peatlands have been drained extensively for agricultural purposes, forestry or peat excavation (Joosten 1997). The drainage and associated aeration have resulted in increased CO_2-emissions (Erkens et al. 2016), peat compaction and land subsidence (Whittington and Price 2006), and loss in ecological diversity (Joosten et al. 2017, Vasander et al. 2003).

Knowledge of the groundwater flow regime is essential for the success of peatland restoration. The sources of water - groundwater or rainwater - define the ecological state of a peatland (e.g. Ivanov 1981, Succow and Joosten 2001, Wassen 1996). The groundwater flow direction and hereby vertical water movement have a major impact on the distribution of water compounds and carbon cycling (Waddington and Roulet 1997). Changes in the hydrological regime and a lowering of the water table due to drainage can alter water flow pathways, water composition and vegetation patterns (Siegel and Glaser 1987, van Loon et al. 2009, Kopp et al. 2013). Drainage causes degradation of the peat, which involves a decrease in pore size and a strong reduction of the hydraulic conductivity (Hallema et al. 2015, Tiemeyer et al. 2017), leading to irreversible changes in the hydraulic properties of peat and stronger water table fluctuations (Whittington and Price 2006).

1.1.2 Coastal peatlands: influence of inundating seawater

Coastal peatlands are unique ecosystems at the transition zone of fresh to saltwater. Along the German Baltic coast an area of 1800 km^2 of wetland adjoins the sea (Sterr 2008). The socio-economical value of coastal peatlands as flood retention areas and carbon sinks has been recognised and restoring peatlands thus has become an important measure.

In coastal peatlands inundating seawater is a further important water source, which is assumed to gain importance in the future with a rising sea level (Grinsted et al. 2015). The input of salts alters the export of dissolved organic carbon (DOC) (Ardón et al. 2016, Gosch et al. 2018) and nutrients from the peat (Ardón et al. 2013, van Dijk et al. 2015) and impacts on greenhouse gas emissions (Chambers et al. 2011 Helton et al. 2014, Hahn et al. 2015, Koebsch et al. 2019). The enhanced sulphate concentrations are of special importance both in increasing nutrient leaching (Lamers et al. 1998, Helton et al. 2014) and in reducing methane emissions (Koebsch et al. 2019). Further, a flooding with saltwater after decades of drainage and isolation from the sea might lead to an increased leaching of nitrogen (mainly ammonium, NH_4^+) and a decrease of DOC and phosphate (PO_4^{3-}) release rates (Lennartz and Liu 2019).

1.1.3 Impact of submarine groundwater discharge on biogeochemical processes

The adjacent sea may receive water from a coastal peatland by surface water discharge and in the form of submarine groundwater discharge (SGD). SGD is defined as the total amount of water discharging from the seabed to the open sea (Burnett et al. 2003) and is a well-known phenomenon for the transport of land-derived solutes that mix with recirculating seawater (Moore 1999, Burnett et al. 2003). The mixture of land-derived groundwater and seawater rich in solutes and organic matter in the coastal sediments with involved microbial activity lead to a release of nutrients, trace gases, e.g. N_2O and CH_4 (Schutte et al. 2016, 2015), carbon

and metals (Moore 1999, Porubsky et al. 2014). Although SGD is diffusive and low in most areas, it is widely distributed and therefore can have an overall impact (Burnett et al. 2003).

In coastal peatlands the outwash of nutrients, carbon-solutes and other compounds with groundwater can influence the ecosystem in the shallow sea. Despite shallow hydraulic gradients an influence is expected due to potentially high loads of solutes from peat. Low freshwater SGD is associated with increased groundwater residence time and a larger dispersion zone, where fresh- and saltwater mixes (Smith 2004). This also increases the time for biogeochemical reactions (Robinson et al. 2007a, Post et al. 2013). For example, the solutes (nutrients, dissolved inorganic carbon (DIC), DOC, trace gases) in the groundwater of the Okatee River estuary (South Carolina) have shown to vary due to differences in microbial sulphate reduction, organic matter supply and groundwater residence time (Porubsky et al. 2014). Besides complex biogeochemical transformations a proper understanding of physical drivers of groundwater flow at the coastal interface is necessary to estimate mass fluxes to the oceans (Robinson et al. 2018).

1.1.4 Drivers for submarine groundwater discharge

Physically SGD is driven by the advective force of fresh groundwater discharge and buoyancy effects depending on density differences to the recirculating seawater, leading to dispersion and convective flow in the saltwater wedge (Cooper 1959, Smith 2004). Recirculating seawater is driven by waves, wind, and sea level fluctuations, e.g. tides (Burnett et al. 2003). These pressure-induced changes can lead to advective pore water fluxes into a permeable seabed with effects for biogeochemical reactions (Huettel et al. 1998). Coastal interfaces are complex hydrogeological systems as the coast is exposed to strong wind and ocean currents resulting in erosion and sedimentation. This shapes the extent of aquifers and confining units within the seabed with implications for the extent of land-derived groundwater offshore (Kooi and Groen 2001). Only few studies consider both alongshore and cross shore heterogeneity (Robinson et al. 2018). Russoniello et al.

(2013) demonstrated the effect of a varying extent of mud and peat layers offshore on the spatial distribution of SGD. Further, the landside hydro(geo)logical conditions affecting SGD are also site-specific as they may differ depending on the geology, topography, climate, land-cover and human interferences (e.g. Michael et al. 2005, Robinson et al. 2018).

1.1.5 Evaluation of groundwater flow through numerical modelling

3D numerical groundwater flow models give insights to the influence of geological heterogeneity and changing boundary conditions on groundwater flow paths and fluxes. Simulation of local and regional groundwater flow in peatlands helped to understand relevant flow processes impacting on solute distribution like enhanced recharge of rainwater during drainage (van Loon et al. 2009), but also enhanced upward flow and transition of bog to fen-type (Kopp et al. 2013), spatial distribution of recharge and discharge areas (Åberg et al. 2019), dispersive mixing as a driver for vertical transport during lateral flow (Reeve et al. 2001), the influence of recharge, evapotranspiration (Reeve et al. 2006) and hydraulic conductivity of the peat and underlying sediment (Reeve et al. 2000), as well as the storage capacity of peat (Reeve et al. 2006), on vertical flow.

Numerous numerical studies concerning the drivers for variable density groundwater flow at the coastal interface exist (e.g. Greskowiak 2014, Robinson et al. 2007a, 2007b, Röper et al. 2015).

Numerical studies considering the connectivity of coastal peatlands to the sea and different hydrological stages in time, combined with field investigations, are scarce.

1.1.6 Problem statement at a specific site

In this thesis a rewetted degraded coastal fen is considered, where both the ground- and the surface water (via a ditch system) is hydraulically connected to the Baltic Sea. The hydrological system (Bohne and Bohne 2008, Miegel et al. 2016, 2017, Selle et al. 2016), CH_4 and CO_2 emissions following rewetting (Koebsch et al. 2013a, b,

2015, 2019, Hahn et al. 2015), and local vegetation succession due to seasonal water table changes (Koch et al. 2017) are well-studied. However, local differences in geochemical composition in the peat and pore water (Koebsch et al. 2019), the varying thickness of the peat layer (Kolp 1975, Dahms 1991, Krüger 1995) and its extent into the Baltic Sea (Kreuzburg et al. 2018) associated with locally enhanced CH_4 emissions offshore (Jurasinski et al. 2018) suggest a complex and heterogeneous geological system with implications for groundwater flow, transport, and biogeochemical processes. Little is known about the groundwater flow field and water quality in the shallow aquifer below the peat with relevance for the near-surface processes described above.

1.2 Objectives

The overall objective of the thesis is to assess the degree of interaction of a coastal fen with the Baltic Sea through surface- and groundwater flow paths and identify the relevance for solute transport. In understanding the functioning of one exemplary groundwater flow system and identifying the major parameters and processes involved, the relevance of low-lying coastal groundwater flow systems under changing hydrological conditions for biogeochemical processes can be assessed. With respect to the long history of different hydrological stages of the investigated fen the main research questions were:

- On what timescales are what kind of processes relevant for groundwater flow?
- What is the influence of spatial hydrological and geological heterogeneity on groundwater flow?
- How does SGD differ on a short and long-term scale and where does it occur?

The steps to answer these questions were:

- Development of hypotheses of changes in the groundwater flow system from a pristine state following (intensive) drainage, rewetting, and sea level rise in the future (Chapter 3), partly based on:
- Assessment of the hydrogeological situation in the peatland and at the coast today through geological investigation, water level recordings, steady-state (long-term effects) and transient (short-term effects) numerical modelling (Chapter 3, 4 and 5)
- Identification of the influence of intensive drainage and recent rewetting on today's water composition and flow paths in the peatland through tritium-helium groundwater dating and groundwater flow modelling (Chapter 3, 5)
- Identification of (hydro-)geological heterogeneities to explain spatial variations in groundwater composition (Chapter 3, 5)

- Testing of the hypotheses (pristine, drained and rewetted) through scenario simulations of the distinct hydrological stages (Chapter 5)

1.3 Structure of the thesis

Chapter 1 introduced the motivation and objectives of this study.

Chapter 2 describes briefly the hydrological and geological features, as well as the history of the investigated site.

Chapter 3 is part of a manuscript (Ibenthal, M., Ptak, T., Massmann, G., Sültenfuß, J., Janssen, M.: "Groundwater flow in a coastal fen exposed to drainage, rewetting and interaction with the Baltic Sea") and characterizes the hydrogeological system based on field observations with final hypotheses on changed flow patterns in the peatland due to anthropogenic interferences. The impact of former inundations on saltwater distribution in the peat and aquifer, as well as local differences in the ionic composition are discussed. Further, potential SGD from the unconfined dune and beach deposits and the confined aquifer based on hydraulic heads on the landside is estimated.

Chapter 4 describes the development, calibration and validation of the transient 3D-groundwater flow model. The most important but uncertain parameters, evapotranspiration and specific storage, are tested in a sensitivity analysis.

Chapter 5 discusses the results of the transient simulation to identify the driving forces for varying SGD, seawater intrusion (SWI) and surface water discharge rates. The short-term effects on flow paths in the peatland and offshore in the light of geological heterogeneity with possible impacts on biogeochemical processes are further discussed based on findings in Chapter 3 and from other studies. Steady-state scenario simulations of the pristine, drained and rewetted peatland are discussed in terms of travel time and recharge and discharge areas of groundwater.

Chapter 6 is a conclusion of the findings in Chapter 3 and 5 illustrating the relevance of short- and long-term drivers on groundwater flow and transport, closing with an

outlook for future research and a brief summary of the most important parameters that should be considered and further investigated to estimate the influence of changed groundwater flow regimes on ecosystem functioning of coastal fens.

2 Study site

The study site and nature reserve 'Heiligensee and Hütelmoor' (Fig. 2.1) is in north-eastern Germany at the Baltic Sea coast near the city of Rostock. The average annual precipitation at the weather station in Rostock-Warnemünde, 6 km away, is 621 mm, the average annual temperature is 9.2°C (1947 to 2018; DWD 2018). The area was shaped by the Weichselian ice age (Kolp 1957). Glacial till was deposited with the expansion of the glaciers. With their retreat, river valleys and deltas developed leading to the deposition of 2.5 to 15 m thick glacio-fluvial fine sands on top of the till (Kolp, 1957), which nowadays form a shallow aquifer. The Littorina transgression (8000 - 1200 BP) entailed a continuous rise of the groundwater level, resulting in the development of a paludification fen from around 7000 years PB onwards (Kreuzburg et al. 2018), when the sea-level rise slowed down (Lampe 2002). Gyttja developed first in depressions, followed partly by peat consisting of wood (Kreuzburg et al. 2018). The dominating peat type consists of moderately to strongly decomposed sedges (Carex) and reed (Phragmites australis). The surrounding forest grows on a slightly acidic podsol.

The peatland receives water from the surrounding forest. Before anthropogenic interference small creeks originating in the forest, drained directly into the Baltic Sea. Moderate drainage of the peatland started in the 18th century (HRO 2017) by construction of a few ditches. In 1976, a dense network of ditches, that still exists today, was built (Fig. 2.1) to enable use as grassland. The ditch system originates in the surrounding forest and leaves the peatland at its south eastern edge via the main ditch 'Prahmgraben'. Downstream, the water runs through the nature reserve Radelsee before entering the harbour area with connection to the Warnow river and the Baltic Sea (Fig. 2.1). Extensive drainage of the peatland was performed through

pumping via a pumping station from 1976 until 1991 and led to a compaction and degradation of the upper decimetres of the peat. The elevation of the peatland nowadays is between -0.15 and 0.75 m a.s.l. (above sea level) and peat thickness is up to 3 m in the central peatland near the coast and thins out towards the forest. The size of the peatland is 350 ha. Renaturation started in December 2009, when the water table was raised by construction of a ground sill at the outlet of the ditch system at 0.4 m a.s.l. (Fig. 2.1). Today, the surface water catchment (Fig. 2.1) of the peatland is 750 ha. The size of the groundwater catchment of the peatland is unknown but reaches up to 15 km further inland (LUNG, 2016). The surface water level is balanced by the ditch system, and is above ground surface in most parts of the peatland, typically with a lowering of the water level in late summer and subsequent increase in winter (Miegel et al. 2016). Most of the groundwater in the surrounding elevated forest still drains into the ditch system and passes the peatland (Miegel et al. 2016). Reed, rushes and sedges are the dominant plants within the peatland, interrupted by areas of open surface water where hydrophytes expand (Koch et al. 2017).

The peatland adjoins the Baltic Sea along a 3 km long shoreline and is separated by an up to 40 m wide dune dike from the 50 m wide beach. The dune dike was initially constructed in 1903 and heightened in 1963 and prevents the peatland from being flooded. Inundations occurred 1872, 1904, 1913/14, 1949 and 1954 (Kolp 1957). Afterwards only in 1995 a breach in the dune dike occurred in its northern part near the natural freshwater lake 'Heiligensee' (Fig. 2.1), causing inundation and salinization of the peatland. Maintenance of the dike was stopped in 2000. Tides occur only with a small amplitude of 0.1 to 0.2 m in the Baltic Sea, and common sea level fluctuations of several decimetres are driven by wind. Seawater can enter the peatland not only over the dune dike, but also via the ditch system, which occurs when the sea level exceeds the height of the ground sill (0.4 m a.s.l.) and the water level of the peatland (Miegel et al. 2017; Selle et al. 2016).

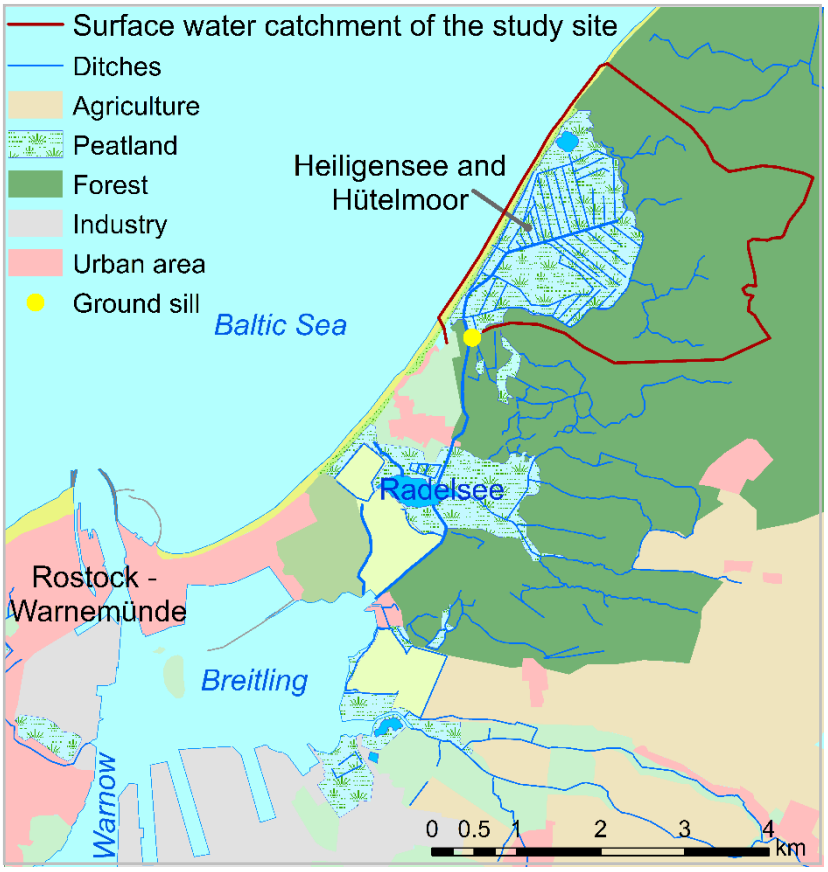

Figure 2.1: Location of the study site 'Heiligensee and Hütelmoor'.

3 Field investigations

3.1 Field and laboratory methods

3.1.1 Geological investigation

Sixteen sediment cores were drilled down to a max. depth of -15 m a.s.l. (Fig. 3.1) with a percussion driller and open metal rods of 4 cm diameter. To assess the peat thickness in more detail, peat probings were conducted. Hereby, a 1 cm diameter metal rod is pushed through the peat until the resistance indicates the beginning of the sand layer. In addition, data on peat thickness from Dahms (1991) and Krüger (1995) were transferred into the current height reference system (NHN 1992) and the peat depth distribution was interpolated for the whole peatland using kriging. All drilling and probing locations were levelled with a digital level (Leica Sprinter 250M) or real-time kinematic and differential GPS (Leica Viva Net-Rover). The sediments in selected ditches were assessed using a sludge sampler. Furthermore, the depth of ditches was measured using a plumb line from a boat. The selected ditches were the main ditch over its full length and small ditches connected to the main ditch, as well as the ditch at the border to the forest.

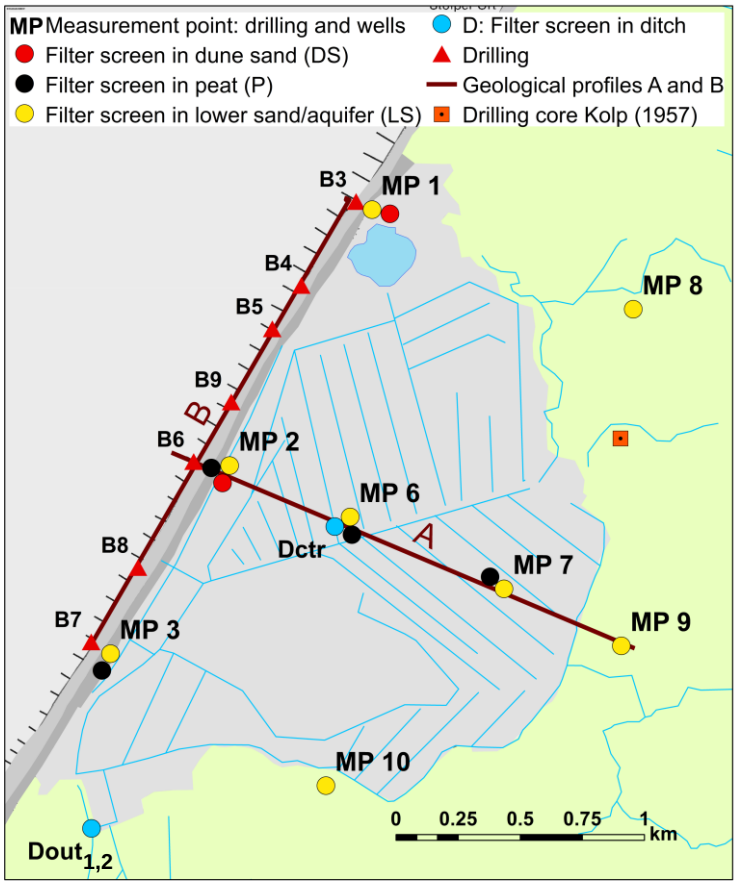

Figure 3.1: Study site 'Heiligensee and Hütelmoor' with groundwater observation wells and drilling locations. Brown lines A, B indicate geological profiles. At MP 7 two sediment cores were taken. At D_{out1} is installed upstream and D_{out2} downstream of the ground sill.

3.1.2 Field instrumentation

A total of 14 groundwater observation wells were installed at 7 locations (Fig. 3.1). Observation wells are arranged as well nests, which are called measurement points (MP) in the following, with filter screens in different geologic layers: Dune sand (DS), peat (P) and lower sand (LS, also referred to as aquifer) (Fig. 3.1). In addition, three wells were installed in ditches: D_{ctr} in the central part of the peatland next to MP6, and D_{out1} and D_{out2} above and below the ground sill at the outlet of the surface water catchment, respectively (Fig. 3.1). All 17 observation wells were equipped with data loggers to record pressure (P), temperature (T) and electrical conductivity (EC) (Dipper-PT or PTEC, SEBA Hydrometrie) in 15-minute intervals. For further

details, see Table A1 in the supplement. Density was calculated internally from EC and temperature after Fofonoff and Millard Jr. (1983). Air pressure was measured at station MP2. The overall measurement error is difficult to estimate, but typically lies within a few centimetres (Rau et al. 2019).

3.1.3 Calculation and usage of equivalent freshwater heads

To consider the influence of density equivalent freshwater heads ($h_{f,i}$) at each groundwater well screen (or point *i*) were calculated from the measured point water heads (h_i) after Post et al. (2007):

$$h_{f,i} = \frac{\rho_i}{\rho_f} h_i - \frac{\rho_i - \rho_f}{\rho_f} z_i \qquad (2.1)$$

With ρ_i the measured density at point i, ρ_f the freshwater density, and z_i the elevation head, which is the difference between the reference datum (mean sea level) and the well screen depth.

The calculated freshwater heads differed not more than 0.01 m from the point water head, except for 1LS with 0.02 m. This lies within the measurement error. All calculations and graphs in the following use or show equivalent freshwater heads. In the following 'hydraulic head' refers to equivalent freshwater head.

3.1.4 Hydraulic conductivities

Falling head and rising head slug tests were performed in all wells. The data was analysed with AQTESOLV (Software provided by HydroSOLVE, Inc., www.aqtesolv.com) using the KGS-model (Kansas Geological Survey, Hyder et al. 1994) to obtain radial hydraulic conductivity parameters. For the wells installed in peat, data from the permanently installed data loggers were used to evaluate the slug test due to the long recovery times of hours to days. In addition, grain size analysis was performed for selected samples of the drilling cores using a combined

sieve and pipette analysis. Hydraulic conductivity was then estimated using the empirical equations by Beyer (1964) and Hazen (1892).

3.1.5 Groundwater sampling

Groundwater samples were obtained from all groundwater wells, except from MP3 due to technical problems, in September 2017 and in April 2018. Before sampling, water in the wells was pumped with a submersible pump until the in-situ parameters EC, pH, temperature and oxygen had stabilized. The volume of water pumped out prior to sampling was at least twice the volume of the well. The water was filtered with CA 0.2 μm filters and filled into plastic bottles. Samples for analysis of cations were acidified with methane sulfonic acid. The samples were cooled at 4°C and in case of the metals frozen until the analysis.

3.1.6 Laboratory analyses

The analysis of anions (SO_4^{2-}, Cl^-, Br^-, NO_3^-) and cations (Mg^{2+}, Ca^{2+}, Na^+) was done with anion and cation chromatography (DX320 and DX500, Dionex), respectively. For anion chromatography a AS11-HC column was used and for cation chromatography a CS16 column. The eluents applied were methane sulfonic acid (18 mM) for anion analysis and KOH (23 mM) for cation analysis.NH_4^+ and PO_4^{3-} were analysed using a continuous flow analyser (CFA, Seal Analytical), dissolved inorganic carbon (DIC) and dissolved organic carbon (DOC) were analysed using the DIMATOC 2000 (DIMATEC Analysentechnik), and iron (II) was analysed using the inductively coupled plasma-atomic emission spectroscopy (ICP Optima 8300, Perkin Elmer).

3.1.7 Groundwater ages

Apparent piston-flow groundwater ages were determined with the tritium-helium method. Anthropogenic tritium ^3H (or T) was emitted in large quantities into the stratosphere during over ground tests of hydrogen bombs between 1955 and 1963

(Solomon and Cook 2000). It reacts to the water molecule HTO and becomes part of the hydrological cycle. Radioactive ^{3}H decays to ^{3}He (henceforth: tritiogenic $^{3}He_{tri}$) with a half-life of 12.32 years (Lucas and Unterweger 2000). Concentrations are given as a hydrogen isotope ratio called tritium unit (TU). One TU equals 10^{-18} $^{3}H/^{1}H$. The tritiogenic ^{3}He concentration converted to 1 TU equals $2.49 \cdot 10^{-12}$ $^{3}He_{tri}$ cm^{3} STP/kg water (STP = standard temperature and pressure). Tritium enters the groundwater as recharge from precipitation. The tritium concentration of precipitation in Germany is measured since 1959 (IAEA, GNIP). The method allows to distinguish between water that infiltrated before 1955 and therefore is almost tritium-free, and younger water with anthropogenic tritium, where an apparent age can be calculated. Sometimes a water sample represents a mixture of water from before and after the bomb tests. A sample with water from before the bomb tests has a tritium concentration of less than 0.15 TU from the leftover of about 5 TU natural tritium in precipitation. All recharge after roughly 1955 still has concentrations of 6±1 TU today (IAEA 2014 precipitation data from Germany corrected for decay until 2015). The tritium-helium clock for groundwater starts when the new produced ^{3}He cannot escape to the atmosphere anymore and accumulates in the water. That is when the water reaches the saturated zone. The tritiogenic $^{3}He_{tri}$ must be separated from other sources of ^{3}He in the groundwater: The ^{3}He equilibrium concentration $^{3}He_{equi}$ is determined by conditions of the atmosphere during recharge and is calculated here with the solubility function of Weiss (1971). Additional $^{3}He_{excess}$ enters the groundwater through air bubbles which are assumed to fully dissolve. To derive $^{3}He_{excess}$ neon (Ne) is measured, which only originates from the atmosphere. The deviation of the measured Ne concentration from the air-saturated equilibrium concentration is called ΔNe. From this the amount of excess ^{3}He is calculated. Another source is ^{3}He produced by subsurface nucleogenic processes. This so called radiogenic $^{3}He_{rad}$ appears in a fixed ratio to $^{4}He_{rad}$ of about $2*10^{-8}$ in groundwater (Mamyrin and Tolstikhin 1984), two orders of magnitude lower than the atmospheric $^{3}He/^{4}He$ ratio. Moreover, radiogenic $^{4}He_{rad}$ itself is useable for dating if the accumulation rate of $^{4}He_{rad}$ is known and constant within the aquifer. According to Solomon et al. (1996), the method is also applicable

to date decade old groundwater in aquifers consisting of recently eroded sediments. Samples for tritium-helium analysis were taken according to Sültenfuβ et al. (2011) in the lower sand (aquifer) at the observation wells along the coast (1LS, 2LS, 3LS) and along the central peatland profile (6LS, 7LS and 9LS) between 25th January and 7th February 2017. The samples were analysed at the Bremen Helium Isotope Lab (Sültenfuß et al. 2009).

3.1.8 Calculation of groundwater flow velocity and discharge

The horizontal flow velocity in the aquifer within the peatland was calculated based on Darcy's law to compare it to obtained apparent groundwater ages and estimate whether horizontal flow in the aquifer is an important flow component. Therefore, the average hydraulic gradient was calculated for the period between February 2017 to June 2018 between the wells 7LS and 6LS. From an averaged hydraulic gradient, measured hydraulic conductivity (K) and effective porosity (n_e) for silty fine sand (value taken from Hölting and Coldewey, 2013) an average groundwater flow velocity was calculated. Vertical flow velocities between 7P and 7LS (and 6P and 6LS) were not calculated because the vertical hydraulic gradient today (and to a smaller extent the hydraulic conductivity of the peat) is very different to the vertical hydraulic gradient under past hydrological conditions. This would be difficult to interpret when comparing it to older groundwater.

If density effects on horizontal flow are considered as described in more detail in Post et al. 2007, one of the well screen depths has to be defined as the reference depth z_r, while the freshwater head of the second well has to be corrected to the reference depth of the first well, and is called $h_{f,r}$. Further, the effect of an averaged density between the two wells, ρ_a, must be considered. This is described in the following taken from Post et al. 2007:

$$h_{f,r} = z_r \frac{\rho_i}{\rho_f}(h_i - z_i) - \frac{\rho_a}{\rho_f}(z_r - z_i) \quad (2.2)$$

With ρ_i the measured density at point i, ρ_f the freshwater density, and z_i the elevation head of the second well.

Then, a hydraulic gradient between the two wells can be calculated. This was tested but the effect was negligible with less than a centimetre difference for the calculated freshwater head at reference depth. This is due to very similar densities at 7LS and 6LS, and hence was not included in the final calculation.

Groundwater discharge within the aquifer and the dune at the coastal interface was calculated using Darcy's law. An estimate of submarine groundwater discharge was not possible with this method because vertical flow, the exact discharging point, and density effects were ignored or unknown. The discharge within the aquifer towards the sea was calculated over 80 m, defined by the observation wells behind the dune (1LS, 2LS, 3LS), and the position of the average water line of the Baltic Sea. The density of the water in the aquifer below the beach was not measured but Jurasinski et al. (2018) indicated a freshening of the groundwater with depth. Hence, no correction according to Formula 2.2 for density was done. The hydraulic gradient was calculated based on averaged hydraulic heads of 1LS, 2LS and 3LS to represent the hydraulic head along the coast, and the sea level. Due to partly confining conditions in the aquifer where the peat layer crops out offshore (Kreuzburg et al. 2018) the applied sea level might not exactly represent the head in the aquifer along the total length of the coastline. The discharge area was defined by an average aquifer thickness of 3.55 m (based on drilling results) over a coastal length of 3000 m. Temporal variation (15-minute interval) of the discharge was calculated for the period between February 2017 and June 2018, neglecting the changing position of the water line. The discharge in the dune was calculated based on averaged hydraulic heads in the dune sand (1DS and 2DS) and the sea level over 80 m, assuming an average thickness for the water saturated dune sand of 1.6 m. The discharge was averaged for the period between February 2017 and June 2018.

Measured hydraulic conductivities for the aquifer and dune were used. The discharge from the peat was not calculated because it was assumed that flow in the less permeable peat is vertical.

3.2 Results and discussion

3.2.1 Geological structure of the coastal peatland

The sediment cores reveal a complex structure of the peatland geology with varying depth and extent of the peat and the fine sands underneath (Fig. 3.2, 3.3 and 3.4). The base of the aquifer, the glacial till, is found at depths between -3.4 and -14 m a.s.l.. The till layer is locally overlain by a few centimetres of coarser sand and gravel sediments typical for riverbeds. The fine sands forming the shallow aquifer are between 2 and 10.5 m thick (Fig. 3.2 and 3.3). A distinct valley structure was found below the beach (at core B9 in Fig. 3.2) with the till at a depth of -14 m a.s.l.. It is assumed that this is part of an ancient glacial river valley that has been described east of the peatland with a depth of -15 m a.s.l. (for location, see Fig. 3.1) by Kolp (1957). Hence the valley structure is expected to continue below the peatland. A more than 2 m thick silt-clay layer interpreted as lacustrine sediments (Kreuzburg et al., 2018) is found in the area of lake Heiligensee on top of the fine sand, but also as thin outcropping layers within the sand (Fig. 3.2). The peat on top of the aquifer consists of medium to strongly decomposed sedges and reeds and in the lower part of wooden peat. Locally gyttja or lacustrine sediments of less than 0.1 m thickness were found below the basal peat (Fig. 3.2 and 3.3). The peat thickness is heterogeneous (Fig. 3.4). It reaches almost 3 m thickness in the central part of the study site between the coast and the main ditch. Towards the forest the peat thickness decreases as the onset of peat growth started later. At the coast, the peat got eroded by sea-level rise and hence only thin peat layers remained offshore depending on their depth (Fig. 3.2 and Fig. 3.4). Below the beach, the peat is 0.1 - 1.5 m thick (Fig. 3.2 and 3.4) but was eroded towards the southern borders (MP3) and near lake Heiligensee (MP1) during storm surges (Kolp, 1957; Kreuzburg et al.,

2018). At the coast, fine to medium dune sands and marine medium to coarse sands and sometimes larger pebbles are found on top of the peat (Fig. 3.2). The sequence found here with peat underlain by several meters of sands and glacial till at the basis is typical and found at several sections along the Baltic Sea coast of Mecklenburg-West Pomerania.

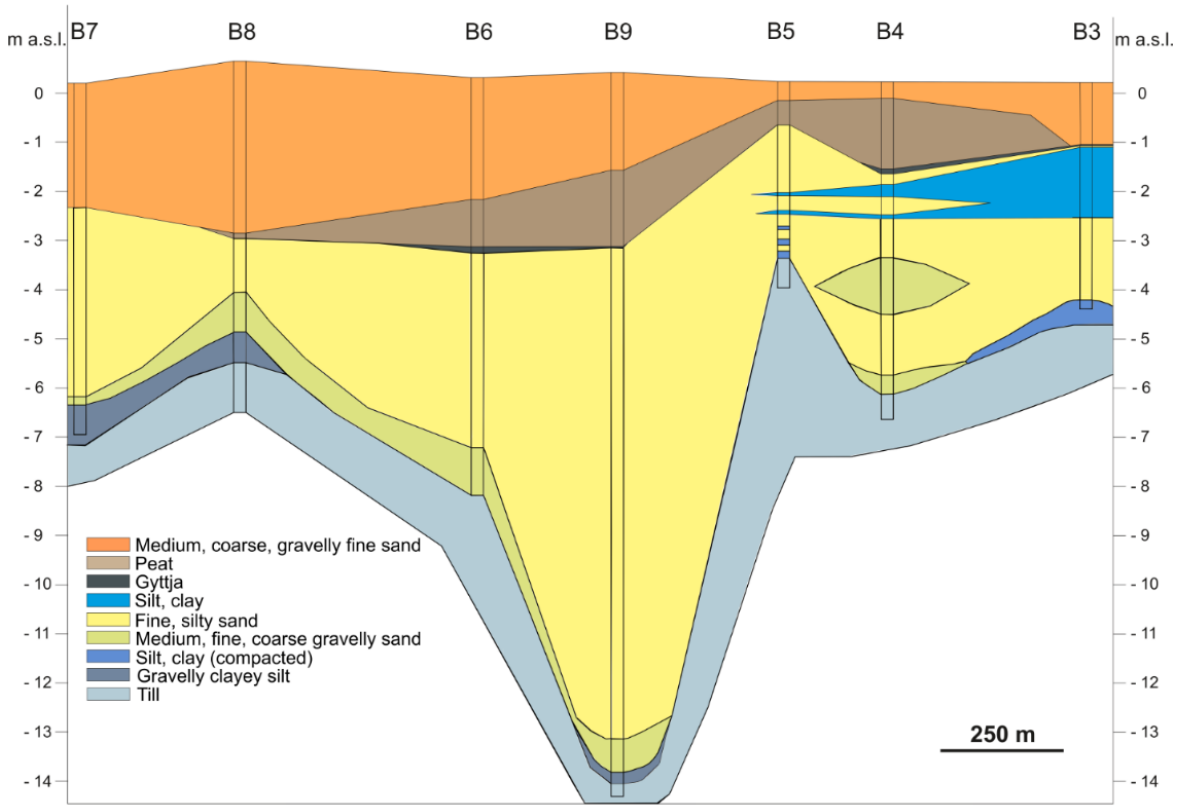

Figure 3.2: Geological profile B along the beach at the study site 'Heiligensee and Hütelmoor' with location of drilling cores.

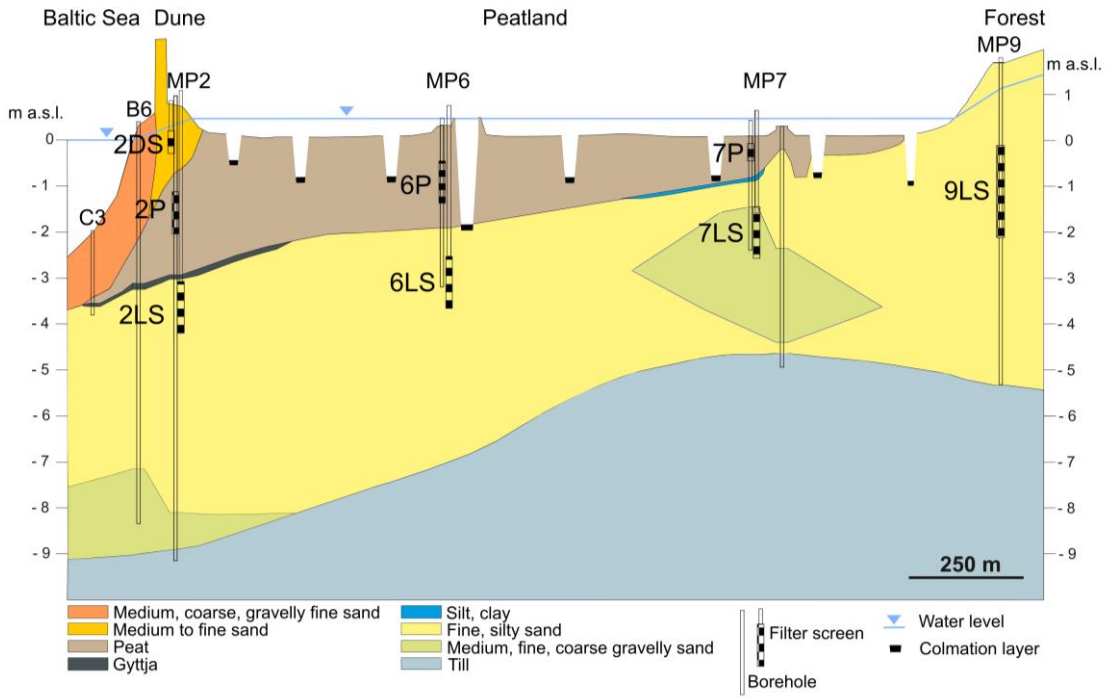

Figure 3.3: Geological profile A through the study site 'Heiligensee and Hütelmoor' perpendicular to the coast with locations of drilling cores (core C3 from Kreuzburg et al. 2018) and groundwater observation wells with filter screens.

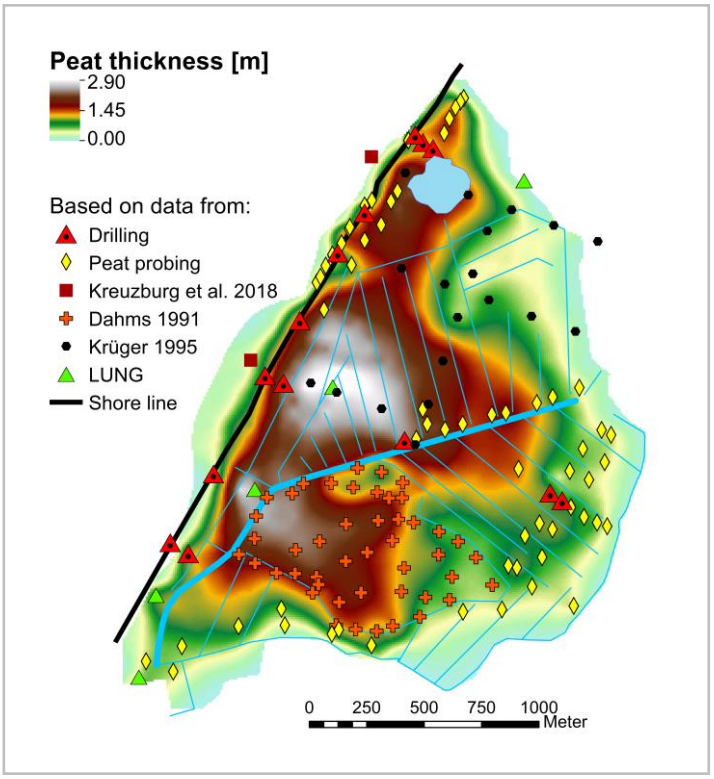

Figure 3.4: Peat thickness at the study site 'Heiligensee and Hütelmoor' interpolated from own drillings and peat probings and data from literature.

The hydraulic conductivity K of the peat varies between $1*10^{-6}$ m/s in the upper decimetres of the peat at MP7 previously exposed to drainage with possible desiccation cracks and roots, and $1*10^{-8}$ m/s in 1 - 2 m depth at MP2, where the weight of the dune sand may have further compacted the peat. Values of $4.6*10^{-6}$ to $1.4*10^{-5}$ m/s have been reported previously by Dahms (1991) without specification of depth. The sandy aquifer is rather homogeneous with K values around $2*10^{-5}$ m/s, which confirms values reported by Dahms (1991). At MP7 (Fig. 3.3) – and also at B4 (Fig. 3.2) – a lens of fine to coarse sand and gravel is found, where K increases locally to $6*10^{-5}$ m/s. The lacustrine sediments have a very low hydraulic conductivity of $1*10^{-8}$ to $1*10^{-9}$ m/s. Hence partially confining conditions can occur in the peatland where the less permeable peat layer or lacustrine sediments overlay the aquifer. In contrast, the ditches that cut into the aquifer may result in unconfined conditions. However, it was found that the main ditch with a depth of -1.5 m a.s.l is covered with an organic layer of 0.1 m thickness in average indicating a colmation of the sandy bed.

3.2.2 Hydraulic gradients from land to sea

The investigated years 2016 to 2018 were either very dry or very wet: The annual precipitation (Warnemünde DWD) was 480 mm in 2016, 739 mm in 2017 (with 40 % of the precipitation in the summer months) and only 437 mm in 2018 with least precipitation in autumn (15% of total precipitation). This precipitation pattern impacted on the groundwater levels measured in the peatland. The high precipitation in 2017 led to an increased water retention in the peatland and hence to highest water levels in April 2018, followed by a drought, whereby lowest water levels were reached in October 2018 (Fig. 3.5). In general, the groundwater level was highest in the forest with an average of 0.94 m a.s.l. at 9LS (range: 0.00 to 1.32 m a.s.l.). The average water level in the peatland was 0.41 m a.s.l. (7P; range: -0.45 to 0.75 m a.s.l.). The large hydraulic gradient (average 0.003) between the forest and the peatland is caused by the ditch system. The water levels in the forest and in the central peatland both within the peat (6P, 7P), in the aquifer (6LS, 7LS) and in the

ditch (D_{ctr}) all follow the same trend (Fig. 3.5) driven by the climatic water balance. The hydraulic gradient between 7LS and 6LS in the central peatland is very low due to the balanced water level in the ditch system. An average hydraulic gradient of 0.002 within the aquifer established between the peatland and the coast (Fig. 3.5). Water levels in the aquifer along the coast correlated with the sea level (see exemplary for 2LS in Figure 3.5). The water level at 1LS (northern corner of peatland) was slightly higher than at 2LS and 3LS (Fig. 3.6), which is due to the absence of drainage ditches in that area and the vicinity to the higher elevated forest and hence more inflow of groundwater. Spring and summer (March to September 2017 and March to April 2018) were characterised by a high water level in the peatland and low sea level fluctuations, and a stable hydraulic gradient from the peatland to the coast established. In autumn and winter the sea level sometimes exceeded the water level in the peatland by up to 1.18 m during storms. The same was observed in the unusual wet and stormy summer 2017 (Fig. 3.5). The hydraulic gradient at the coast reversed for a few weeks and up to two months when the water level on the landside was very low in autumn 2016 and in the very dry summer and autumn of 2018, respectively. At the outlet of the peatland ditch system, the water level downstream of the ground sill (D_{out2}) showed distinct peaks of high water levels that correlated with a high sea level (Fig. 3.5, Fig. 3.6). Sometimes it even exceeded the water level in the central peatland (Fig. 3.6), resulting in an inflow of water into the peatland via the ditch system as has also been reported in Miegel et al. (2017).

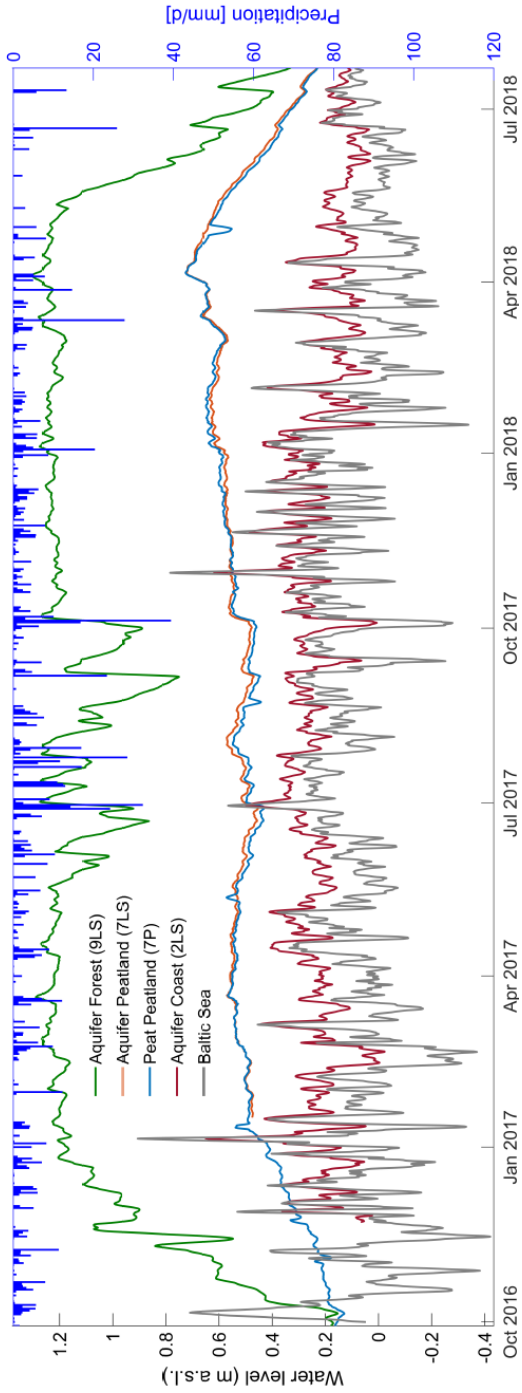

Figure 3.5: Water levels (freshwater heads) (running-mean 3 days) at the study site 'Heiligensee and Hütelmoor' from the forest to the coast (left y-axis) and precipitation (right y-axis). The complete water level data is shown in Figure 3.6. Precipitation from DWD (2018), Baltic Sea level provided by Bundesamt für Seeschifffahrt und Hydrographie.

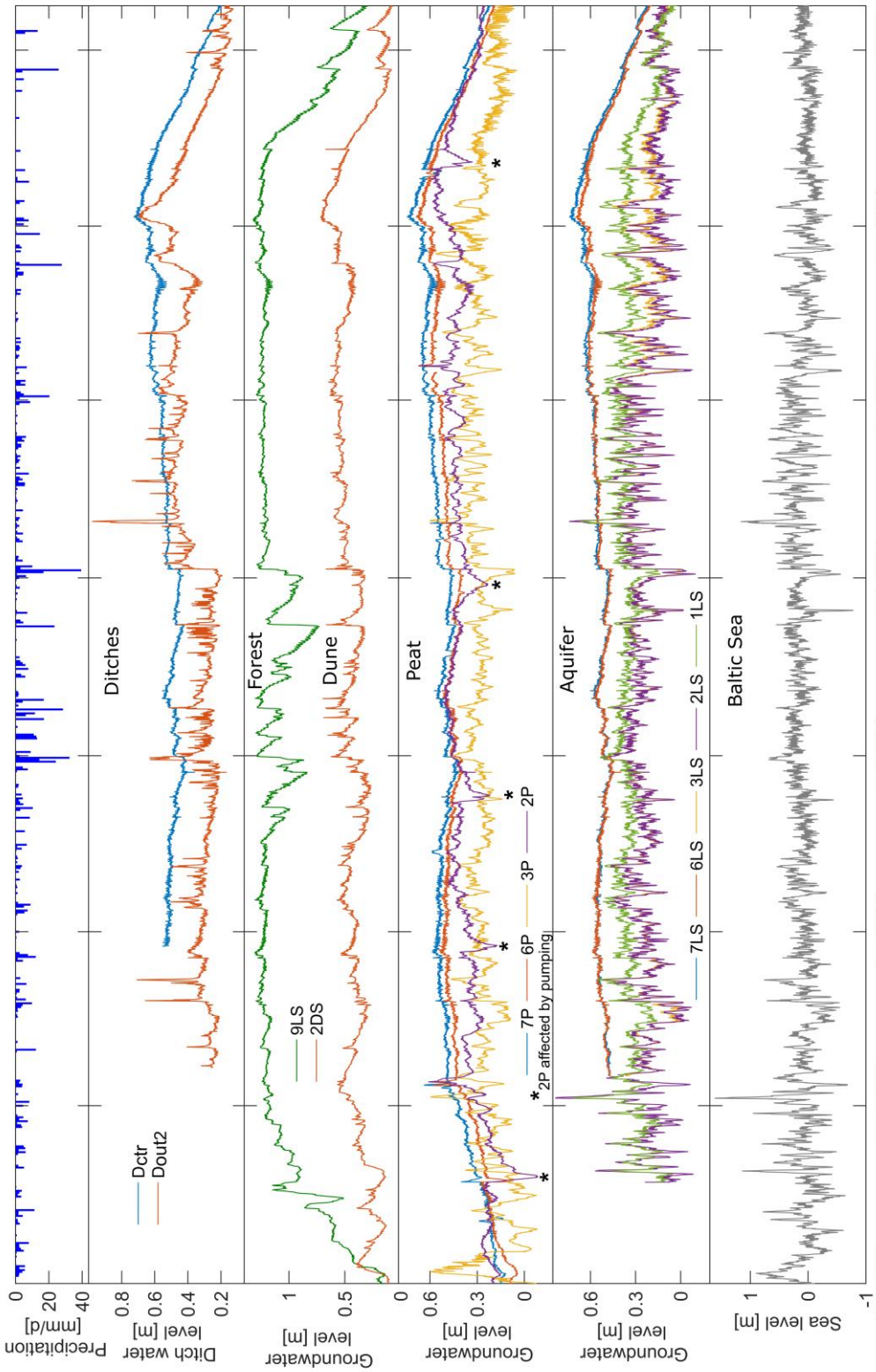

Figure 3.6: Groundwater level (freshwater heads) at the study site 'Heiligensee and Hütelmoor', and Baltic Sea level (data provided by Bundesamt für Seeschiffahrt und Hydrographie) and precipitation (DWD, 2018) at Warnemünde.

3.2.3 Distribution and alteration of seawater in the peatland

The current measured EC in the groundwater showed a large spatial variation at the study site (Fig. 3.7a) from a minimum of 0.7 mS/cm in the forest to a maximum of 11.4 mS/cm near the coast at 1LS. The Baltic Sea has an average EC of 21 mS/cm at the study site (IOW, 2018). In the central peatland, the average EC was 9.3 (7P) and 8.1 mS/cm (6P), and in the aquifer below 7.6 (7LS) and 6.9 mS/cm (6LS). The EC was lower near the coast with 6.3 mS/cm (2LS), 5.0 mS/cm (2P) and 3.6 mS/cm (3P and 3LS). Only at 1LS, where several seawater breakthroughs occurred in the past and the dune dike is disappearing, high values of up to 11.4 mS/cm were measured. In the dune sands the EC was in average 1.0 mS/cm (2DS), indicating freshwater recharge in the dune dike. The relatively high EC in the central aquifer demonstrates a strong influence of sea water, but the decrease towards the coast disproves the intrusion of saltwater as a cause. Pore water profiles of the upper 60 cm of the peat measured by Koebsch et al. (2019) showed fresh water in the first 20 cm and more saline water further downwards, indicating a freshening of the groundwater at the soil surface resulting from rewetting the peatland. Hence our measurements of the EC in the peat (6P and 7P) can be regarded a mixture of young fresh water and older, brackish water.

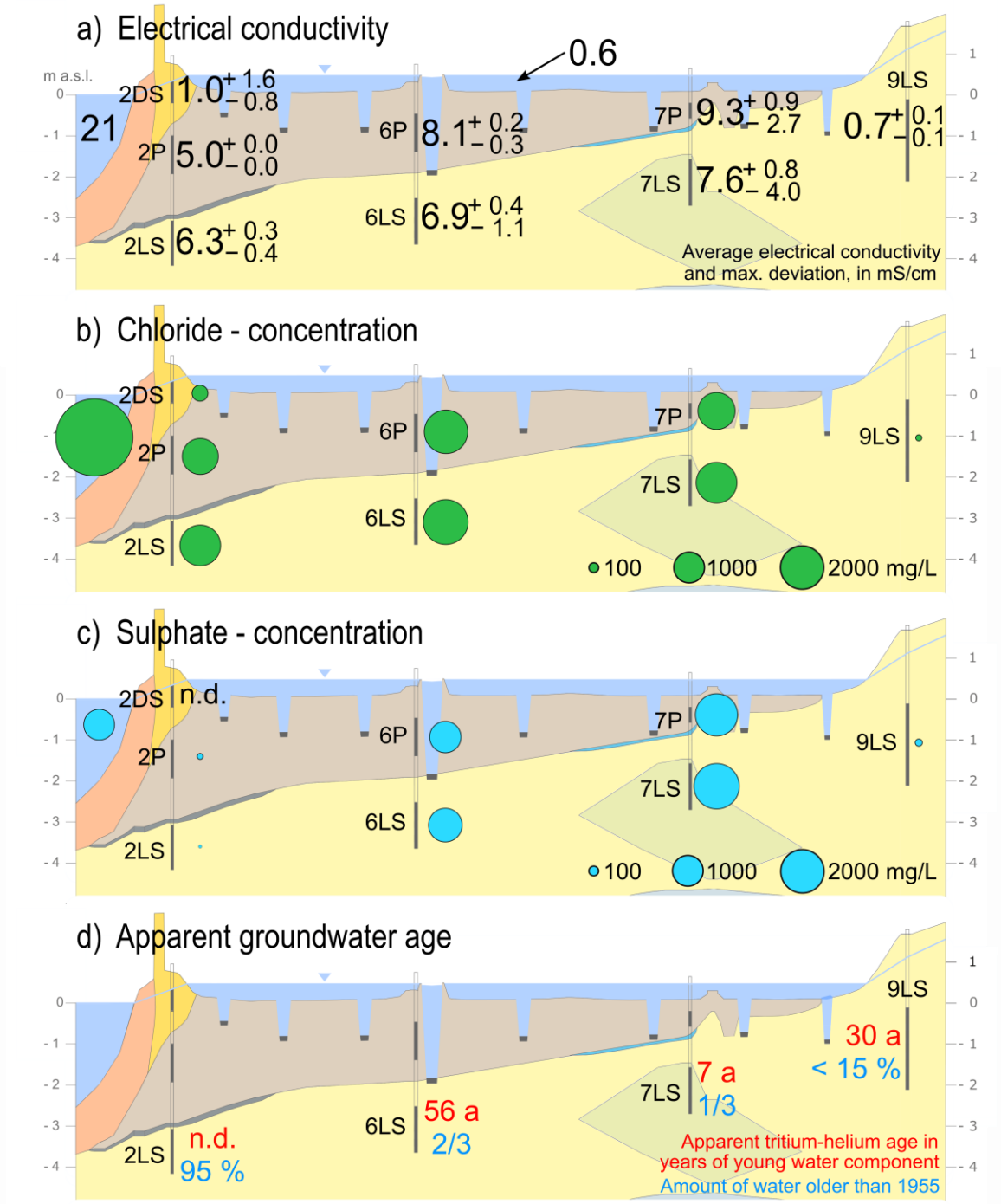

Figure 3.7: Groundwater properties at the study site 'Heiligensee and Hütelmoor'. (a) Electrical conductivity (EC), (b) Chloride concentrations, (c) Sulphate concentrations, (d) Apparent groundwater age based on tritium-helium analysis (red) and amount of tritium-free water (blue). For legend of geological profile, see Fig. 3.3.

Chloride and sulphate are both common in sea water; chloride is considered a conservative tracer for transport processes, while sulphate is altered by biogeochemical reactions (e.g. Canfield, 2001; Jørgensen, 1982). The chloride concentrations (Fig. 3.7b, Table A.2) were highest both in the peat and aquifer at MP6, followed by MP2 and MP7, and in general the chloride concentrations were slightly elevated in the aquifer compared to the peat. Sulphate (Fig. 3.7c) was enriched at 7LS, even exceeding concentrations of the Baltic Sea by a factor of two. Koebsch et al. (2019) showed that the source of sulphur is the Baltic Sea using stable isotope analysis. Further they showed that sulphur reducing bacteria depleted the sulphate pool at some spots, while a spot near MP7 indicated elevated amounts of iron in the form of labile iron minerals and dissolved ferrous iron (Fe(II)), which we confirm by our measurements of elevated Fe(II) at MP7 (Table A2). Iron is assumed to originate from the mineral soil (Koebsch et al., 2019) and in the form of Fe(III) it is alternatively used by certain sulphate reducing bacteria as an electron acceptor instead of sulphate (Postma and Jakobsen 1996). Koebsch et al. (2019) further investigated the different iron species, which are not presented here. The comparison of the molar SO_4^{2-}/Cl^- ratios in the groundwater (Table A2) with the current ratio from the Baltic Sea indicates that sulphate has been enriched at 7LS, slightly reduced at 6LS and almost completely reduced at 2LS, which affects the measured EC (Fig. 3.7 a-c). Processes like oxidation of pyrite (Portnoy 1999) during intensive drainage could lead to an enrichment of sulphate and iron concentrations at 7LS. However, to explain these high concentrations further investigation is needed, which is beyond the scope of this study.

The chloride concentrations in the aquifer and peat in comparison to the current chloride concentration in the Baltic Sea (Fig. 3.7b, Table A2) indicates 24 % ± 4 (standard deviation of the averaged concentration of all samples at 2P, 6P, 7P) of sea water in the peat and 29.9 % ± 3.2 (standard deviation of the averaged concentration of all samples from 2LS, 6LS, 7LS) of sea water in the shallow aquifer, which appears to be a rather homogeneous distribution. An increase of solute concentration due to ET is unlikely because a change of the EC (Fig. 3.8) is not seen

during the drought 2018. Selle et al. 2016 found seasonal variations of the EC of 3 to 4 mS/cm, but the annual water balance is positive (Miegel et al. 2016) and hence no increase in solute concentration is expected.

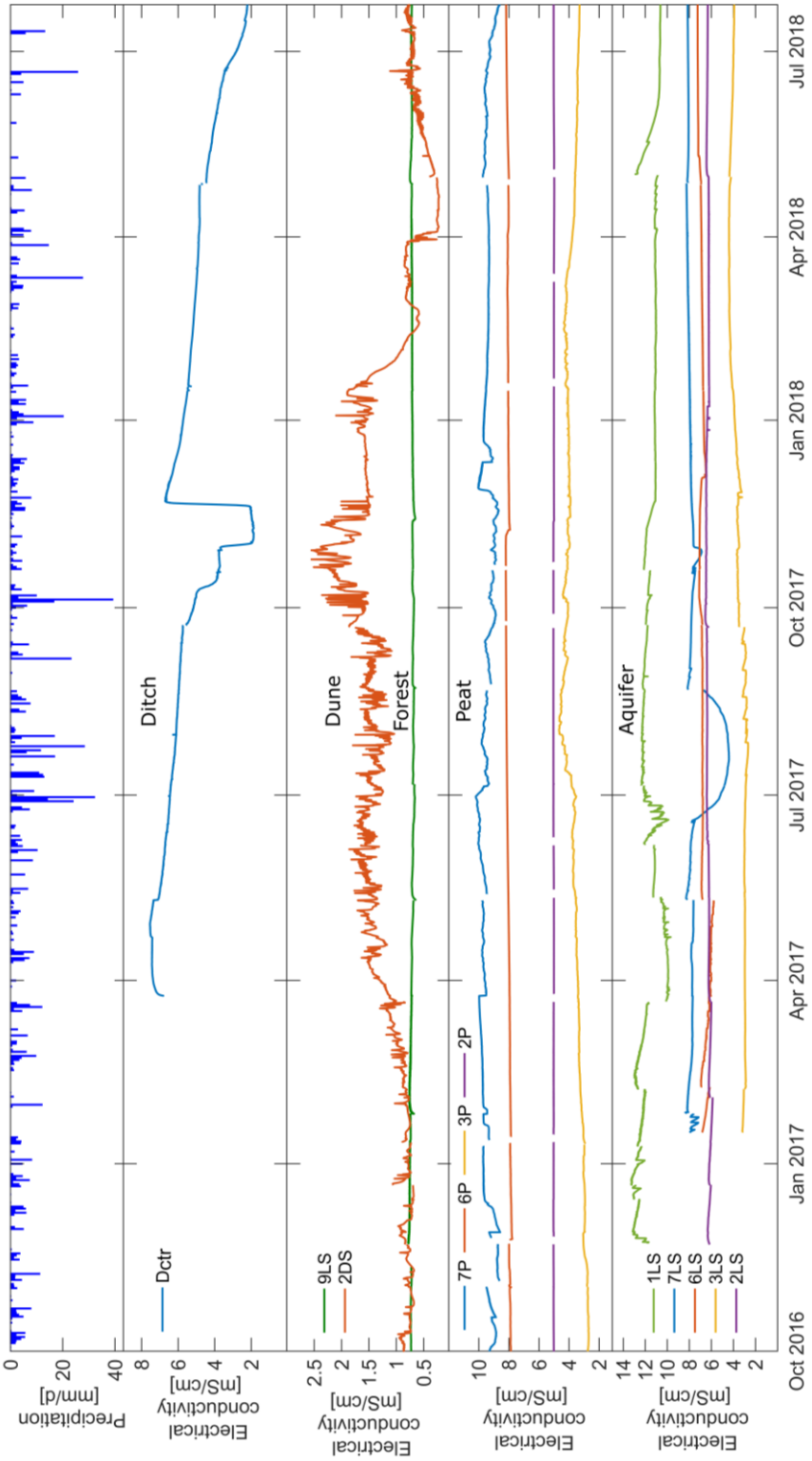

Figure 3.8: Electrical conductivity in the groundwater at the study site 'Heiligensee and Hütelmoor', and precipitation at Warnemünde (DWD, 2018).

3.2.4 Age and origin of groundwater

A larger time scale must be considered to understand the flow system in the peatland and the influence of changed hydraulic conditions over the last decades and centuries. The apparent tritium-helium ages of the groundwater in the aquifer are shown in Figure 3.7d together with the amount of water that is tritium-free and hence older than 1955 (for ^{3}H and $^{3}He_{tri}$ concentrations see Table A2). Analytical uncertainties (1 sigma) of duplicates of this study are smaller than 5% for tritium and less than 1.5 years for ages. As in groundwater recharged after 1960 tritium has decayed to an almost constant concentration of 6 ± 1TU (for northern Germany) this allows to identify the amount of water that is tritium-free and hence older than 1955 (for ^{3}H and $^{3}He_{tri}$ concentrations see Table A2).

The tritium-containing groundwater in the forest close to the border of the peatland (9LS) has an apparent age of 29 years while the older, tritium-free groundwater water portion can be up to 15 % of the total sample (6 TU tritium). The low EC of 0.7 mS/cm indicates an origin from recharge within the surrounding forest. In the aquifer below the peat at 7LS the apparent age of tritium-containing water is 7 years and approximately one third of the water is tritium-free water and hence older than 1955. This indicates mixing of very old with very young water components. The young groundwater component at 7LS compared to the age in the forest can be explained by vertical infiltration of surface water. The peat layer at MP7 is only 0.9 m thick and probably rhizomes, and the rewetting of the peatland seven years before sampling has enabled enhanced infiltration. At 6LS in the central peatland the apparent age of the portion of the water containing tritium is 56 years and the portion of water older than 1955 increases to about two third. At 2LS near the coast the amount of tritium-free water increases to about 95 %, hence no apparent age could be determined.

Based on the hydraulic head measurements and with a K of $2*10^{-5}$ m/s and n_e of 0.1 the current lateral groundwater travel time between 7LS and 6LS resulted in 7200 years. Even under drained conditions the overall hydraulic gradient within the peatland would be similar due to the balancing ditch system. Hence, the apparent

groundwater ages indicate that not solely lateral inflow from the forest, but recharge of surface water is an important water source. It is assumed that the water is strongly stratified in age and that the pumping during sampling from a 1 m long filter screen led to the broad spectrum of ages in one sample.

A Ne concentration less than the equilibrium value ($\Delta Ne<0$) must be affected by a process which drives permeant gases out of the water. A possible process is massive production of gases like CH_4 and the subsequent formation of bubbles in the subsurface (Sültenfuß et al. 2011). ΔNe is 1% in the forest and decreases to -7% at 7LS, -30% at 6LS and -40% at 2LS near the coast. The decrease of ΔNe correlates with an increasing thickness of the peat layer. Sültenfuß et al. (2011) further showed that a diffusion-controlled fractionation of the analysed ^3He and Ne concentrations and their isotopes through degassing in peat was not the case. If degassing occurs slow enough all concentrations should decrease equally by solution into the methane bubbles due to similar solubility coefficients (Sültenfuß et al. 2011). ^3H as part of the water molecule was unaffected by degassing (Sültenfuß et al. 2011). Hence the calculated apparent groundwater ages should be too young. Finally, as $^4He_{rad}$ release rates from the aquifer matrix are not known, the $^4He_{rad}$ concentration in the groundwater can be used as an additional qualitative indicator for the contact time of water with the aquifer matrix only, i.e. the residence time (Solomon et al. 1996, 2000). With a $^4He_{rad}$ concentration of only $1.6*10^{-5}$ ccSTP/kg at 9LS the residence time is lowest in the forest. It is assumed that groundwater flow is relatively fast here driven by the hydraulic gradient (Fig. 3.5) towards the ditch system. At 7LS the concentration was $2.1*10^{-5}$ ccSTP/kg and increased largely to $2.1*10^{-4}$ ccSTP/kg at 6LS. At 2LS – the sample with the lowest tritium concentration – the $^4He_{rad}$ concentration was only $7.8*10^{-5}$ ccSTP/kg, although contradicting 6LS with higher tritium concentration also shows higher $^4He_{rad}$ of $2.1*10^{-4}$. Together with the negative ΔNe these results indicate that most water originates from recharge through the peat and not from the mineral aquifer at 2LS. At 6LS – near the main ditch – drainage might have led in the past to an upward directed flow of old

groundwater, where a higher $^4He_{rad}$ concentration indicates a longer residence time in the mineral aquifer.

In general, it is assumed that vertical flow dominates in the peat and partly in the aquifer, while horizontal flow in the aquifer might play a role where the hydraulic connection to the surface water is inhibited. Negative ΔNe indicates recharge through the peat during recharge or the rewetting process and $^4He_{rad}$ indicates upward flow from the deeper aquifer caused by the drainage function of the ditches. The longer the residence time of the water in either the peat or the aquifer, the higher the respective concentrations. More negative ΔNe further indicates that the calculated apparent groundwater age should be older. Hence, the parameters ΔNe, $^4He_{rad}$ and the apparent groundwater age are qualitative proxies for the origin of the analysed water sample and for the flow direction (downward through the peat or upward from the aquifer).

3.2.5 Short-term oscillations of vertical water flow

The apparent groundwater ages ΔNe and $^4He_{rad}$ indicated a long residence time of the water in general. On the short-term, the interaction between the groundwater and the ponded surface water in the peatland depends on climatic conditions and drainage ditches. Between ditches (MP7) the groundwater-surface water interaction was governed by changes in the amount of precipitation and ET: During times of enhanced precipitation and low ET in winter the water level in the peat was above the water level in the aquifer (Fig. 3.5), indicating downward directed flow. With enhanced ET in summer 2017, the water level in the peat decreased below the water level in the aquifer indicating a vertical flow reversal with upward directed flow from the aquifer (Fig. 3.5). In late summer 2018 the water level in the forest dropped drastically due to unusual low precipitation and high ET, and the inflow of surface- and groundwater from the forest to the peatland decreased. Therefore, the hydraulic head in the partly confined aquifer was too low and no upward directed flow in the peatland was visible in the water levels. Hence, recharge (downward flow) occurs during precipitation and small ET, while discharge (upward flow)

occurs during enhanced ET and sufficient groundwater inflow from the larger groundwater catchment as described in several studies (e.g. Devito et al. 1997, Drexler et al. 1999, Fraser et al. 2001, Kopp et al. 2013, Siegel and Glaser 1987). The flow direction may vary spatially within the peat depending on factors such as a local anisotropy of K (Drexler et al. 1999), local high specific storage (Reeve et al. 2006), methane production (Romanowicz et al. 1993) and the transpiration rate of the vegetation type (Drexler et al. 1999), which varies in the study site between reeds, submerged aquatic species in shallow open water and sedges in dryer areas (Koch et al. 2017).

Near the ditches the groundwater-surface water interaction is mainly governed by the water level in the ditch system, i.e. the rate of surface water discharge. At MP6, located near the main ditch, water levels indicated an in general upward directed flow from the aquifer (6LS) towards the ditch D_{ctr} during most of the year (Fig. A1). Only enhanced precipitation and a decreased discharge due to high water levels downstream of the ground sill (D_{out2}) as in spring 2018 led to a downward directed flow from the ditch towards the aquifer (Fig. 3.6).

Another indicator for changes in vertical flow direction is the EC. The temporal variability of the measured EC (Fig. 3.7a, Fig. 3.8) in the peat was largest in the upper first meter (7P, 3P), smaller at around 1 m (6P), and the EC was stable at a depth of 2 m (2P) (Fig. 3.7a, Fig. 3.8). EC fluctuations behaved accordingly in the aquifer below, hence they were more pronounced where the peat layer above the aquifer is thinner (MP7).

3.2.6 Hypotheses of past hydrological conditions

The hydrological conditions within the peatland changed several times over the last decades and centuries due to anthropogenic interventions. The apparent groundwater ages, ΔNe, $^4He_{rad}$ and Cl^- concentrations reveal a long memory of the peatland. But also, short-term processes like recharge, ET, and sea water inundations are assumed to affect the composition of groundwater. Based on the

depicted information in the previous chapters, a general idea of the flow paths during different hydrological states was derived. The in the following stated hypotheses will be further investigated through numerical modelling and help to identify processes that must be considered in the modelling process.

Today, it is assumed that input of water into the peatland is mainly through infiltration of surface water, while the inflowing groundwater from the forest is diverted by ditches surrounding the peatland (Fig. 3.9c). Flow fields in the peatland are assumed to be dominated by an overall downward directed flow and locally discharge towards the nearest ditch or coast. Water level oscillations due to varying precipitation and ET lead to flow reversals and enhance the residence time of water in the peat. Where the aquifer is deep and the peat thick enough to inhibit the discharge function of the ditches, e.g. in the ancient glacial river valley, a deep lateral flow towards the coast might establish that would lead to groundwater ages of several thousand years.

During the pristine state of the fen prior to anthropogenic interferences (Fig. 3.9a), the surface elevation of the peat was probably at least 0.5 m higher than today. In intact fens the water level is around ground level (Heathwaite 1993). The conditions were presumably similar to those today in the pristine fen Bierzba valley in Poland with similar topographic features and adjoined by a river instead of a sea (Wassen and Joosten 1996). A smooth gradient towards the river exist in the Bierzba valley, which can be transferred to this study in the form of a smooth seaward gradient. The upper peat horizon of a pristine fen is often more permeable than deeper peat horizons (e.g. Chason and Siegel 1986), and water flow in the upper peat was likely directed mainly towards the coast, while downward directed flow in the less permeable lower peat is assumed to have been slow. Groundwater inflow from the forest is assumed, though a few shallow creeks existed in the forest. Inundations with sea water are assumed to have occurred frequently due to a lower natural dune.

During two decades of intensive drainage of the peatland (Fig. 3.9b), water was pumped out of the ditch system, resulting in a water level of some decimetres below ground level, and often below sea level (Bohne and Bohne 2008). The ET in the peatland is assumed to have been less than today due to a water level below ground level. Hence, the hydraulic gradient at the coast must have been often reversed. The groundwater samples from 2LS indicate no previous saltwater intrusion, because the water's origin is likely in large parts from recharge through the peat layer and it is much older than the intensive drainage period. Whether a saltwater intrusion in the deeper part of the aquifer occurred is not known. At the same time, inflow of (salt) water into the ditch system at its outlet was prevented by a non-return valve (Voigtländer et al. 1996). The general groundwater flow pattern is assumed to have been similar to nowadays, but fluxes were likely increased due to larger hydraulic gradients between the peat body and the ditch system, and less colmation at the bottom of ditches. A general slow upward directed flow within the aquifer below the peatland is assumed during high pumping rates. Since the pumping led to an increased direct discharge of the inflowing water from the forest, the water level in the nearby forest must have been lower than today.

In the future (Fig. 3.9d) the sea level is expected to rise by more than 0.5 m until 2100 (Grinsted et al. 2015), accompanied by a rise of the inland groundwater level. The ditch system connected to the Baltic Sea – and therefore with a future average water level above the ground sill – will lead to more frequent inflow of sea water into and less discharge from the peatland. The dune dike, if as planned not maintained anymore, will be only a few decimetres above sea level, as can be seen already today in the northern part of the study site (MP1), and sea water inundations will occur frequently. The surface water level between the peatland and the Baltic Sea will then be balanced via the breaches in the dune dike and the ditch system. The hydraulic gradient between the forest and the peatland will persist and groundwater flow in the aquifer will still be upward at that border. Vertical fluxes – and hereby mainly downward flow – within the peatland will likely decrease if the seaward gradient and the drainage function of the ditches

decreases. The groundwater below the peat will only very slowly become more brackish through dispersive downward flow of the mixed surface water from the forest and the Baltic Sea. The permanent inundation of the peatland with brackish water is expected to influence vegetation (Koch et al. 2017), decrease methane emissions (Koebsch et al. 2019), and decrease the risk of further degradation of the peat. Koch et al. (2017) concluded that peat growth might resume under already current inundated conditions with a dominant salt-tolerant reed vegetation.

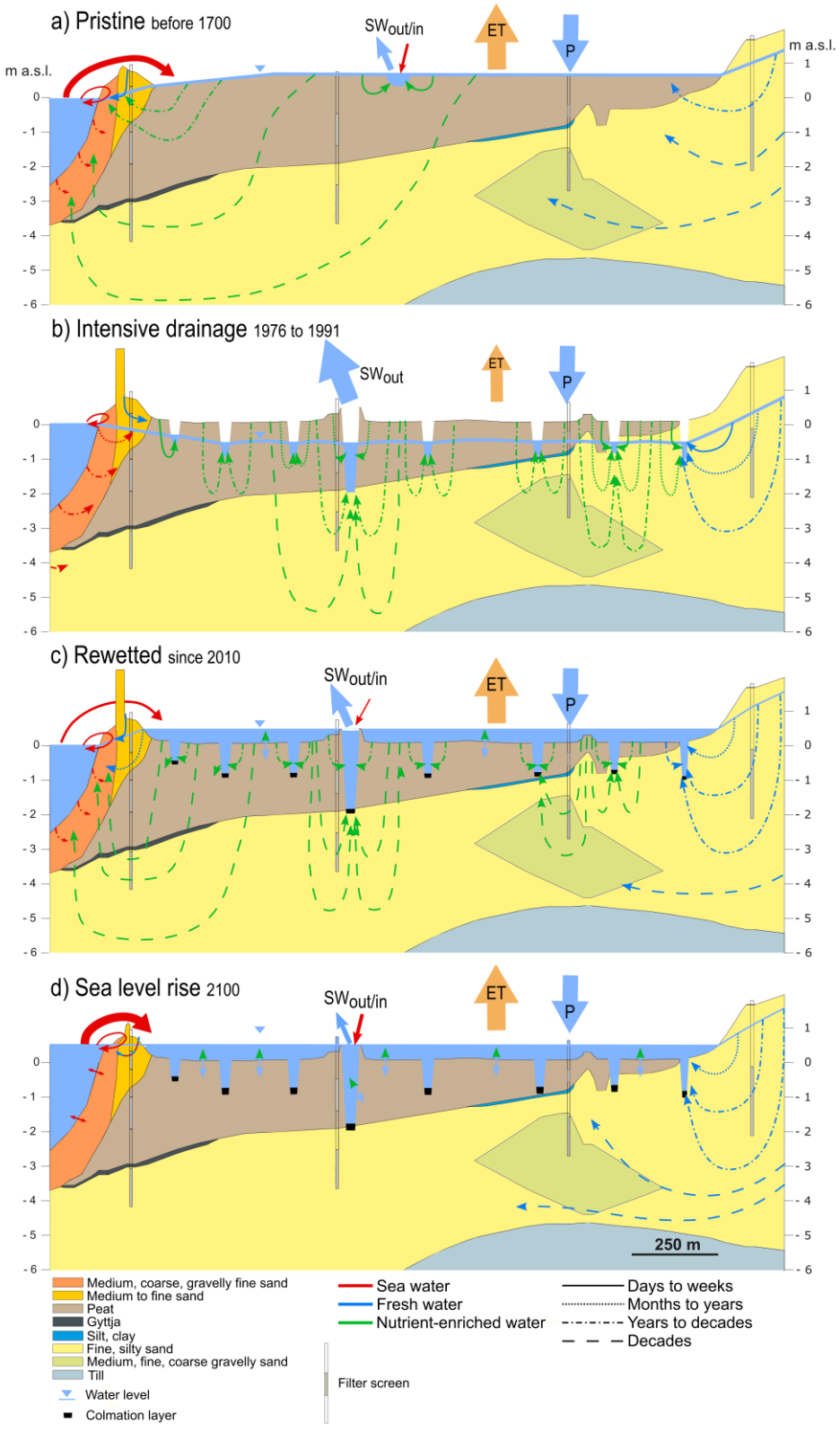

Figure 3.9: Assumed water levels and flow lines during four stages of the peatland 'Heiligensee and Hütelmoor'. Pattern and thickness of the lines indicate groundwater fluxes. Colours indicate the quality of the water. SW: Surface water, ET: Evapotranspiration, P: Precipitation.

3.2.7 Implications for SGD as a potential nutrient source

Today, a low but nearly permanent hydraulic gradient towards the Baltic Sea, and a freshening of pore waters down to 5 m depth below the shore line (Jurasinski et al. 2018) suggest the occurrence of freshwater SGD at the study site. The land-derived SGD is expected to transport nutrients and DOC into the Baltic Sea, as has been observed e.g. by (Andersen et al. 2007, Szymczycha et al. 2012). Jurasinski et al. (2018) reported enhanced methane concentrations where the peat crops out near the shore in the northern part of the coast (between B4 and B5), which were attributed to DOC input with pore water originating from the peat. A large amount of the groundwater in the aquifer recharged through the peat layer and is enriched in compounds (Table A2). At 2LS concentrations for NH_4^+ of 15 mg/L, for PO_4^{3-} of 0.7 mg/L, for DIC of 167 mg/L and for DOC of 63 mg/L were found, while the corresponding concentrations in the Baltic Sea were 0.2, 0.01, 18 and 12 mg/L. In the central peat at 7P and 6P concentrations were even higher than in the aquifer except for DIC (Table A2).

Three sources of water can be distinguished, which will undergo mixing at the coastal interface: Old, nutrient-enriched groundwater discharges from the peat and aquifer below. Precipitation leads to fresh groundwater discharge from the dune and beach sands towards the sea. Within the beach, sea water re-circulates following high sea levels.

The seaward directed discharge within the aquifer yielded in average 0.46 L/s along the 3 km long shoreline, or 13 L/d/m shoreline. Miegel et al. (2016) calculated an average discharge of 0.65 L/s (19 L/d/m shoreline) for the aquifer with slightly different parameters. The resulting average discharge in the dune yielded 2.1 L/s along the 3 km shoreline, or 60 L/d/m shoreline. In general, the groundwater flow rate within the dune dike (38 L/(m^2d)) is ten times more than within the aquifer (3.7 (L/(m^2d)). It is expected that the groundwater from the aquifer discharges over a larger area at the sea floor in a diffusive way, while the discharge from the dune dike is limited to the near shoreline and therefore is locally enhanced. So far, studies that measured or calculated SGD at the Baltic Sea yielded values of 3 to 22 L/(m^2d)

in the Bay of Puck (Szymczycha et al. 2012), 1.2 L/(m^2d) in the Eckernförde bay (Schlüter et al. 2004), and based on numerical modelling 868 m^3/d/km shoreline (with a total aquifer thickness of approx. 30 m) in Wismar bay (Schafmeister and Darsow 2011).

To emphasize the importance of spatial heterogeneity for groundwater flow along the coast, three short profiles perpendicular to the coast are depicted exemplary in Figure 3.10. At the southern part of the study site at MP3 (Fig. 3.10a), the peat layer is thin, relatively shallow and ends somewhere underneath the dune or beach. Where the peat layer ends, the groundwater from the aquifer will likely mix with freshwater recharge from the dune and recirculating sea water, before reaching the shoreline. The aquifer at MP2 (Fig. 3.10b) is shielded from surface water by the thick peat layer, which extends far into the Baltic Sea and minimises mixing of the old, nutrient-enriched groundwater with surface water. The upward directed flow through the peat will be very slow and the water composition will be altered by sea water, and freshwater discharge from the dune body once it reaches the sandy marine sediments before entering the open sea. Hence, where the lowly permeable peat layer crops out at the shallow seabed, nutrient-enriched SGD from the aquifer could occur. This geological situation is only found near the shoreline in the northern part of the study site (Fig. 3.10c). The peat layer is only slightly covered with sand where the land-derived groundwater is assumed to discharge. However, the preferential geological situation for nutrient-enriched SGD also suggests that the aquifer is not well shielded from saltwater intrusion during reversed gradients like during the drought 2018 or intensive drainage.

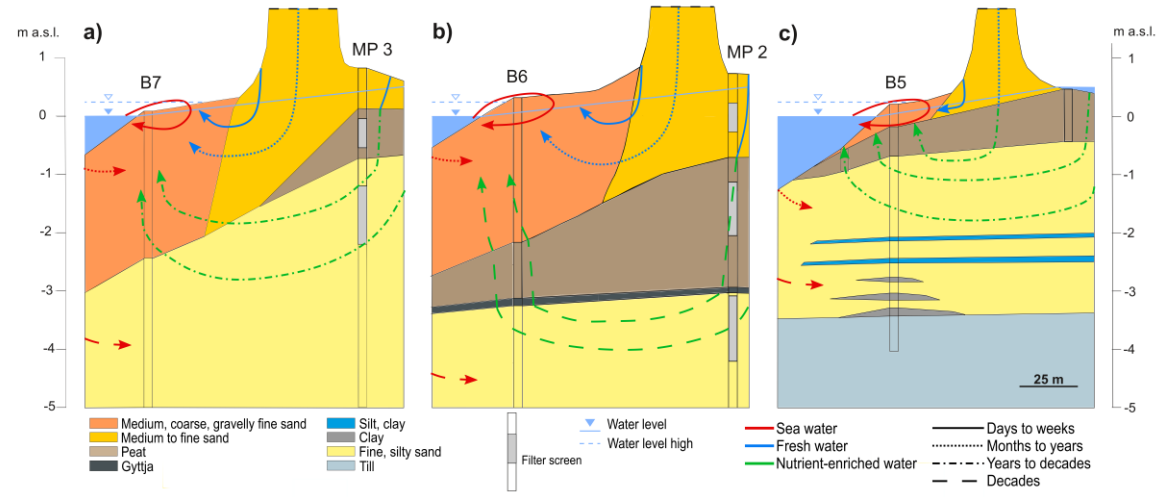

Figure 3.10: Geologic cross-sections at the coastal interface of the study site 'Heiligensee and Hütelmoor' and assumed flow lines. Pattern of the lines indicate groundwater fluxes. Colours indicate the quality of the water.

In general, the depicted and described flow paths and hence the discharge will oscillate due to the fluctuating sea level and water level on land. Transient boundary conditions due to storms, waves and the water level on the landside influence the temporal variability of the discharge towards the sea (Burnett et al. 2003). The calculated discharge from the aquifer and dune (Fig. 3.11) both increased for several weeks in March and April 2018 up to more than 1 L/s or 6L/s, respectively, but also partly in February 2017 to more than 1 L/s or 4 L/s and for a few hours to more than 1.5 L/s or 5 L/s, respectively. A single event in September 2017 led to a discharge as high as 2.1 L/s or 7 L/s, respectively. Early spring is usually characterized by high water levels on land before ET increases. At the same time storm intensity reduces and thus a relatively low and calm sea level is more likely. An enhanced discharge from the dune and aquifer is then possible, though the calculated discharge from the dune – when based on an equivalent cross-sectional area of 1 m^2 – was approximately ten times the discharge from the aquifer. It is assumed that the land-derived compounds (e.g. NH_4^+, DOC, DIC) will undergo and affect biogeochemical processes in the marine sediment, especially when in contact with the peat layer that serves as an additional carbon source (Matthias Kreuzburg,

Leibniz Institute for Baltic Sea Research Warnemünde, personal communication). The low hydraulic gradient and hence slow groundwater fluxes with at the same time high loads of land-derived compounds increases the time for biogeochemical reactions (Moore 1999, Robinson et al. 2018).

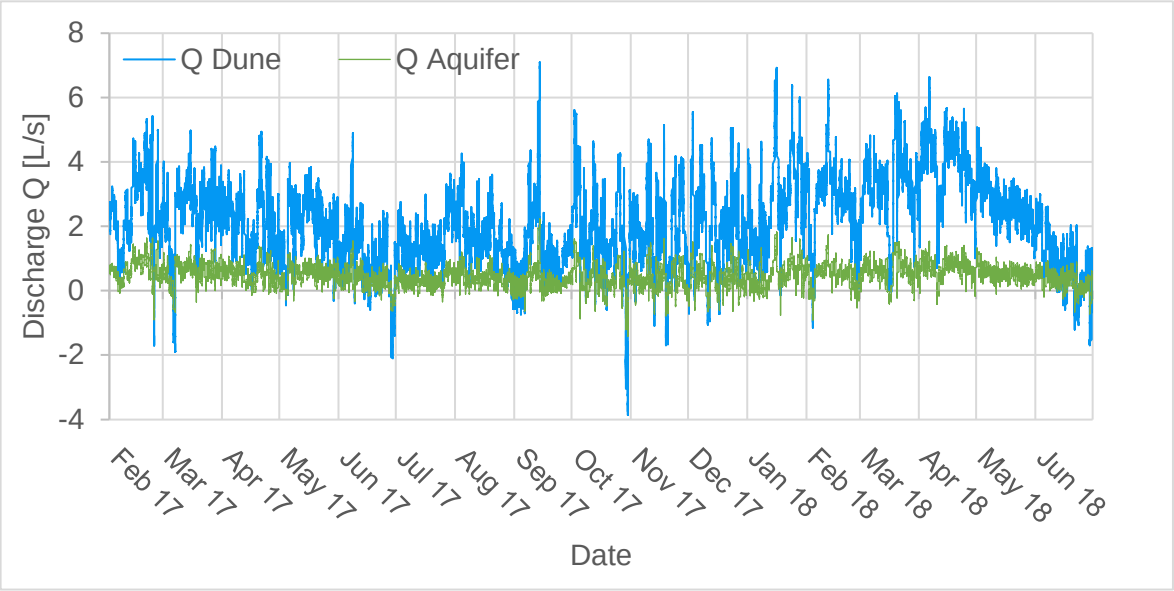

Figure 3.11: Calculated discharge Q using Darcy's law within the aquifer and dune towards the coastline.

4 3D-groundwater modelling

4.1 Modelling procedure

The model was built with Visual MODFLOW Flex (in the following VMF) which is a graphical user interface (GUI) based on MODFLOW-2005 from the USGS (United States Geological Survey). The GUI supports structures from ArcGIS and allows the building of the conceptual model independent from the numerical model grid. Different grids and grid sizes can be applied without changing the conceptual model.

In the conceptual workflow, a 3D-geological model and the hydraulic parameters of each geologic zone were defined, and boundary conditions were assigned. Afterwards the type of grid and its discretization were defined depending on the desired resolution of geological zones. The information from the conceptual model was translated into the discretized numerical model.

The calibration was achieved with the trial and error method by comparing observed and simulated heads, as well as calculated water budgets with budgets estimated from Chapter 3 and the literature. The trend of the simulated heads compared to the trend of measured heads, and the deviation from measured heads (correlation coefficient and normalized root means squared error (normalized RMS)) were used as a qualitative measure for the performance of the model.

In the first calibration step, a steady state model with a simple geology was simulated against averaged measured hydraulic heads, and hydraulic parameters were adjusted accordingly. During this step, the implementation of drainage ditches was tested and adjusted based on simulated heads and surface water discharge. To understand the effect of the interplay of input parameters (e.g. hydraulic conductivity distribution) and changes of the BC's on surface water discharge, SGD, and groundwater flow direction, a transient model was required. Therefore, the calibrated steady state model was used to simulate a period of one

month with daily, so-called stress periods. Each stress period is defined by a change of one or more BC's. The hydraulic parameters, with focus on hydraulic conductivity and storage (specific storage and specific yield), but also porosity, were further calibrated. A final validation run of one more month was done to test the model performance. The most important parameters that were not directly measured – ET rate and S_s (specific storage) – were tested in a sensitivity analysis with respect to changes in the mass balance (e.g. surface water discharge, storage change, SGD rate) and simulated hydraulic heads. Selected stress periods from the transient calibrated model with a certain constellation of BC's were further analysed regarding changing flow rates and flow paths at the interface, and within the peatland.

4.2 Conceptual model

4.2.1 Model domain

The model area was defined on the landside based on the position of observation wells MP 8, 9 and 10, which later define a BC and hence the inflow of water to the peatland. On the seaside the model boundary was defined in 0.5 km distance to the shoreline to exclude artificial artefacts from the model boundary and its BC's.

4.2.2 Geological model

Based on own geological data described in Chapter 3, literature data (Krüger 1995, Dahms 1991, Kreuzburg et al. 2018) and data from the geological survey of MV (LUNG, 2016) a 3D-geological model was built. The complete geological data can be found in Table A4 in the appendix. Four main geological zones – sand aquifer, peat, dune (and beach) and marine sediments – were defined in the beginning. Within VMF this is achieved through creating surface layers (Fig. 4.1) of the upper and lower extent of a geological zone. This defines the vertical extent. The horizontal extent within the model domain is defined by polygonal areas (Fig. 4.2). The surface layers for each geological zone were defined based on the geological data and created with the kriging method.

The first surface layer (Fig. 4.1 A) combines the topography and bathymetry: The topography data is based on the airborne satellite image (horizontal resolution 1 m x 1 m with 0.3 m accuracy, vertical accuracy: 0.15 m) from the LAIV MV (Landesamt für innere Verwaltung, Mecklenburg Vorpommern, 2015) For the dune and beach topography own levelling points were added. The marine sediment surface is based on bathymetric data (resolution: 0.5 m x 0.5 m x 0.5 m) from Kreuzburg et al. (2018). In cases where the bathymetric data are not covering the shallow coast near the beach additional data were added to create the surface (black points in Fig. 4.1 A). The data are based on own levelling points (Table A4) in the shallow coast indicating a continuous increasing depth and the assumption that a sand ridge

interrupts the continuous increase of depth as found in Kreuzburg et al. (2018). Within the peatland it was found that the data from the satellite image deviates from own levelled data. This difference could be explained by dense vegetation leading to a higher topography in the satellite image. The difference between the satellite image and the peat surface is later defined as ponding surface water.

The second and third surface layer (Fig. 4.1 B and C) represent the surface and base of the peat layer; the latter corresponds to a part of the surface of the sand aquifer. The data sources for the peat surface and base were already described in Chapter 3 (Fig. 3.4). To create the peat layer, additional points at the border of the peat were added to define the end of the layer (Fig. 4.1 B and C). The area outside of the black points in Fig. 4.1 B and C is neglected for the model set-up.

In case of the till surface (Fig. 4.1 D) more interpretation (black points) was added to the shape of the layer based on assumptions that the ancient glacial river valley continues between the forest and the coast and that the smaller ridge-valley structures also continue parallel to the deep glacial valley structure. This assumption is underlined by surface features in the peatland such as elevated topography with growing trees in the north-east ("Großer Birkhorst") and the south (actual "Hütelmoor" as described in Bohne and Bohne 2008, Fig. 4.1 D), where a shallow till layer would lead to enhanced water pondage and the development of a bog-type (upward growing) peat due to a stronger influence of precipitation as described for the Hütelmoor in Bohne and Bohne (2008). On the seaside the depth of the till layer was observed to crop out at the sea floor in the northern part (Kreuzburg et al. 2018), and the valley structures found on the landside are assumed to continue offshore, while ridges got eroded.

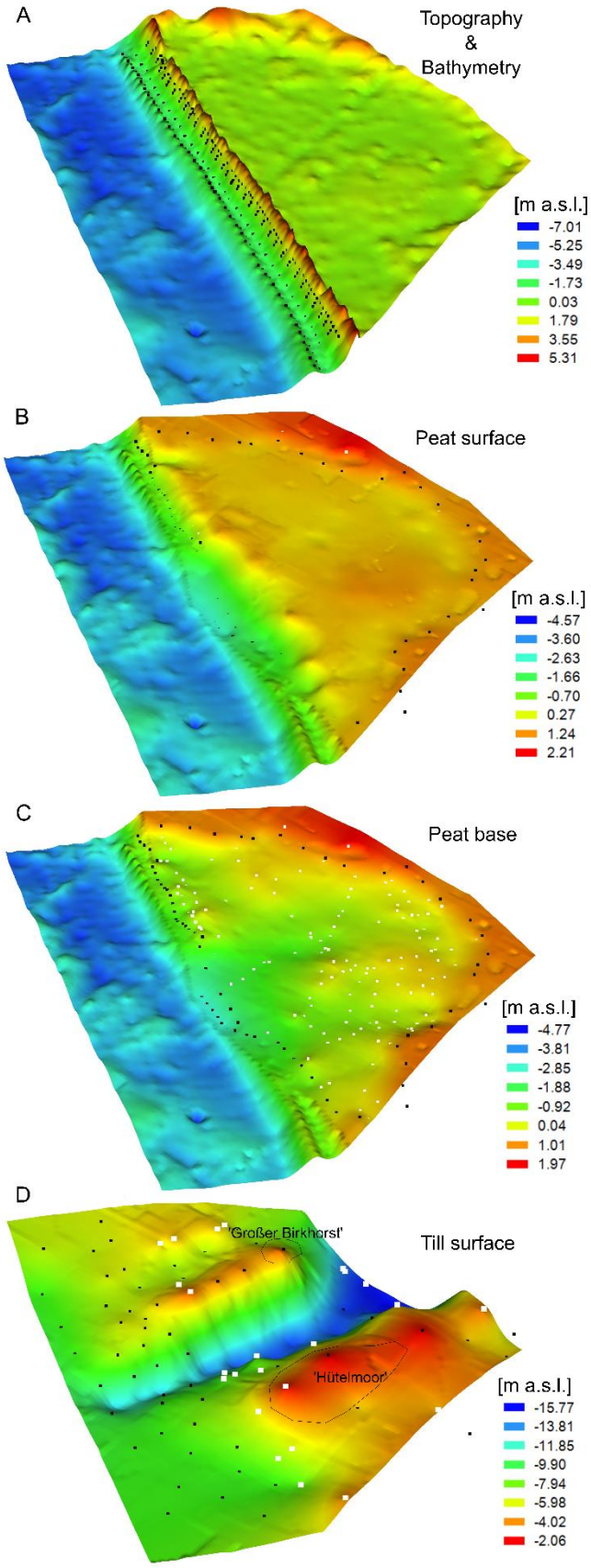

Figure 4.1: Surface layers of different geological units. Vertically 40 times exaggerated. Colour bars are different for each surface layer. White dots: drilling points, black dots: interpreted points for kriging. Note: in A) the surface is based on a complete cover of satellite imaging (1 m x 1 m, vertical accuracy 0.15 m) on the land-side, and bathymetry data (horizontal and vertical resolution 0.5 m) from Kreuzburg et al. (2018), except for the shallow coast; B) not all points are displayed, see C).

The main 4 geological zones (or hydraulic property zones) were built from the surface layers in Fig. 4.1 and the aerial extent (Fig. 4.2) as summarized in Table 4.1.

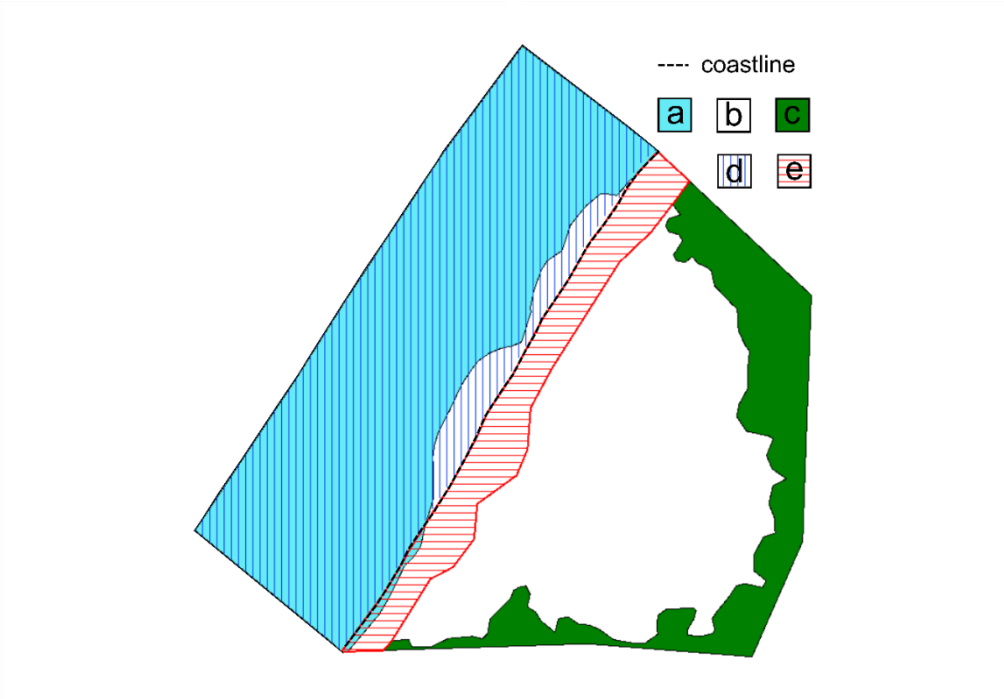

Figure 4.2: Polygonal areas to define the extent of geological zones. Note that polygon b (white) intersects polygon e and partly polygon d, and polygon a lie within polygon d.

Table 4.1: Hydraulic property zones of the 3D-geological model.

Hydraulic property zone	**Upper surface layer (Fig. 4.1)**	**Lower surface layer (Fig. 4.1)**	**Polygonal extent (Fig. 4.2)**
Peat zone	B (Peat surface)	C (Peat base)	b
Aquifer zone	A (Topography & Bathymetry)	D (Till surface)	c
	C (Peat base)	D (Till surface)	b
Dune dike - beach zone	A (Topography & Bathymetry)	B (Peat surface)	e
Marine sediment	A (Topography & Bathymetry)	D (Till surface)	a
	A (Topography & Bathymetry)	B (Peat surface)	d (only new information where d intersects b)

The geological model (Fig. 4.3) visualizes the 4 main hydraulic property zones. The spatial extent of the Baltic Sea is later defined within polygon *d* (Fig. 4.2) between surface layer *Topography & Bathymetry* (Fig. 4.1) and a surface of constant height of 1 m. The aquifer (Table 4.1) was assumed to continue offshore below the peat as found in Kreuzburg et al. (2018). The spatially varying geometry of the aquifer and peat are further visualized in Figure 4.4.

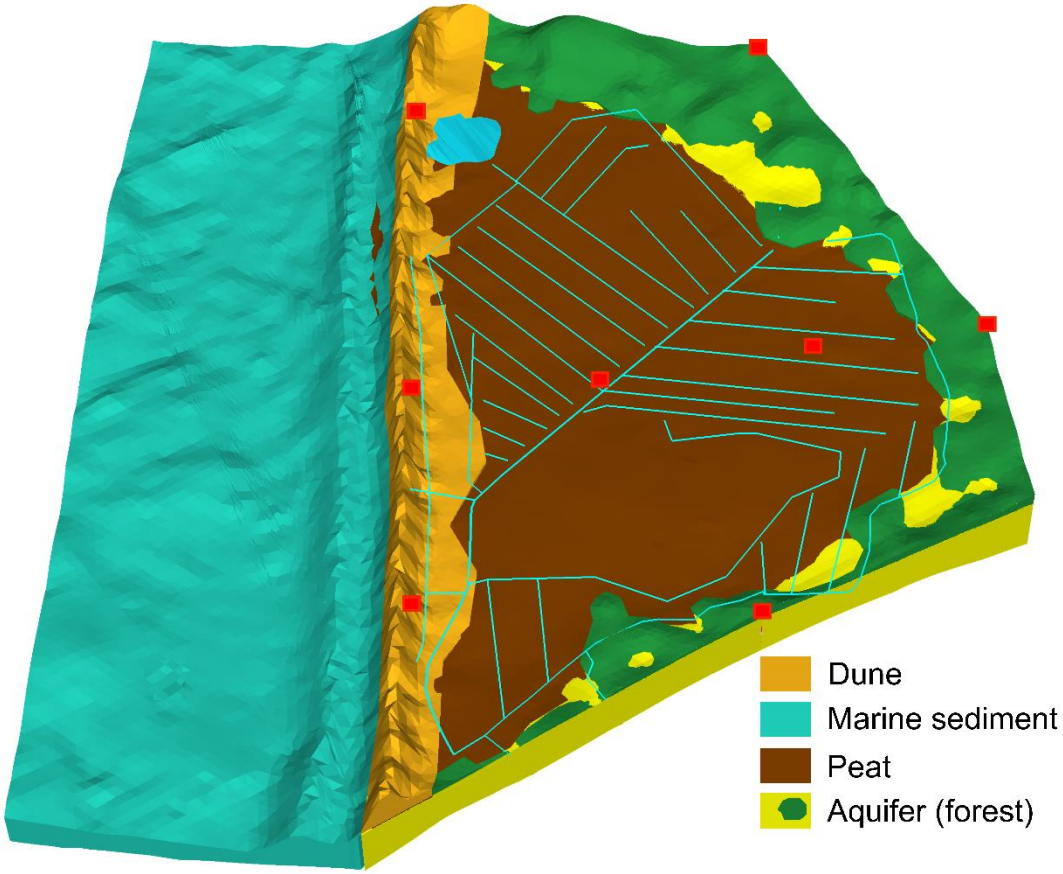

Figure 4.3: 3D-geological model with ditches, lake (blue) and observation wells (red) for orientation (vertically 40 times exaggerated).

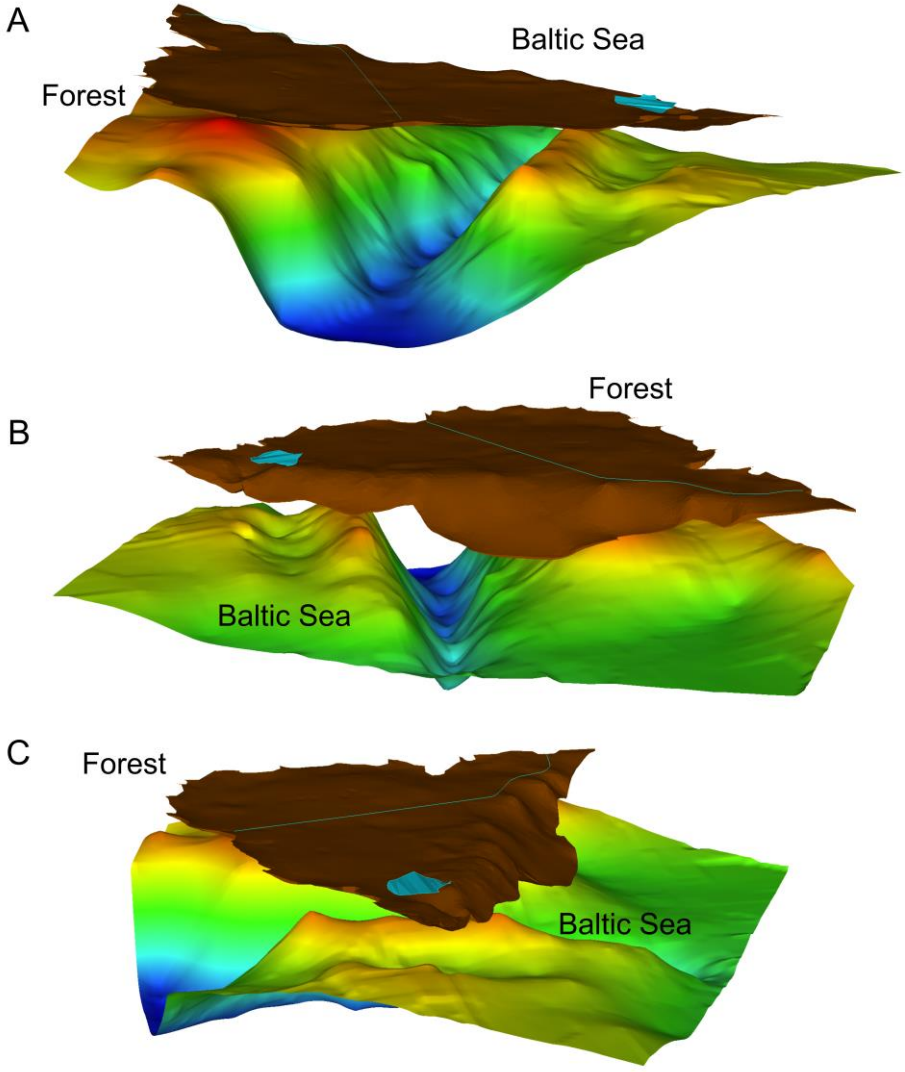

Figure 4.4: Peat (brown) and surface of till layer (coloured) representing the base of the aquifer from three different perspectives (A-C). Lake and main ditch (blue) for orientation. Vertically 40 times exaggerated.

4.2.3 Hydraulic parameters

The required hydraulic parameters were hydraulic conductivity (K_x, K_y, K_z) for steady state simulations, and additionally specific yield (S_y), specific storage (S_s), for transient simulations. Effective porosity (n_e) for particle tracking with MODPATH and total porosity (n_{tot}) needed for variable density-dependent flow with SEAWAT – though not applied anymore in this study – were also defined. The aquifer, dune and marine sediments were assigned each with homogeneously distributed hydraulic parameters and were assumed to be isotropic due to low compaction. The

parameters were chosen based on slug tests, grain size analysis, literature data, and adjusted during the calibration process. The assigned values were summarized in tables for each simulation in the respective chapters.

The slug test-derived radial K in the aquifer ranged between $2*10^{-6}$ and $3*10^{-5}$ m/s. The lowest values were found at 3LS and MP 8. At the other wells, K was between $1.2*10^{-5}$ and $3*10^{-5}$ m/s. The K derived by grain size analysis was often higher with around $6*10^{-5}$ m/s. Hence a high K of $6*10^{-5}$ m/s and a low K of $2*10^{-5}$ m/s were tested in the calibration and better results were obtained for a K of $2*10^{-5}$ m/s.

For the dune the slug test indicated a K of $5.4*10^{-5}$ m/s at 1DS, and the grain size analysis a K of $2*10^{-4}$ m/s at 2DS (slug test not evaluated due to shallow depth). The grain size analysis of the coarser upper sediments at the beach (sediment cores along profile B in Fig. 3.2) resulted in K values of $6*10^{-4}$ m/s. Within the model set-up the beach area is not further distinguished and belongs to the dune area. Kreuzburg et al. (2018) showed that marine surface sediments at the study site were heterogeneous from fine to coarse material, but little is known about the grain size distribution in greater depth. In the shallow sea close to the shoreline, where most of the SGD is expected, no information on grain size distribution was available. Due to also fine material a lower K of $1*10^{-4}$ m/s was assumed for the whole marine sediment.

K of the peat was tested during the calibration based on slug test results. A K at 7P and 6P was not estimated properly because the KGS model (Chapter 3.1.4) did not converge. One reason could be that at 6P and 7P the surface water was frozen when the slug tests were performed, while all other slug tests were done in greater depth or on other days. The results for 3P and 2P indicate a K of 10^{-7} to 10^{-8} m/s, respectively, though the results are based only on the faster, early stage of the slug test. The water level recordings indicate a very slow recovery of several days at 2P (Fig. 3.6), which indicates a lower K than 10^{-8} m/s. A comparison of the water level drawdown curves of 6P and 7P with results of 3P and 2P indicates a faster recovery and hence a higher K in the less compacted peat at 6P and 7P, which might be

around 10^{-6} m/s. Hence, in the calibration a first simulation – case I – was done with a homogeneous distribution of K of 10^{-7} m/s, followed by case II with a zonation of K for the peat.

The storage parameters for mineral sediments (final calibrated values in Table 4.3) were assigned based on literature data (Johnson 1967, Hölting and Coldewey 2013). In case of the fen peat, literature values were considered, but the uncertainty due to the heterogeneity of peat, and different peat types reported in the literature, is high. Porosity and storativity depend on the degree of compaction of peat. For decomposed fen peat, porosity can be as high as 0.89 (Gosch et al. 2018), while Kleimeier et al. (2017) reported a porosity of 0.61 for a decomposed fen. Hence, porosity values were assigned relative to K values estimated in the calibration. Despite a high porosity of peat, n_e (and K as seen in the slug tests) can be rather low due to poorly connected pores (Loxham 1980, Reynolds et al. 1992, Ours et al. 1997). For n_e Hoag and Price (1997) reported a value of 0.12 for decomposed catotelm peat (bog) and Siegel and Glaser (1987) assumed a value of 0.1. Since n_e corresponds to the drainable pore volume, it was set equal to S_y – the storage changes due to drainage. S_y values between 0.048 to 0.55 Price (1996) were found for bog peat. During the calibration it was considered that roots of reed and sedges in the upper peat could lead to better connected pores despite decomposition. S_s is less studied for peat, because it is difficult to estimate. However, storage changes due to compression over the total depth of the peat can be more important than S_y (Price and Schlotzhauer 1999). Price and Schlotzhauer (1999) estimated a storativity due to S_s over a peat thickness of 1.75 m of 0.13, and for the same peat a S_y of 0.048 was reported by Price (1996).

Surface water zones – Baltic Sea, drainage ditches, ponding water in the peatland – are incorporated and defined as highly conductive zones. Implementing surface water as a highly conductive zone was achieved in other modelling approaches (Anderson et al. 2002, Yihdego and Becht 2013). This has the advantage that water can flow between sediments and a surface water body to estimate exchange rates. Flow within the highly conductive zones is not representative for surface water

flow (Anderson et al. 2002). The implementation of ditches was done manually after the grid was defined. For surface water bodies K was set to 10 m/s, S_s to 10^{-6} m^{-1}, and all other parameters were set to 1.

4.2.4 Boundary conditions

4.2.4.1 Simulated period

A steady state simulation was done with averaged hydraulic heads for the period between 24.3.2017 and 31.5.2018. In this period data from all wells was available, while the period after May 2018 was unusually dry and water levels dropped considerably (see Fig. 3.5).

For the transient simulation with daily stress periods the time period 24.3.17 to 20.4.2017 was chosen because the averaged water levels for this period were close to the averaged water levels of the period from 24.3.2017 to 31.5.2018. Hence, no preliminary simulation time was needed to consider long-term effects like accumulation of recharge events or droughts on the actual simulated period of one month. The hydraulic heads and the sea level used as BC's or observation data to estimate the quality of the simulation were measured in a 15-minute interval. To obtain an averaged head for each simulated day (or stress period) a running-mean of 3 days was applied to the measured heads and the sea level.

For the validation, an additional month from 21.4.2017 to 20.5.2017 was simulated.

4.2.4.2 Constant head BC

A first-type BC or constant-head (CHD) BC was assigned at the part of the model boundary that covers the landside. The CHD was defined by the hydraulic heads measured at observation wells MP 8, 9, 10 and the sea level at the coastline (Fig. 4.5). Between the points the CHD was linearly interpolated (Fig. 4.5). This was assumed to best represent the distributed water levels in the forest and hence the inflowing amount of groundwater to the peatland. The continuous extent of the

CHD BC to the coastline is needed to represent enough inflowing water from the surrounding higher elevated forest. An additional point as part of the landside CHD BC was defined at the lower western edge (Fig. 4.5). It was set equal to the head of MP 9 due to similar topographic elevation and distance to the peatland.

On the seaside, a CHD BC equal to the sea level was assigned over the whole length of the model boundary parallel to the coastline (Fig. 4.5).

In vertical direction the CHD BC's were assigned between the minimum-height of sea level to the bottom of the aquifer.

For the steady state simulation averaged hydraulic heads for the period between 24.3.2017 and 31.5.2018 were assigned, i.e. 2.35 m at MP 8, 1.17 m at MP 9, 0.95 m at MP 10, and 0.11 m for the sea level (equal to freshwater head in 1 m depth). The values for the transient simulation are shown in Fig. 4.6. The groundwater flow model does not simulate equivalent freshwater heads.

4.2.4.3 No-flow BC

The model boundaries on the seaside perpendicular to the shoreline were assigned as no-flow BC's. The bottom of the model domain (impermeable till) was automatically defined as impermeable.

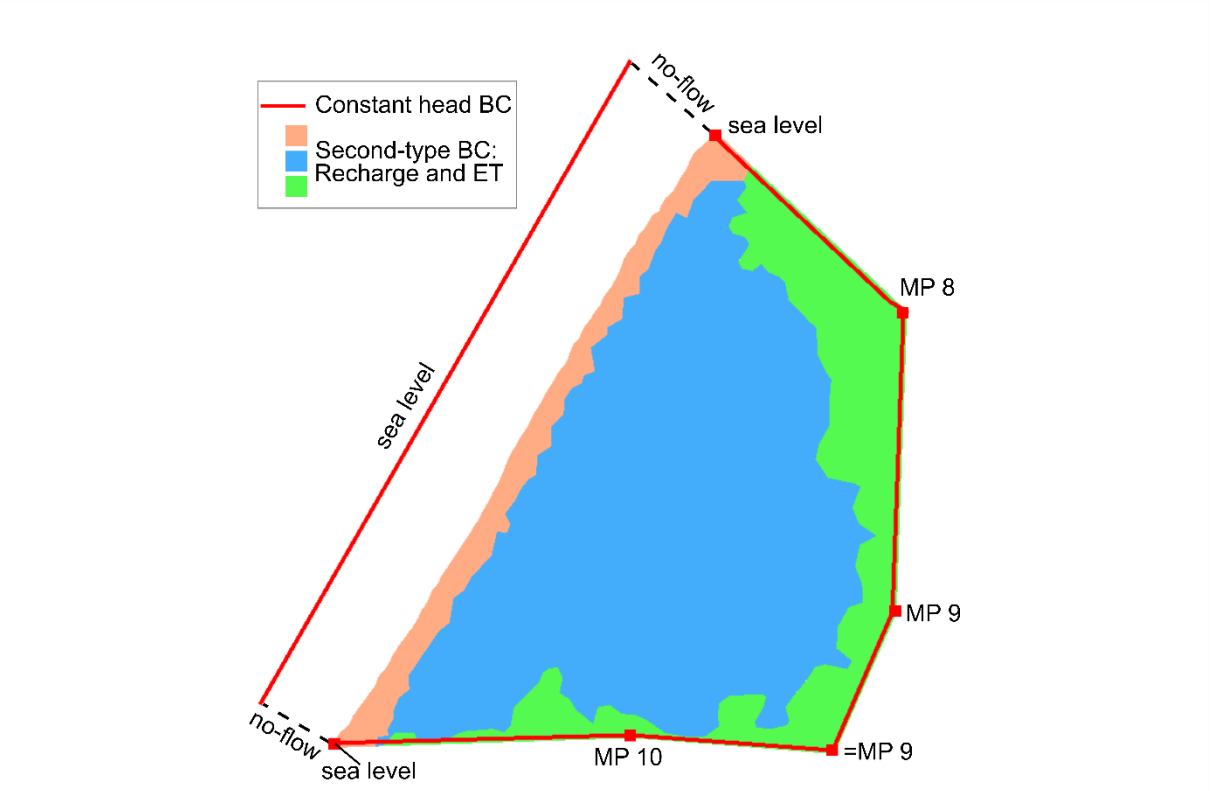

Figure 4.5: Location of assigned boundary conditions: Constant-head BC's (red lines) and Recharge and ET (coloured polygons).

4.2.4.4 Evaporation and recharge rates

Second-type BC's for ET and recharge were assigned with different rates for forest, peatland and the dune-beach area (indicated as zones in Fig. 4.5). Recharge is calculated by subtracting ET from precipitation. If recharge dominates, ET is set to zero, and if ET dominates, recharge is set to zero. Surface water discharge is implemented in a separated way into the model and is therefore not considered in the calculation of recharge. The estimation of the actual ET requires labour-intensive field measurements on a regular base, which was not feasible. However, the potential ET (ET_{pot}) is a good estimate if it is assumed that enough water is supplied to the area. For the transient simulation in spring it is assumed that enough water is supplied to the area. Because of the difficulty to estimate the actual ET,

recharge and ET are usually a calibration parameter as well, and a sensitivity analysis for these parameters was performed.

ET_{pot} was calculated on a daily base with the semi-empiric Penman combination equation (Penman 1948), which is based on a radiative energy balance. The required parameters temperature, precipitation, wind velocity (corrected to 2 m height according to Häckel (1999) found in Miegel et al. (2016)), humidity and sunshine duration were provided on a daily base by the German Weather Service (Deutscher Wetterdienst 2018) at the station Warnemünde. Values for extra-terrestrial solar radiation were obtained from Iqbal (1983). Further, the albedo α and the emissivity ε of an object or surface (vegetation, soil or water surface) were taken from literature.

The albedo describes the reflection of solar radiation (Sumner 2000). It varies with the angle of the incoming solar radiations, cloud cover, type of surface (roughness, shininess) (Sumner 2000, Otto et al. 2014) and soil humidity (van Wijk and Ubing 1963). Here it will be differentiated between i) the dune area with sand and dune grass (assumed α of 0.22 after Stoutjesdijk and Barkman (2014); ii) the peatland with areas of phragmites in winter (α of 0.21, Smid 1975) and summer time (α of 0.18, Smid 1975) and areas (approximately one third after Miegel et al. 2016) of open surface water (α of 0.06 to 0.37 depending on the month, Cogley 1979); as well as iii) the broadleaf-dominated forest (winter 0.15 and summer 0.2, Oke 1978). For emissivity, which is the effectiveness of emitting energy as thermal radiation, an average value of 0.98 was used for the peatland and the forest based on values from Oke (1978) and a value of 0.95 was assumed for the dune area.

For the steady state simulation, the average calculated recharge for the dune was 0.17 mm/d, and for the peat and forest 0 mm/d. ET was set in all cases to 0. Recharge and ET rates for the transient simulation period (24.3.2017 to 20.4.2017) are shown in Fig. 4.6.

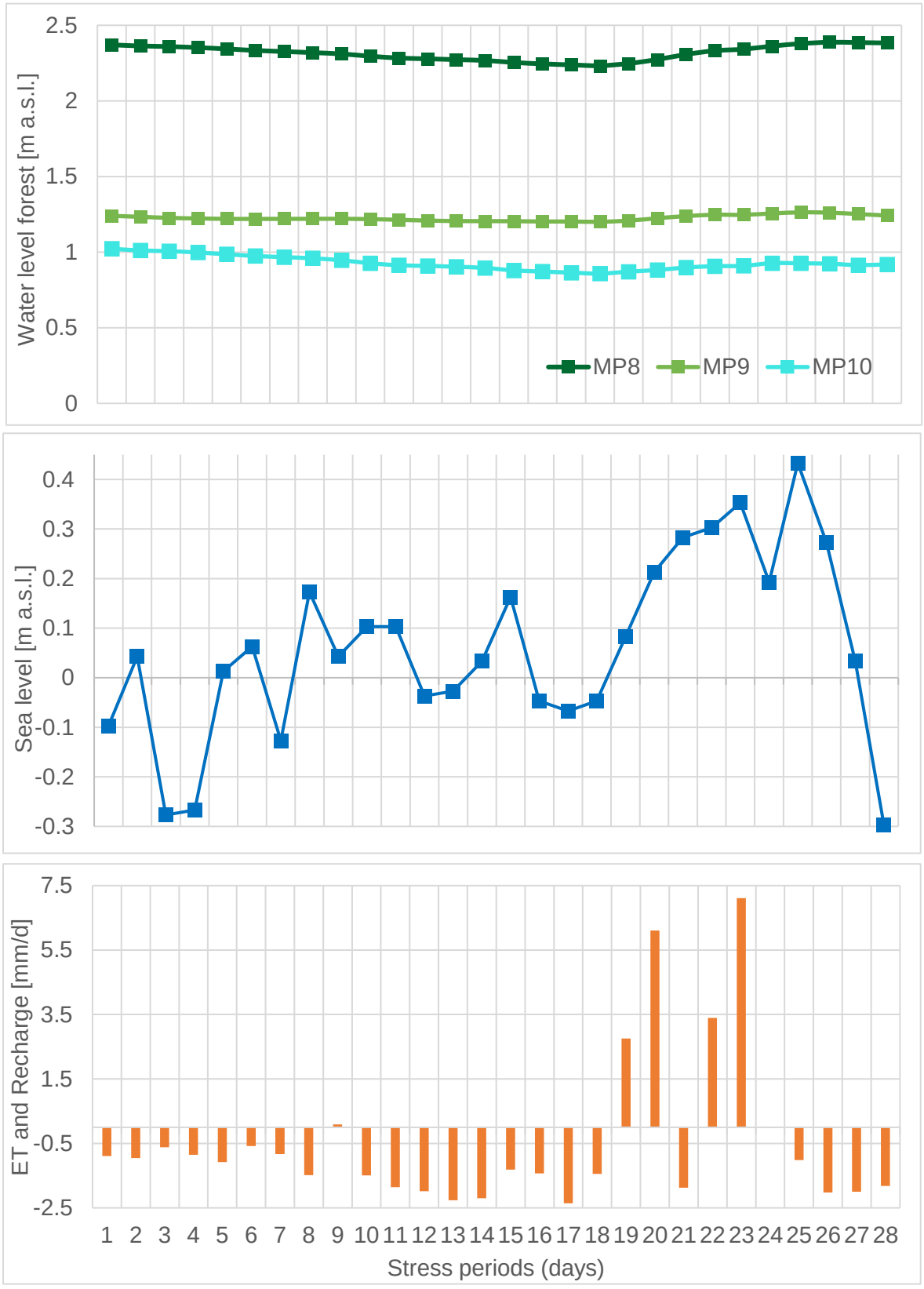

Figure 4.6: Assigned values for transient boundary conditions. ET (negative) and recharge (positive) are exemplary shown for the peat zone. Simulation period: 24.3.2017 to 20.4.2017.

4.3 Numerical model

4.3.1 Groundwater flow equation

MODFLOW is based on the partial-differential equation for saturated groundwater flow described in McDonald and Harbaugh (1988):

$$\frac{\delta}{\delta x}\left(K_{xx}\frac{\delta h}{\delta x}\right)+\frac{\delta}{\delta y}\left(K_{yy}\frac{\delta h}{\delta y}\right)+\frac{\delta}{\delta z}\left(K_{zz}\frac{\delta h}{\delta z}\right)+W=S_S\frac{\delta h}{\delta t} \tag{4.1}$$

Where K_{xx}, K_{yy}, K_{zz} represent the hydraulic conductivity [L/T] along the x, y and z coordinate axes, h is the hydraulic head [L], W are sink and sources [T^{-1}], S_S is the specific storage [L^{-1}] and t is time [T].

Based on the partial-differential groundwater flow equation the finite-difference equation (McDonald and Harbaugh 1988) is solved for each grid cell, i.e. between the cell node and neighbouring nodes along x-, y-, and z-direction. The calculation is done in an internal flow package. Here, the block-centred flow package (BCF6) was used. For further details, see Harbaugh et al. (2000).

4.3.2 Particle tracking using MODPATH

For each cell flow rates along x-, y-, and z-direction are calculated in MODFLOW. MODPATH (Pollock 2016) calculates flow velocities based on the Darcy flux q [L/T] and the effective porosity n_e [-] for each direction:

$$\vec{v_a}=\frac{\vec{q}}{n_e} \tag{4.2}$$

The velocity vectors of the three directions x, y, z of a cell are linear interpolated and a flow direction of a (water) particle in the cell is calculated. The position of the

particle can be calculated for each time step from the recharge of the particle to its discharge point in the model domain using backward and forward tracking. The advective age of water at a certain location can be calculated using backward tracking of several particles.

4.3.3 Finite-difference grid

A finite-difference grid of uniform cell distribution (Fig. 4.7), i.e. no vertical offset, was used for discretization to ensure numerical stability. A uniform finite difference grid requires a finer vertical discretization and manual adjustments of the correct assignment of parameter distribution (e.g. K and porosity), while a deformed grid (vertical offset) needs less cells and automatically implements complex geological layering. However, the deformed grid might lead to instabilities when simulating mass transport or density-dependent flow (VMF Manual 6.0). Additionally, a fine discretization of the uniform finite-difference grid would be necessary to simulate transport or variable density flow, where highly conductive zones exist next to low conductive zones, as it is the case at the sea-sediment interface.

In vertical direction the cell size was 0.25 m down to a depth of -5 m, and afterwards increased to 0.5 m. The fine discretization in the upper part ensured to depict the depth of ditches and the geometry of peat and aquifer as well as the bathymetry of the shallow coast. In total, 60 layers were defined, 208 rows along NE-SW direction (parallel to coastline) and 196 columns along NW-SE direction (vertical to coastline) with a total number of 971,177 active nodes. The columns always had a width of 17 m while the rows at the coastal interface were discretized as fine as 5 m to depict the extent of the outcropping peat layer in the shallow coast, and increased to 20 m width in the Baltic Sea and in the peatland (see Fig. 4.7).

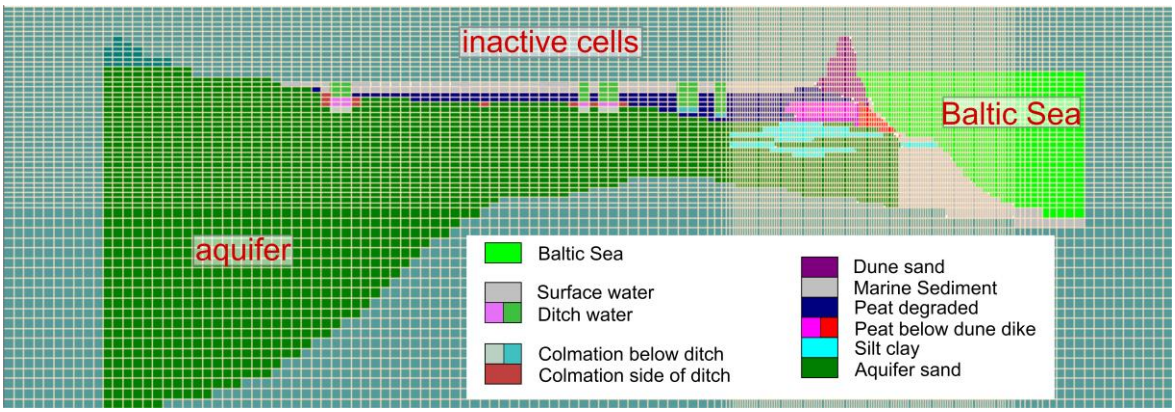

Figure 4.7: Grid resolution along a column and in vertical direction (vertically 20 times exaggerated). Refinement of row width visible at the coastal interface.

4.3.4 Initial Conditions

Initial heads were defined for each active model cell and were set to 0.5 m for the steady state simulation. For the transient simulation, a previous steady state simulation was used to define the initial heads for each cell.

4.3.5 Calculation of the water balance

Within VMF, a mass balance with volumetric flow [L^3] and flow rates [L^3/T] for each stress period (1 day) was calculated for the whole model domain. This included the water in- and outflow via CHD-BC's, storage, recharge (no outflow), ET (no inflow) and the total in- and outflow, which was equal unless storage has changed. In a steady-state, model storage is excluded from the mass balance. Furthermore, water budgets were calculated for sub-classified zones with the Zonebudget package (Harbaugh 1990). The exchange with neighbouring zones was also calculated.

The Baltic Sea was classified as one zone, and the sediment (land- and seaside) was sub-divided layer-wise (depth-wise) into zones. In the following, the flow from the sediment to the Baltic Sea was assumed to be equal to SGD, and the flow from the Baltic Sea to the sediment was assumed to be equal to SWI (seawater intrusion). Further, the inflow from the CHD-BC on the landside was distinguished from the inflow from the CHD-BC on the seaside. The flow from the forest (CHD-BC)

towards the peatland was defined as Q_{in} in the following. The surface water discharge Q_{SW} was initially estimated with the River package and later was calculated with the Zonebudget package (which is explained in more detail in the next chapter). Hence, the water balance for the peatland, including the underlying aquifer and marine sediments, is as follows:

$$Q_{in} + Recharge - ET - Q_{SW} - SGD + SWI = \Delta S \quad (4.3)$$

ΔS is the storage change that mainly is due to changes of storage in the surface water of the peatland, where S_y is set to 1.

The whole water balance is only calculated for the final calibrated transient model.

4.3.6 Boundary Conditions

4.3.6.1 Constant-head

Constant-heads were assigned as first-type boundary conditions at the cells as defined in Fig. 4.5 and linearly interpolated between the points (see Chapter 4.2.4.1).

4.3.6.2 Recharge and evaporation

Recharge and ET rates were assigned as a second-type BC at the uppermost active and wet cells according to the zones in Fig. 4.5. The Recharge package (McDonald and Harbaugh 1988) requires only the rate of recharge that is then calculated for each cell depending on the cell size. The Evapotranspiration package (McDonald and Harbaugh 1988) calculates the loss of water depending on the assigned maximum value of ET and the extinction depth (EXDP). The defined ET rate assigned to the uppermost saturated layer decreases along the user-defined EXDP linearly to 0 (McDonald and Harbaugh 1988). An EXDP of 0.1 m was assigned for the dune and the forest, and an EXDP of 0.6 m for the peat with ponding surface

water. The total amount of water loss due to ET can therefore be adjusted through changing EXDP. The effect of changes on the water balance was tested in a sensitivity analysis.

4.3.6.3 Surface water discharge

4.3.6.3.1 High conductivity approach with the River package

The ditches were first implemented as a third-type BC which required the assignment of a constant-head at each grid cell that was defined as a River BC. The constant-heads were assigned in the same way as for the linear interpolated CHD-BC along polylines representing the ditches as in Fig. 4.3. Further, the cells above the River BC had to be turned into highly conductive cells with a K of 10 m/s (e.g. Fig. 4.7), because the actual ditches (0.5 to 2 m depth) are deeper than the cell (0.25 m thick) the River BC was assigned to. The assigned hydraulic head (H_{Riv}) and a conductance term (C_{Riv}) at each cell define the volume of water either flowing into the peat or sand below, or that is taken out of the cell, and in their sum should equal the surface water discharge at the ground sill. This relationship is described in the following (McDonald and Harbaugh 1988):

$$Q_{Riv} = C_{Riv} (H_{Riv} - h_{i,j,k}) \tag{4.4}$$

where Q_{Riv} is the flow between river and aquifer [L^3/T], C_{Riv} is the hydraulic conductance of the river-aquifer interconnection (river bed) [L^2/T], H_{Riv} is the water level in the river [L], and $h_{i,j,k}$ is the head in the cell underlying the river reach

The hydraulic conductance C_{Riv} is further calculated as follows:

$$C_{Riv} = \frac{K\ L\ W}{M} \tag{4.5}$$

where K is the hydraulic conductivity [L/T] of the riverbed; L, W and M [m] are the length, width, and thickness of the conductance block (riverbed).

H_{Riv} was assigned based on hydraulic heads observed in the central peatland at D_{ctr} (0.535 m) and upstream of the ground sill at D_{out1} (0.525 m a.s.l.) for the steady state simulation. The ditch level at the border to the forest was assumed to be 0.545 m a.s.l.. For each polyline that represents a ditch (Fig. 4.3), a value for H_{Riv} (and C_{Riv}) was defined at the beginning and the ending of the polyline. These values were estimated from the assumed hydraulic head gradient of 0.02 m between forest and ground sill. The geometry of ditches was defined based on the measured depth and width (the length was defined by the polyline) for small ditches (depth 0.5 to 1 m, width 2 to 3 m) and the main ditch (depth 2 m, width 10 m). The thickness of the riverbed was 0.1 m. A K of 10^{-5} m/s and 10^{-6} m/s for the riverbed was tested during the calibration. A disadvantage of this way of implementing the ditches is however, that the water level for each grid cell of the ditch system is defined prior to simulation, which is basically unknown.

4.3.6.3.2 High conductivity approach without the River package

To obtain a more realistic and dynamic head-distribution, a second way of implementing the ditches was tested, where the hydraulic gradient in the ditch system was solely defined by a CHD-BC at the border of the model, where the ground sill is located. The CHD was assigned according to the measured water level upstream of the ground sill (D_{out1}). The surface water discharge was calculated with the Zonebudget package (Harbaugh 1990) at the outlet (Fig. 4.8). Due to the large grid cells in horizontal directions, the ditches were too wide and could lead to unrealistic high infiltration of water from the surrounding sediments. Therefore, the interaction with the more permeable sand is controlled by a low conductive layer below all ditches and next to the ditches in case of sand (Fig. 4.9). The bottom cells were assigned a K of $1*10^{-6}$ m/s. The cells next to the ditches in the aquifer near the forest were assigned only with a K of $5*10^{-5}$ m/s. This might be because the forest

is actually drained by many ditches, while in this model set-up more groundwater is supplied to the peatland. Besides a higher K at the ditch walls, a few ditches were also implemented in the forest and connected to the ditch system to lower the water level in the peatland.

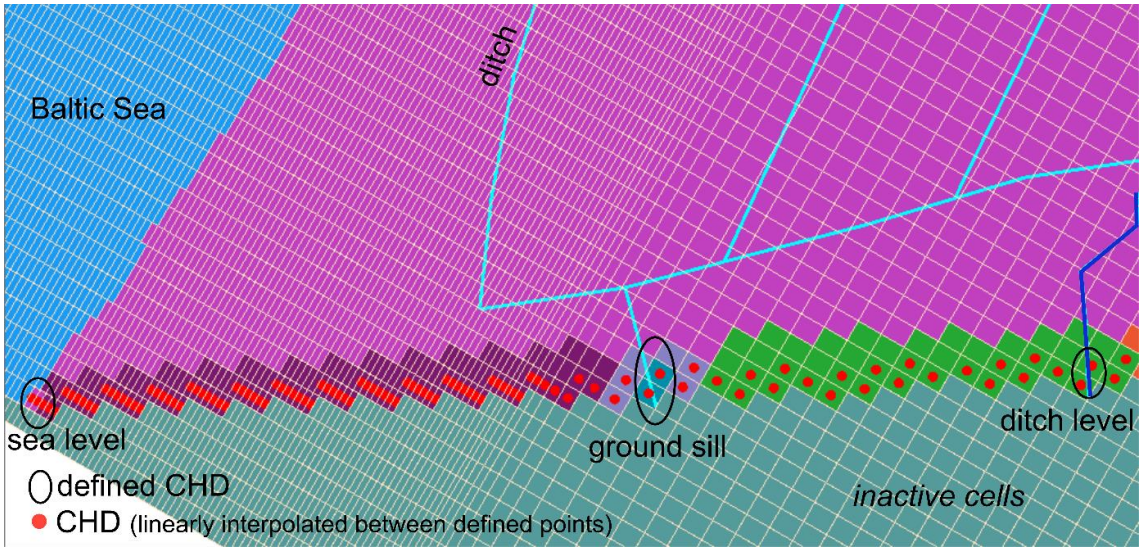

Figure 4.8: Zones for Zone Budgets (different colours) and constant-head boundary conditions (red dots). Blue lines indicate location of ditches. Dark blue line: Ditch is not assigned in terms of K but it defines a CHD at the boundary equal to the water level upstream of the ground sill. No discharge out of the catchment appears via this ditch.

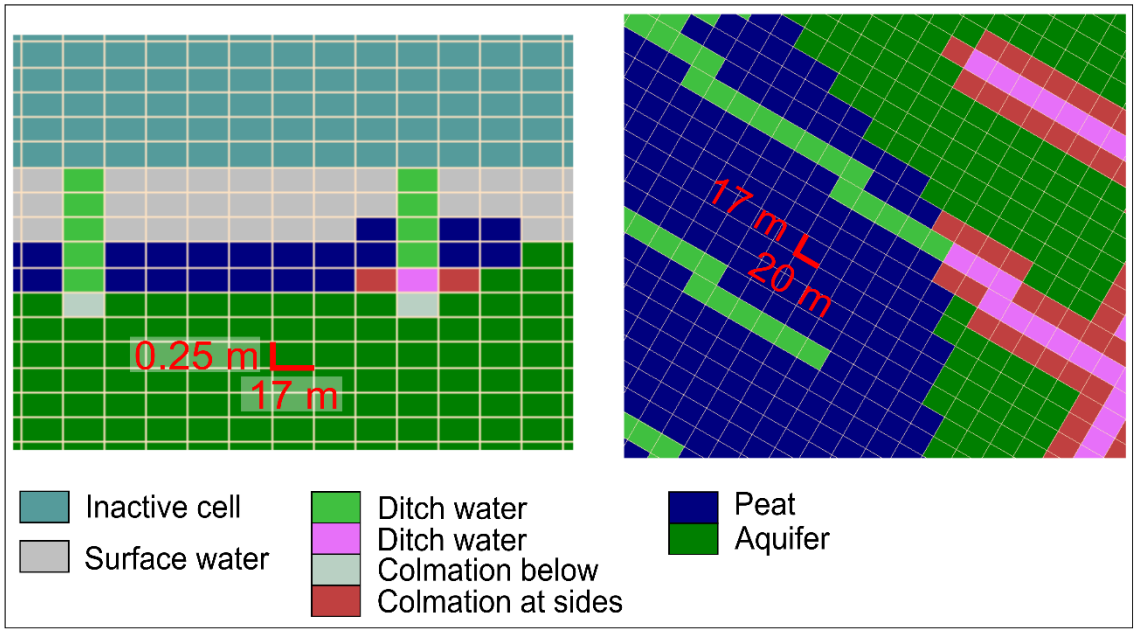

Figure 4.9: Implementation and discretization of ditches as high conductive zones. Different colours (zones) for the ditch water were used to be able to switch the cells easily back to its surrounding substrate.

4.3.7 Solver, convergence criteria and time step scheme

The BiCGSTAB (preconditioned bi-conjugate gradient stabilized method) - P Matrix Solver (WHS package, Visual MODFLOW Flex User Manual 6.0) was used because it converges faster and is more stable for larger grids than the PCG (preconditioned conjugate gradient) solver for example. The convergence or closure criteria for head change (HCLOSE) and residual (RCLOSE) were both set to $1*10^{-5}$ ([m] and [m^3/d], respectively).

The transient model with 28 stress periods (28 days) was run with 10 time steps for each stress period and a multiplier of 1.2. Convergence problems for stress periods with strong changes of a BC (e.g. high recharge or sea level) were solved either by adjusting time steps or the rewetting settings (mainly wetting factor). Rewetting, that defines when a dry cell is turned to a wet cell, is applied with a wetting factor of 0.001, and wetting from sides and below. With these rewetting settings, only 10 time steps were needed.

4.4 Calibration

4.4.1 Steady state calibration

In the steady state calibration information was implemented stepwise. 5 selected cases will be discussed in more detail. Case I and II differed in terms of geological zonation, case II.1 to II.3 are based on case II but focus on how to implement the ditch system. The different input parameters of the 5 cases were summarized in Table 4.1. The simulated hydraulic heads and errors will only be presented in detail for case I and case II.3. Case II.1 to II.3 focus on the ditch system and amount of discharge and have a minor effect on the hydraulic heads near the coast.

Table 4.2: Hydraulic conductivity in m/s for the different cases I to II.3 of the calibration.

Hydraulic property zone	Case I	Case II	Case II 1	Case II 2	Case II 3
Peat degraded	10^{-7}	10^{-7}	10^{-7}	10^{-7}	10^{-7}
Peat > 2 m depth	n.c. (= degraded peat)	10^{-8}	10^{-8}	10^{-8}	10^{-8}
Peat below dune dike	n.c. (= degraded peat)	10^{-8}	10^{-8}	10^{-8}	10^{-8}
Silt clay	n.c. (= aquifer)	$5*10^{-8}$	$5*10^{-8}$	$5*10^{-8}$	$5*10^{-8}$
Aquifer (fS,Si)	$2*10^{-5}$	$2*10^{-5}$	$2*10^{-5}$	$2*10^{-5}$	$2*10^{-5}$
Dune (mS, fs)	10^{-4}	10^{-4}	10^{-4}	10^{-4}	10^{-4}
Marine sediment (mS, cS, fS, gravel)	10^{-4}	10^{-4}	10^{-4}	10^{-4}	10^{-4}
Surface water and ditches	10	10	10	10	10 *1
Colmation layer below ditches	10^{-5} (R.p.)	See case II.1 to II.3	10^{-6} (R.p.)	10^{-5} (R.p.)	10^{-6}
Colmation layer side of ditches	n.c.	See case II.1 to II.3	n.c.	n.c.	$5*10^{-5}$

n.c.: not considered, R.p.: River package, *1 additional ditches in forest

4.4.1.1 Steady state simulation of case I

Initially, a simple geology with hydraulic parameters summarized for case I in Table 4.2 was tested. The correlation coefficient of simulated versus observed heads (Fig. 4.10) was 0.64, the normalized RMS 36.89 %, and the mass balance discrepancy 0 %. The resulting simulated heads (Fig. 4.10 and 4.11) in the central peatland (MP7, MP6) were already close to the observed water levels due to the defined heads in the ditch system. Near the coast the simulated heads did not match the observed heads well (Fig. 4.10). The simulated heads differed among each measurement point, i.e. MP1 (1US and 1LS) < MP2 (2US, 2P and 2LS) < MP3 (3P and 3LS).

However, at individual measurement points (e.g. 1LS and 1DS) the observed vertical gradient was not matched by the simulation. The simulated heads at 1DS were 0.28 m lower than the observed heads (Fig. 4.10), which was the largest difference in the simulation.

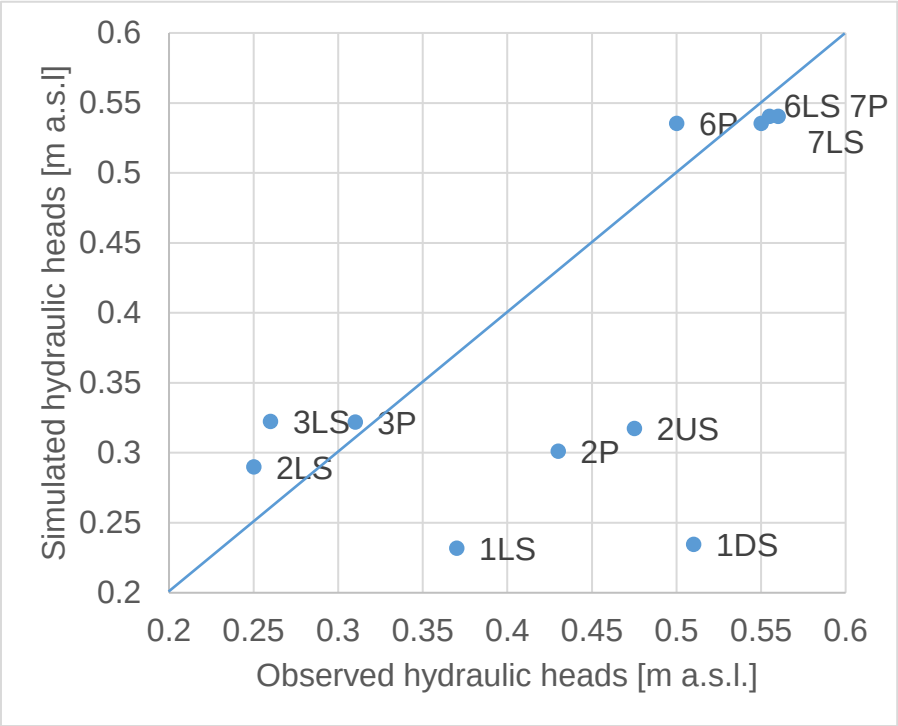

Figure 4.10: Simulated vs. observed heads of the initial steady state simulation.

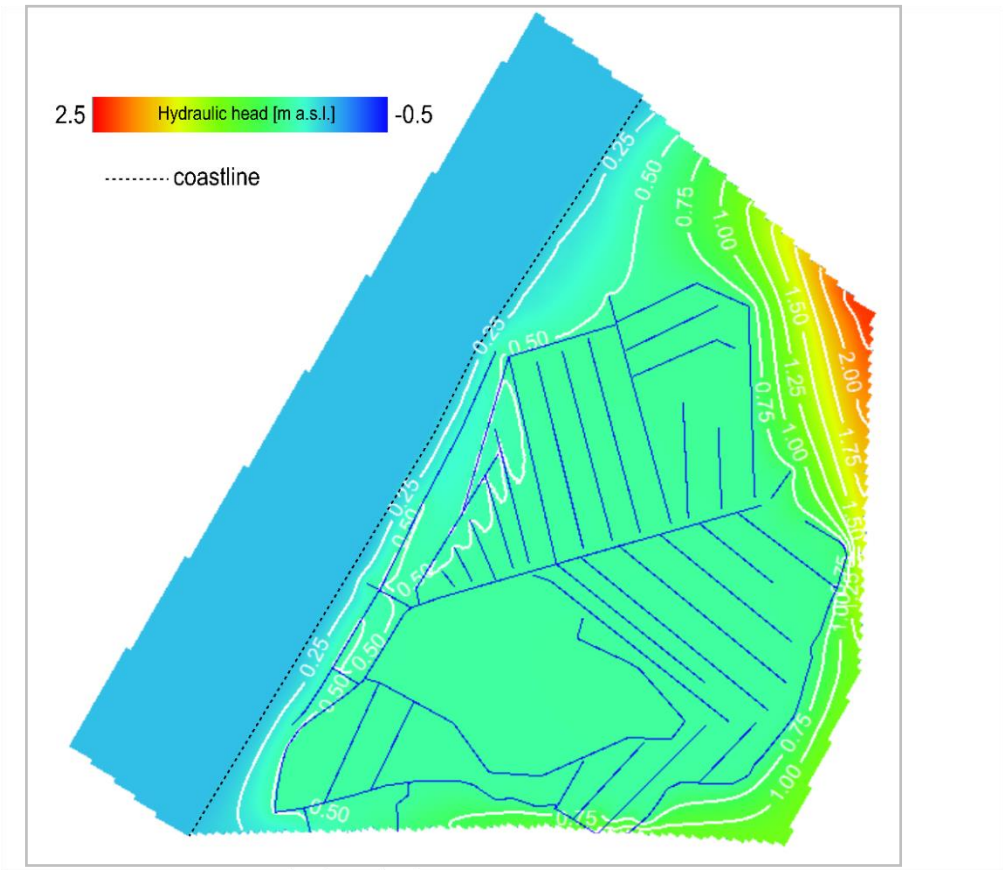

Figure 4.11: Simulated hydraulic heads in layer 20 (-0.25 to -0.5m).

4.4.1.2 Adjustments of the geological zones in case II

A vertical gradient can be achieved through implementation of impermeable layers. It has been already seen from slug test results, that the peat at the coast (3P and especially 2P) showed lower values of K due to the overlying dune sand, leading to a compaction of peat. For the peat below the dune dike (Fig. 4.12, pink colour) a K of $1*10^{-8}$ m/s was assigned. In general, the upper degraded peat might be disturbed by roots, while with greater depth the peat got more compacted. Hence, for peat below 2 m depth (Fig. 4.12, white colour) a K of $1*10^{-8}$ m/s was assigned as well. Locally, thin gyttja was found at the base of the peat (e.g. at MP2, B6 and B9 in Fig. 3.2) that decrease the connectivity between the aquifer and the peat. These zones were not discretized in the model, but conceptually were included in the K value of the peat below 2 m depth.

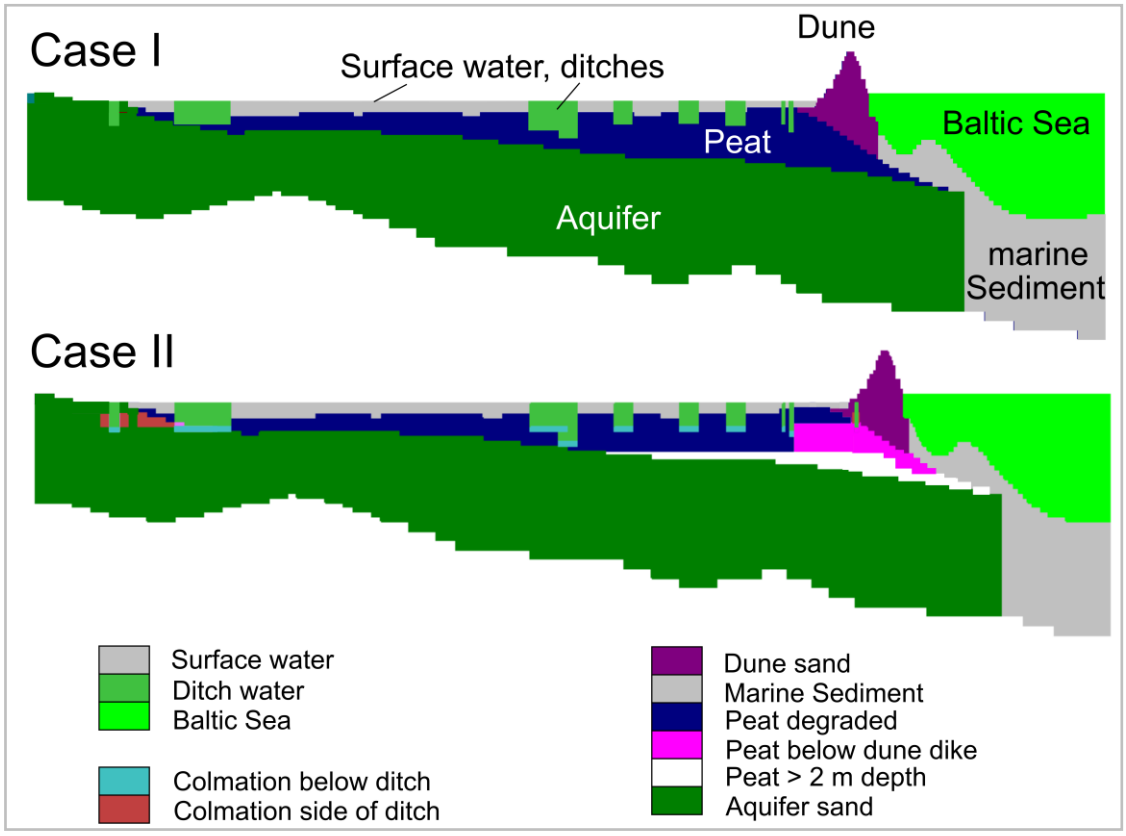

Figure 4.12: Zones of different hydraulic properties. For values see Table 4.2. Case I: Simple geology. Case II: Peat divided into different zones. Note that implemented colmation zones at the ditches as in case II.3 are already shown.

At MP 1 and the surrounding area, silty to clayey lacustrine sediments were identified with a thickness up to 3 m (Fig. 4.13). It is assumed that the lacustrine sediments extend below the lake. The sediment was also found in thin layers in the drilling cores B4 and 5 along the shoreline (Fig. 3.2), as well as 100 m offshore (Kreuzburg et al. 2018). Manual taken peat cores behind the dune dike helped to identify the extent parallel to the coast. The lake sediments were implemented into the model (see Fig. 4.14) in the same manner as described in Chapter 4.2.2. with a K of $5*10^{-8}$ m/s.

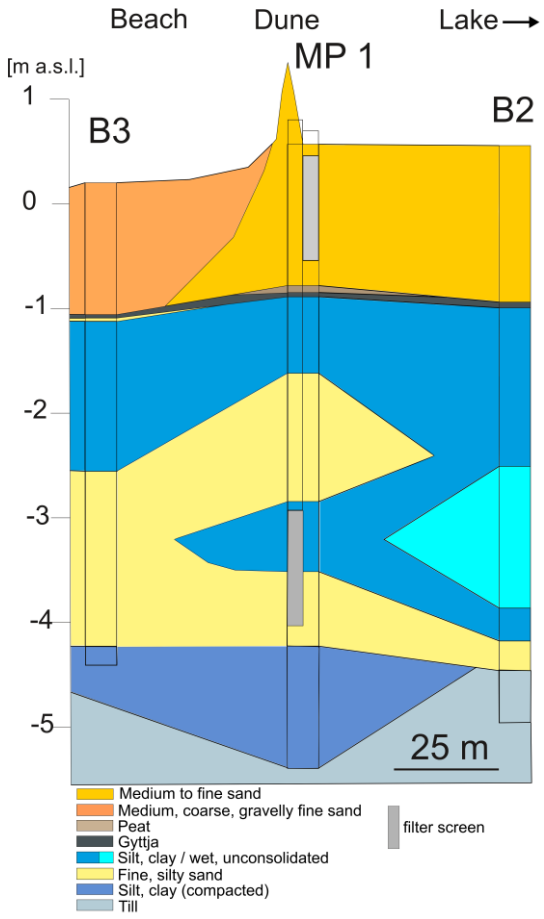

Figure 4.13: Geological profile at MP1 perpendicular to the Baltic Sea. For location of drilling cores see Fig. 4.14.

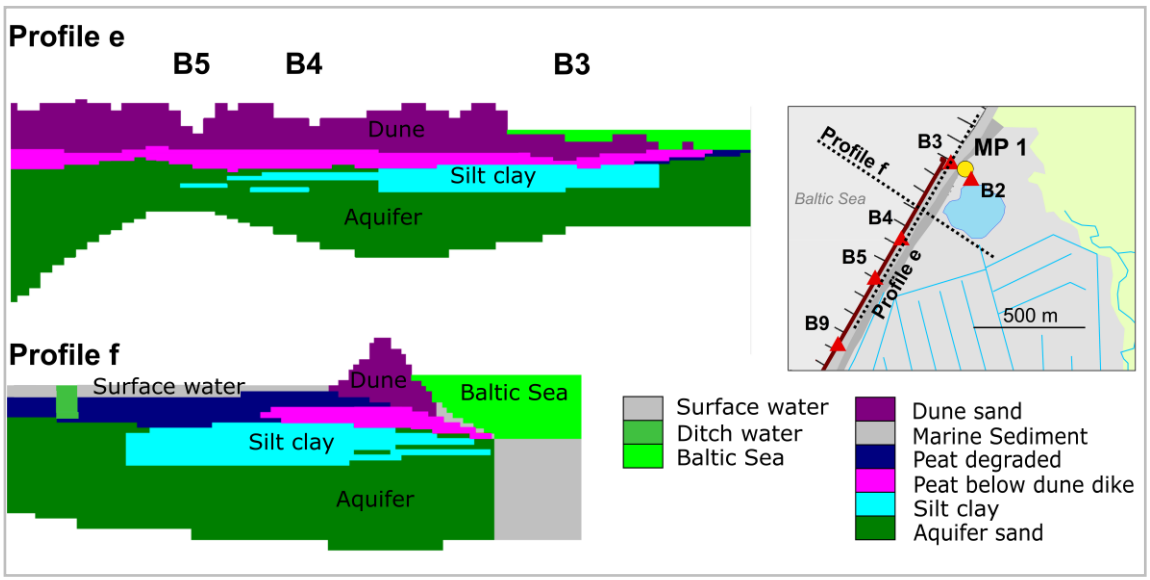

Figure 4.14: Implementation and extent of the silt-clay sediments in case II in the northern part of the peatland. For values of hydraulic conductivity see Table 4.2. Red triangles and yellow dot in the map show locations of drilling, dashed lines show profile locations e and f.

4.4.1.3 Implementation of ditches: Case II.1 to II.3

The ditches were first implemented as a River BC. Along profile A perpendicular to the coast (for location see Fig. 4.15) simulated heads are shown in Fig. 4.16 with a hydraulic conductivity of the riverbed of $1*10^{-6}$ m/s for case II.1 and $1*10^{-5}$ m/s for case II.2, while all other parameters stayed the same. In case II.1, the simulated hydraulic heads in the peatland were between 0.56 and 0.52 m. Hence, a larger gradient developed within the peatland. The sum of water taken out by the River BC, which equals surface water discharge, was 36 L/s. In case II.2 the hydraulic gradient was very small from the border at the forest towards the coast and balanced over large parts of the ditch system. The water level lowered to 0.51 m and the surface water discharge increased to 67 L/s. For the years 2011 to 2015 the average surface water discharge calculated by Miegel et al. (2016) was 24.4 L/s. The large density of ditches in the model domain led to a fixed distribution of hydraulic heads over the whole peatland depending on the conductance term (C_{Riv}) in combination with assumed hydraulic heads in the ditches.

The simulated hydraulic heads (case II.3 in Fig. 4.16) within the peatland were balanced as in case II.2, even though the heads were elevated and close to the measured water level of 0.535 at D_{ctr} in the central peatland. The surface water discharge decreased from 67 L/s to 11 L/s, which is closer to the average of 24.4 L/s by Miegel et al. (2016). However, the average discharge by Miegel et al. (2016) was based on a longer period, including the very wet year 2011.

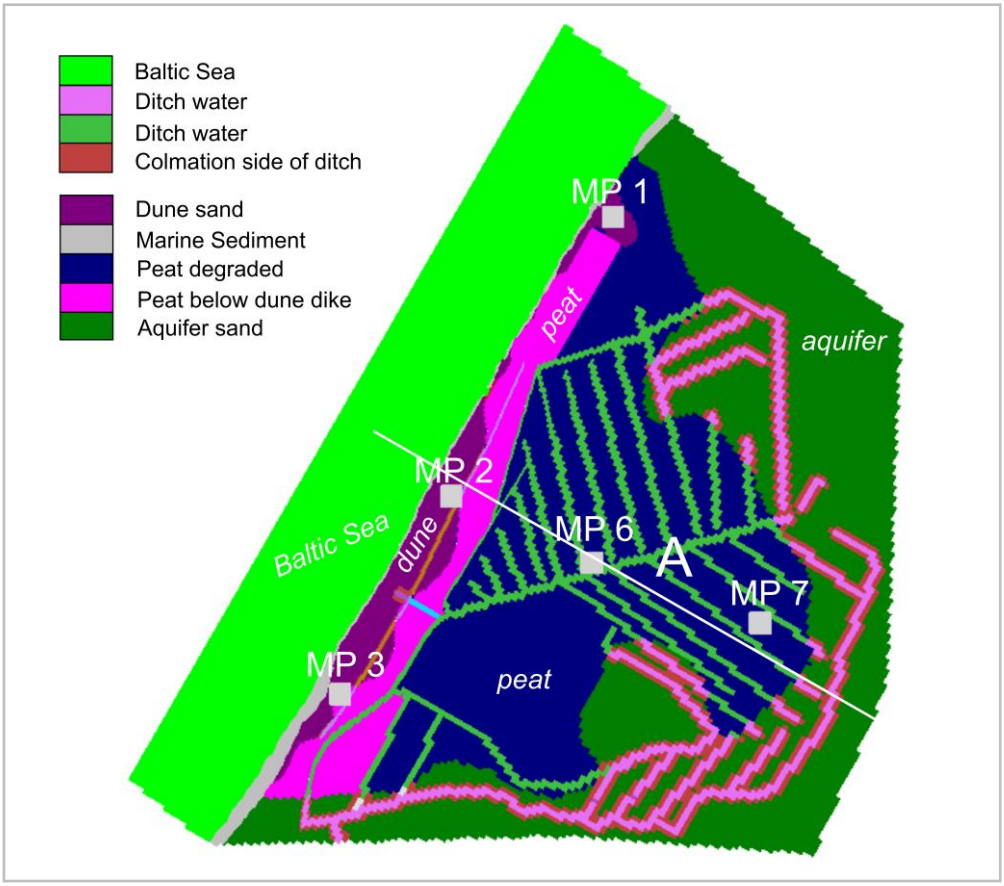

Figure 4.15: Hydraulic property zones (for values see Table 4.2) of model layer 20 (-0.25 to -0.5 m a.s.l.). Ditches are indicated in mainly green and pink (more colours (zones) are used near the dune dike to be able to switch cells easily back to its surrounding substrate (i.e. dune, peat or aquifer) in case of scenario simulations). The ditches located in the sand are surrounded by additional cells that can control the water flow between sand and ditch.

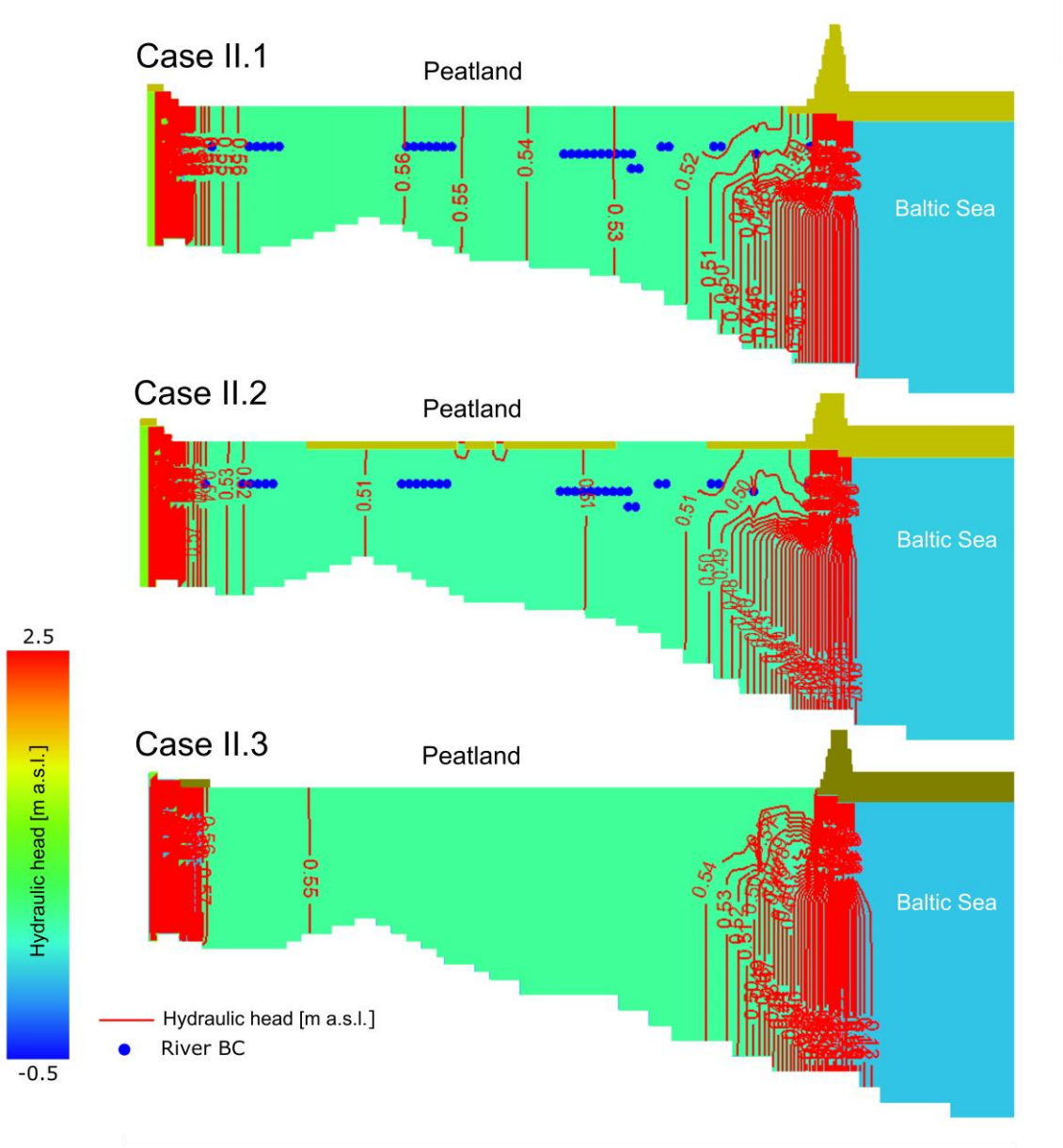

Figure 4.16: Simulated hydraulic heads along profile A (Fig. 4.15) with focus on the peatland with water levels balanced by ditches. Case II.1 and case II.2: River package with a riverbed conductivity of $1*10^{-6}$ m/s and $1*10^{-5}$ m/s, respectively. Case II.3: without River package and a CHD BC at the catchment outlet. For geological zonation see Fig. 4.12, for values of hydraulic conductivity see Table 4.2. Brown areas indicate dry cells. Length of the profile 2300m, vertically 40 times exaggerated.

4.4.1.4 Final calibration results of case II.3

The overall model performance of case II.3 with refinements in geological zonation (Table 4.2) resulted in a correlation coefficient of 0.89, a normalized RMS of 16.55 %, and a mass balance discrepancy of 0 %. The low-permeable zones both in form of peat and silt-clay sediments led to an increased vertical gradient at individual measurement points MP1, MP2 and MP3 (Fig. 4.17). The hydraulic head distribution with a balanced water level in the peatland is seen in Fig. 4.18. In general, the heads are slightly too high in the aquifer near the coast (Fig. 4.17: 1LS, 2LS, 3LS). 3P also seems to be influenced by the same factors. However, it is assumed that the observed heads at 3P rather follow the behaviour of the aquifer because the filter screen sits directly at the border between peat and aquifer. At 1DS the simulated head was raised enormously through implementing the silt-clay zone. The simulated heads at 2P and 2DS were still lower than the observed heads. The heads in the dune and peat at MP 2 are strongly influenced by recharge. At 1DS the sand is often saturated, while at 2DS unsaturated conditions are not considered in the simulation.

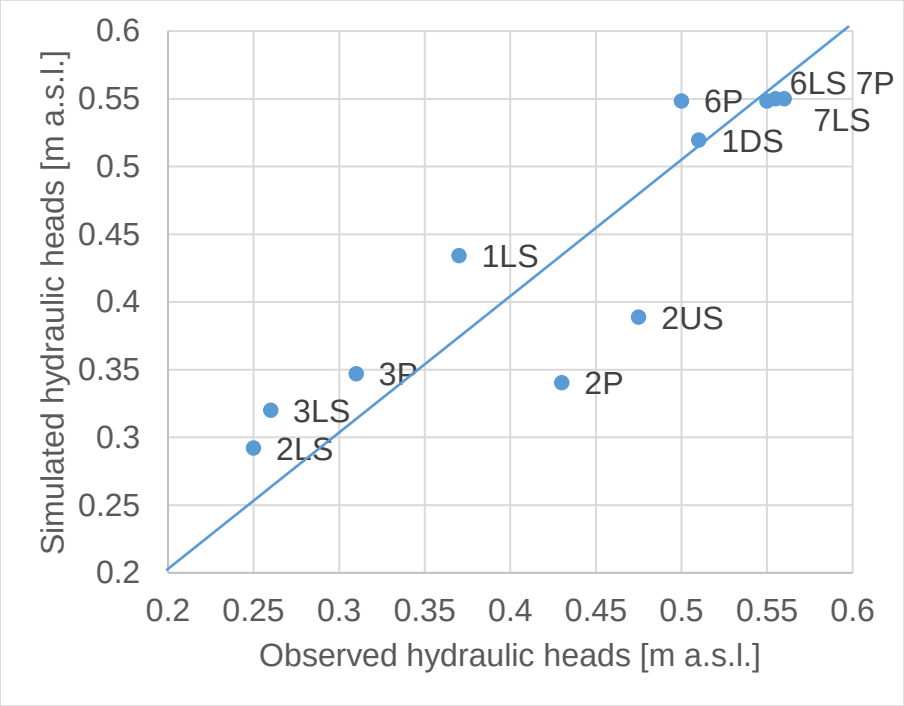

Figure 4.17: Calculated vs. observed heads for the calibrated steady state simulation case II.3.

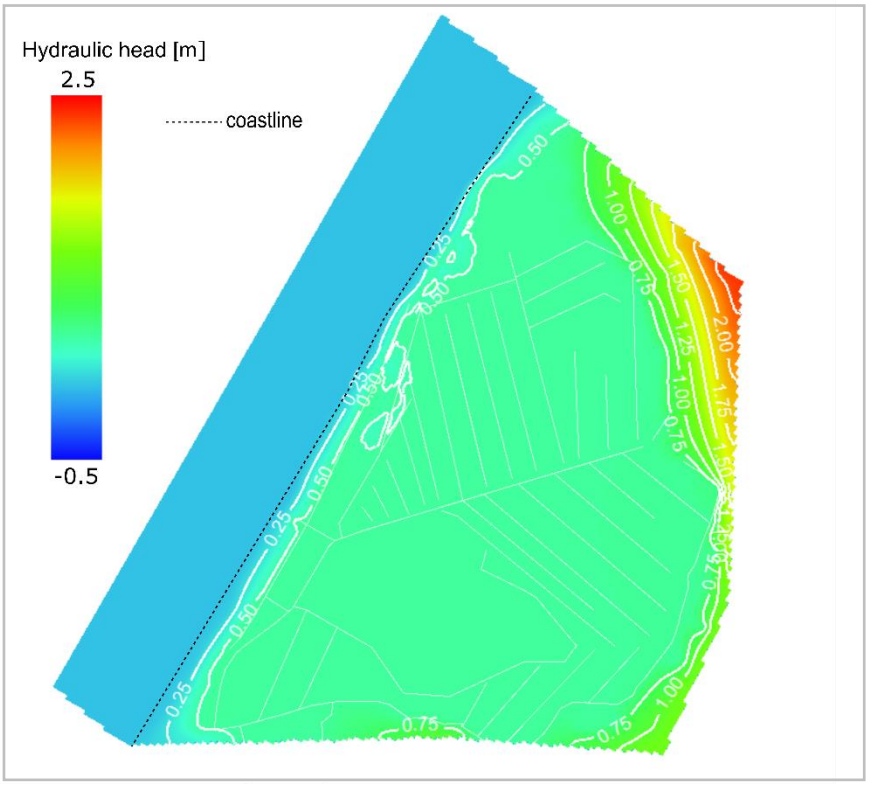

Figure 4.18: Simulated hydraulic heads [m a.s.l] in layer 20 (-0.25 to -0.5 m) of the calibrated steady state simulation case II.3.

4.4.2 Transient calibration

For the transient simulation S_y and S_s were assigned for each geological zone based on assumptions described in Chapter 4.2.3. Also values for n_e (later used with MODPATH) are shown. In case of the hydraulic conductivity it was further distinguished between horizontal $K_{x,y}$ and vertical K_z. The values are summarized in Table 4.3. The hydraulic conductivity parametrization of the peat was further adjusted in the transient simulation. For the peat below 2 m depth $K_{x,y}$ and K_z were changed to $1*10^{-9}$ m/s. The degraded upper peat was sub classified in a $K_{x,y}$ of $1*10^{-6}$ m/s and K_z of $1*10^{-7}$ m/s. This fitted the observed heads at MP6 and 7 better. Also $K_{x,y}$ of the silt-clay zone increased to $1*10^{-7}$ m/s, while K_z stayed $5*10^{-8}$ m/s. The normalized RMS of the simulation was 9.56 % and the correlation coefficient 0.96.

Table 4.3: Hydraulic parameters of the transient simulation.

Substrate	$K_{x,y}$ [m/s]	K_z [m/s]	S_s [m^{-1}]	S_y [-]	n_e [-]
Peat degraded	10^{-6}	10^{-7}	0.01	0.2	0.2
Peat > 2 m depth	10^{-9}	10^{-9}	$5*10^{-5}$	0.06	0.06
Peat below dune dike	10^{-8}	10^{-8}	0.0005	0.07	0.07
Aquifer (fS,Si)	$2*10^{-5}$	$2*10^{-5}$	0.0001	0.12	0.12
Silt clay	10^{-7}	$5*10^{-8}$	0.001	0.07	0.07
Dune (mS, fs)	10^{-4}	10^{-4}	0.0001	0.22	0.22
Marine sediment (mS, cS, fS, gravel)	10^{-4}	10^{-4}	0.0001	0.15	0.15
Colmation layer below ditches	10^{-6}	10^{-6}	0.001	0.01	0.01
Colmation layer side of ditches	$5*10^{-5}$	$5*10^{-5}$	0.001	0.01	0.01
Surface water (ditches, Baltic Sea)	10	10	10^{-6}	1	1

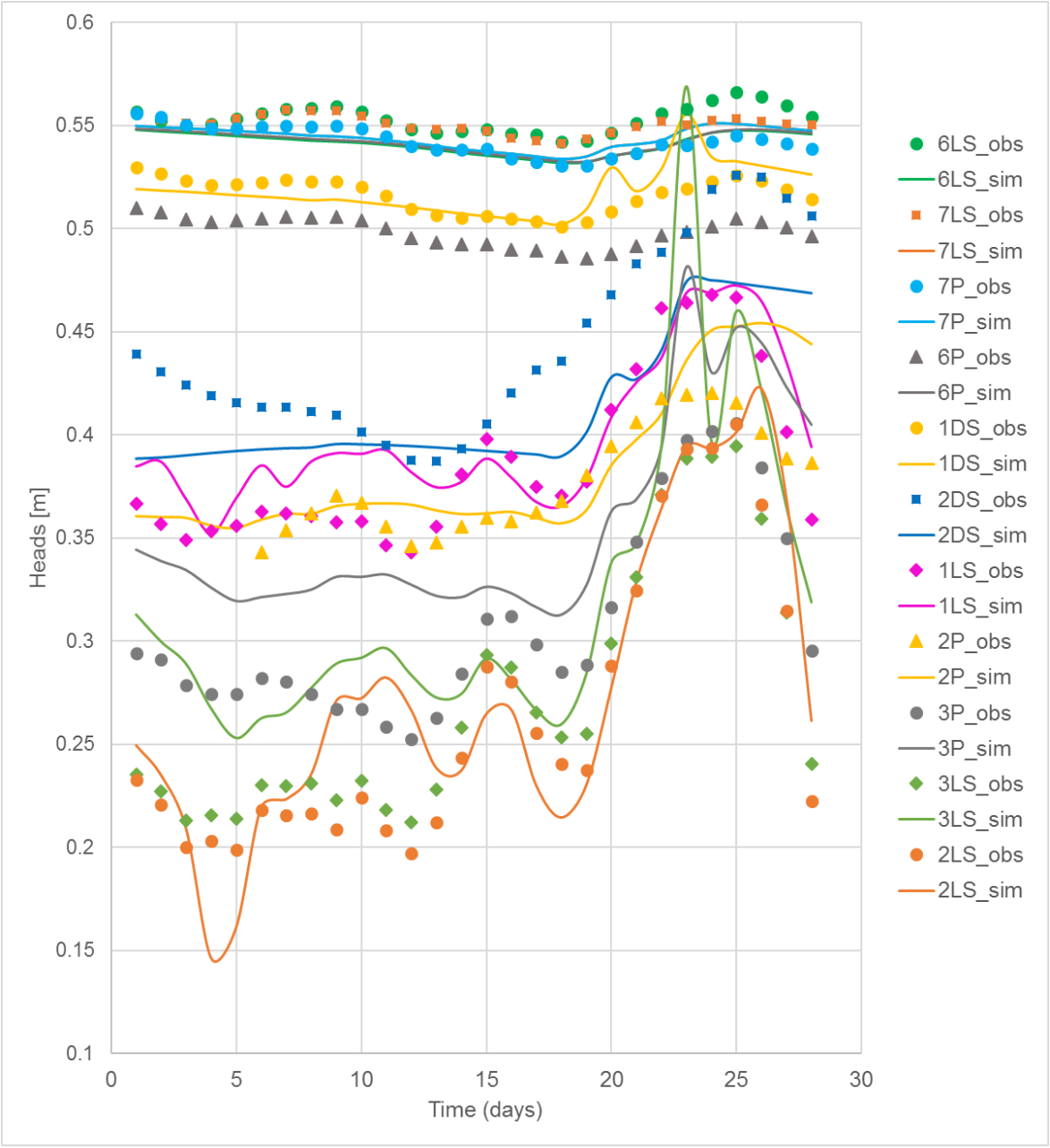

Figure 4.19: Simulated (solid lines) versus observed heads (points)[m a.s.l.] for the transient model.

The overall distribution of simulated heads in Fig. 4.19 fitted the observed heads very consistently. The general gradient between the measurement points was clearly seen in the simulation. Also, the varying amplitude of fluctuating water levels in the investigated area was in general observed in the simulation.

The simulation of differences in hydraulic heads in the central peatland (MP6 and MP7) is difficult because of the small differences in measured heads and the large

width of the ditches in the model. An increase of the simulated head at 7P above the simulated head at 7LS (and 6P and 6LS) from day 19 on due to precipitation (Fig. 4.6) is seen, although this is not seen in the measured heads. In general, a measurement error of a few centimetres is possible.

The simulated heads at 6P were in the same range as the simulated heads at 6LS, 7P, 7LS, but systematically were above the observed heads of 6P by about 4 to 5 cm. The levelled height of the observation well was verified several times. Whether local hydraulic heterogeneities in the vicinity to the main ditch could be the reason cannot be clarified here.

The simulated heads at 3P were above the observed heads throughout the simulation period as well. The observed heads at 3P might not reflect hydraulic conditions solely in the peat, because the filter screen might intersect the aquifer below. The lower end of the screen of 3P sits directly at the border of the two layers due to the thin extent of the peat at this location. Permeability caused by roots of trees was not considered at that location (low K_z).

Taking the simulated heads of 3P and 6P out of the error estimation, the normalized RMS decreased to 8.55 % and the correlation coefficient increased to 0.97.

The simulated heads at 1LS, 2LS and 3LS fitted the observed heads well throughout most of the simulation period, but slightly deviated in a systematic pattern between day 8 and 13. This could be due to incorrectly assumed BC's (e.g. using a running-mean as CHD-BC and observation heads) for these stress periods.

The large deviation on day 23 at 3LS (also visible at 3P) due to strong precipitation could not be adjusted by testing parameters for the overlying peat.

The trend of simulated heads at 2P (heads deviated after day 23) depend mainly on K and S_s as well as on the heads in the overlying dune sand. The simulated heads at 2DS increased with a delay and were mostly lower than the observed heads. Changes in S_y led to negligible changes in the simulated heads. Unsaturated zone processes, that were not considered, could be the reason. Numerically, a slow

rewetting of the dry cells due to a fine discretization could lead to lower heads. However, an increase of the time steps for one stress period from 10 to 100 resulted in no differences of simulated heads.

4.5 Validation

The validation was performed for another 30 days (21.4 to 20.5. 2017) and matched the observed heads well (Fig. 4.20). The normalized RMS was 10.38 % and the correlation coefficient 0.94. Without 3P and 6P they were 8.53 % and 0.96, respectively. The validation confirmed that some factors (e.g. unsaturated zone) were not considered to match the heads for 2DS and 2P. The lowering of observed heads after day 46 in the coastal aquifer at 1LS and 3LS was not reproduced by the simulation. Also, simulated heads at 3LS fluctuated stronger. However, at 2LS the lowering of heads towards the end of the simulation was observed.

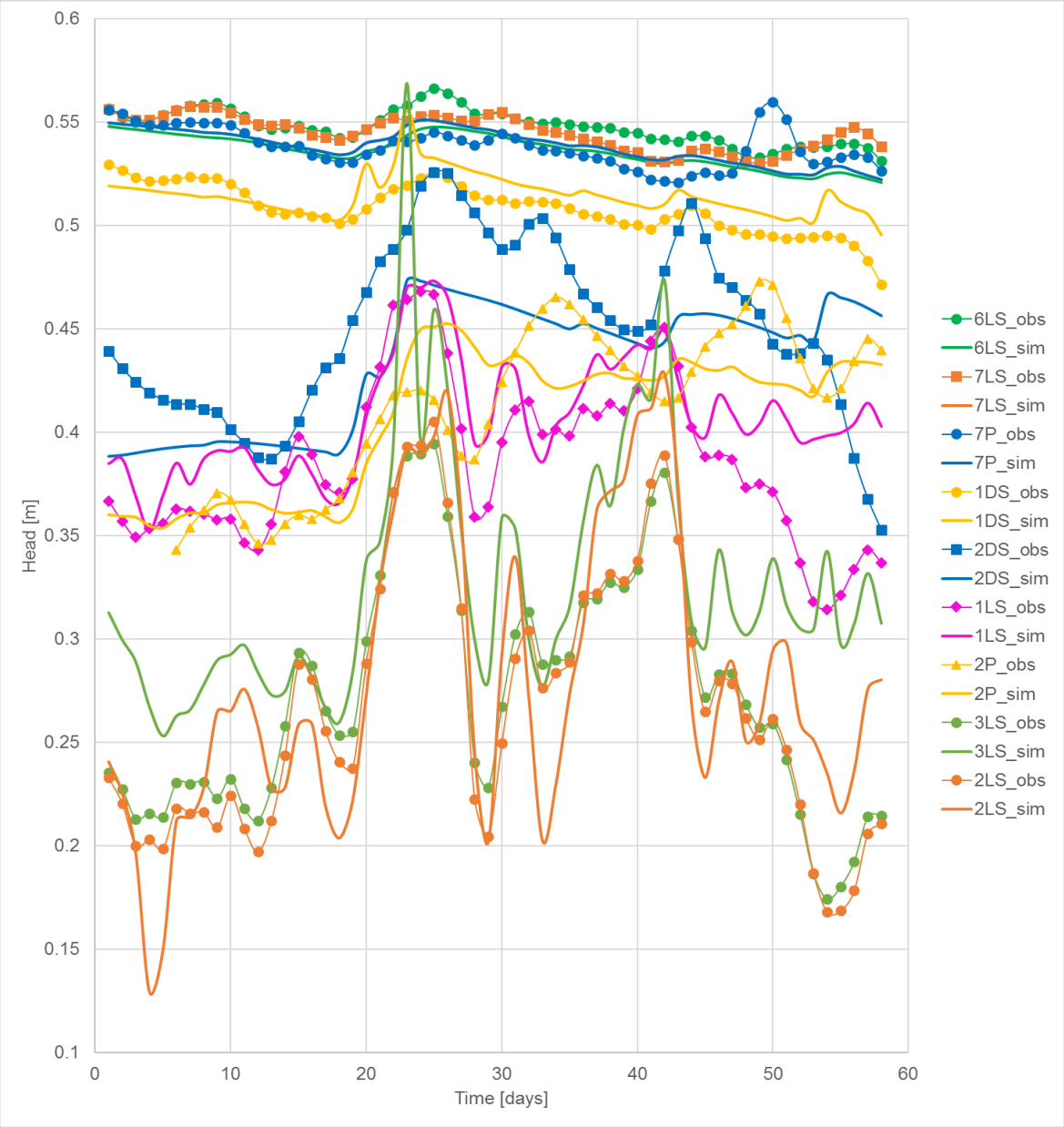

Figure 4.20: Simulated (solid thick line) and observed (points with thin line) heads [m a.s.l.] between 24.3.17 to 20.5.17. 3P and 6P are not shown.

4.6 Sensitivity analysis of the ET rate and specific storage

4.6.1 Methodology

Sensitivity analysis of ET and S_s were performed because ET was assigned as potential ET solely based on climate data, and S_s was solely assigned based on literature.

ET is an important parameter because it is part of the water balance and affects surface water discharge from the peatland and SGD from the dune dike. As an example, the sensitivity towards changes in the ET rate of the peat and the dune area was tested, though the ET rate of the forest likely affects surface water discharge and groundwater supply to the peatland as well. The extinction depth of the ET rate, EXDP, was varied between 0.1 and 0.6 m. Numerically, ET is applied to the saturated surface. In case of the dune an unsaturated zone of a few centimetres to meters lies between the saturated zone and the atmosphere. Here, the effect of an EXDP of 0.1 and 0.5 m was tested. In case of the peat with ponding surface water, the ET is not only effective at the water surface, but also in the saturated peat due to plant activities. Here, an EXDP of 0.1 and 0.6 were tested. Different combinations of EXDP for peat and dune were tested in four cases A-D (Table 4.4). The overall performance in terms of changes in the mass balance of the model was tested, but also single reactions at the different observation wells in terms of changes in RMS at each well.

Table 4.4: Assigned extinction depth EXDP [m] of the ET rate for cases A-D.

Area	**Case A**	**Case B**	**Case C** calibrated model	**Case D**
Peatland	0.1	0.1	0.6	0.6
Dune dike	0.1	0.5	0.1	0.5

S_s, the specific storage, is an important parameter under confined conditions like in the coastal aquifer. It defines how the water storage due to compressibility, and to which extent the hydraulic head changes, if shifts of the water level occur (e.g. due to sea level fluctuations). For both the marine sediments and the aquifer the specific storage was lowered from $1*10^{-4}$ m^{-1} to $1*10^{-5}$ m^{-1}. For the deep peat below 2 m depth S_S was lowered from $5*10^{-5}$ m^{-1} to $1*10^{-5}$ m^{-1}, for the silt-lay sediments and degraded peat S_s was lowered to $1*10^{-4}$ m^{-1} (see Table 4.5 and for comparison see Table 4.3).

Table 4.5: Specific storage S_s in m^{-1} of the sensitivity analysis (test). For the second sensitivity analysis (test2) only S_s of the marine sediment and aquifer was changed.

Hydraulic property zone	S_s (test)	S_s (test2)
Aquifer and marine sediments	$1*10^{-5}$	$5*10^{-4}$
Peat > 2m depth	$1*10^{-5}$	$1*10^{-5}$
Peat degraded, silt clay	$1*10^{-4}$	$1*10^{-4}$

4.6.2 ET rate

The overall changes in the mass balance (Fig. 4.21) towards changes of the ET rate in the dune area (8.5 % of the modelled land area) was low (comparison case A to B and C to D in Fig. 4.21). Changes of the ET rate in the peatland (70 % of the modelled land area) led to strong changes (comparison case A, B to C, D in Fig. 4.21). The effect of changes in the ET rate – mainly for case C and D – led in general to a lowering of the RMS of calculated heads at the coast (MP 1, 2 and 3 in Fig. 22).

1DS and 2DS should be directly influenced by changes in the ET rate for the dune area, while the heads in the aquifer change because of a lowered hydraulic gradient. At 1DS a decrease of the RMS due to enhanced ET (case A to B) from the dune was seen (Fig. 4.22). At 2DS however, a slight increase was seen, while for case C and D the RMS increased even further. The simulated hydraulic heads at 2DS (Fig. 4.19) were in general lower than the observed heads. Only saturated conditions were

considered in the simulation, that might be realistic at 1DS, where the unsaturated zone was maximum 0.02 m thick for the simulated period. However, at 2DS, the unsaturated zone was in reality 0.3 to 0.4 m thick for the simulated period (at MP 3 approx. 0.5 m), which should decrease the effect of ET. Due to the way the ET was assigned in the model the loss of water was too high for the in large parts unsaturated dune dike. A refinement of the assigned zones for ET along the dune dike could further improve the simulated heads at the dune.

An increase of EXPD for the peat area (case C and D) resulted in an increase of ET by a factor of 33. This led to a lowering of the surface water discharge (Q_{SW}) by a factor of 1.4 (Fig. 4.21). The additional water needed for enhanced ET came from storage release ("Storage in" Fig. 4.21), while the inflow to the model ("CHD in" Fig. 4.21) changed only slightly. The storage release came mainly from the part defined as surface water (including ditches) with a S_y of 1 (not shown). The RMS (Fig. 4.22) decreased for 7P, while it increased slightly for 7LS and more pronounced for 6LS (simulated heads lower than observed heads) located near the main ditch. This could indicate an increased influence of surface water processes (ET or drainage) on the underlying aquifer depending on the way how ditches are implemented. However, the overall RMS at 6 LS and 7 LS was low compared to the RMS at observation points near the coast (Fig. 4.22). The total RMS decreased for case C and D.

Hence, simulated surface water discharge is very sensitive, and the underlying aquifer – depending on the connectivity to the ditch system – is slightly sensitive to changes in ET. Furthermore, unsaturated zone processes might play a major role at the dune dike. Water hold back in the unsaturated zone of the dune due to surface water tension might add to the saturated zone in case of a precipitation event and subsequent recharge. If a drought as in summer 2018 is simulated, the effects of how the ET rate is assigned will become more pronounced for the unsaturated peat area as well. The potential ET will not be reached any more and either more parameters have to be considered for the calculation of the actual ET, or alternatively EXDP has to be varied temporally.

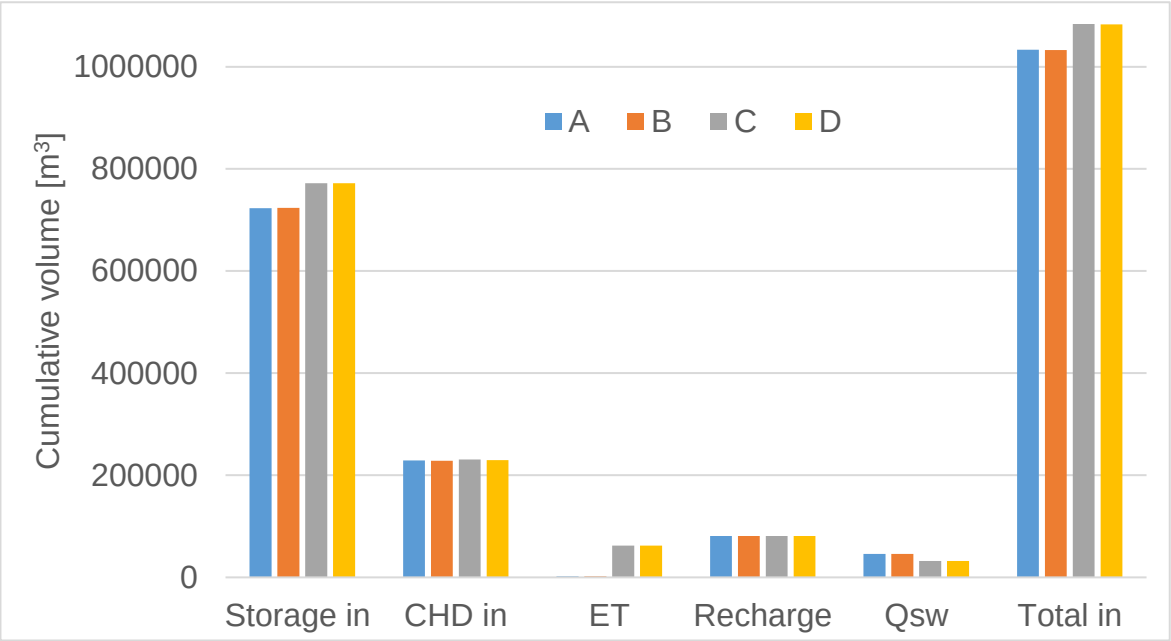

Figure 4.21: Mass balances for the models A to D. The mass balance refers to the complete model domain and is the cumulative volume of 28 stress periods. ET for case A and B is low.

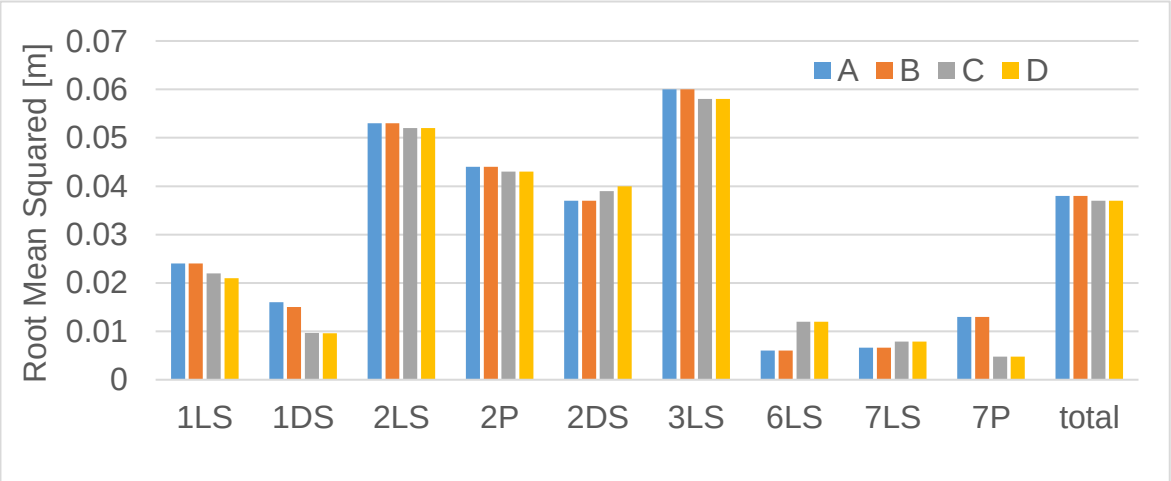

Figure 4.22: Root mean squared error at the different observation wells for the models A-D.

4.6.3 Specific storage

Fig. 4.23 shows the heads at observation wells in which a difference to the calibrated transient simulation occurred.

Differences between simulated heads in the peatland (not shown) were very low because they might be more influenced by S_y or the ditch system. Differences were slightly visible at 6LS (Fig. 4.23), where the aquifer was more confined due to a thicker peat layer. The heads increased less than a centimetre due to precipitation events. However, the discrepancy to the observed heads is larger.

A decrease of S_s in the deep peat and aquifer led to lower heads at 2DS (day 20 onwards), even though 2DS is unconfined, and at 2P as well (day 23 onwards). Hence, the hydraulic head in the dune is sensitive to the storage properties of the peat and aquifer below, but unsaturated zone processes in the dune might have a greater influence.

In the aquifer the lowering of S_s led to stronger amplitudes of the simulated heads, especially at 2LS, but also at 1LS (Fig. 4.23). Additionally, the increase or decrease in heads, e.g. due to changes in sea level, shifted to earlier times. For the second sensitivity analysis (test2) with a large S_s, a decrease of the amplitudes and a delay of peaks occurred (shown for 2LS in Fig. 4.23). This effect was only slightly pronounced at 1LS (data not shown).

Hence, the model is mostly sensitive to changes of S_s in the confined aquifer at 2LS with a thick and rather impermeable peat layer above. S_s here defines whether SGD occurs immediately or with a delay, and with lower and more constant rates. The heads in the aquifer are less sensitive in the area dominated by the ditch system with partly confined conditions, e.g. at 6LS (small sensitivity), and rather unconfined conditions at 7LS due to a thin peat (no sensitivity).

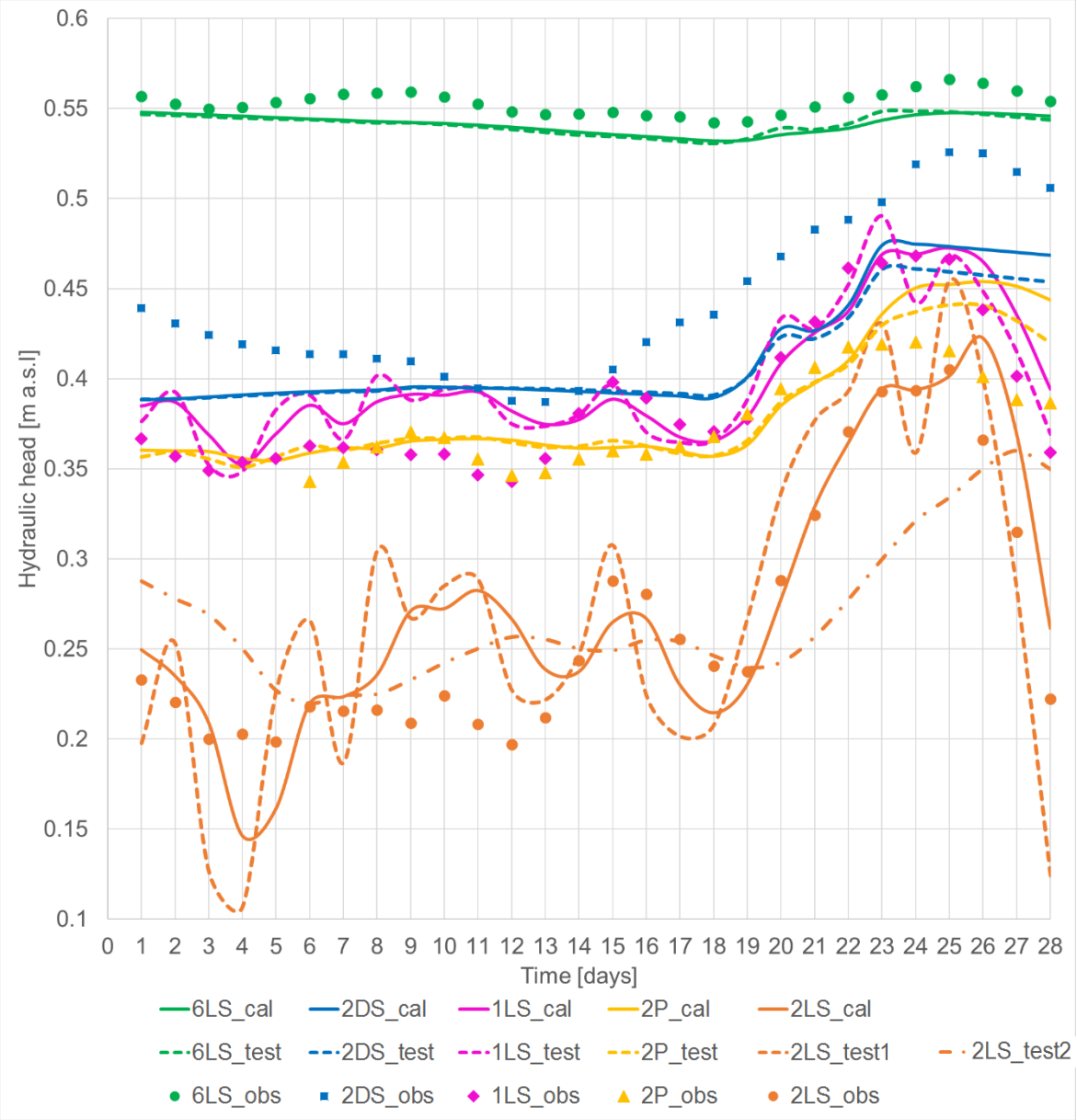

Figure 4.23: Simulated hydraulic heads for lower values for S_S (test, dashed line), for the calibrated model (cal, solid line), and observed heads (obs, points). Note that only observation wells are shown where differences between the tested and calibrated simulation occurred. See Table 4.3 (calibrated) and 4.5. (tested) for input parameters.

5 Modelling results and discussion

5.1 Water balance: variation of surface water discharge, SGD and SWI

The water balance of the transient simulation with daily stress periods illustrates the complex interaction of climate, drainage system, hydraulic properties and resulting hydraulic gradients with effects on the amount of surface water discharge (Q_{SW}), SGD and SWI. By calculating a coefficient of determination, the interaction of different parameters (Fig. 5.1) was determined to get an initial idea of direct driving forces on flow. There was no direct interaction of the ET and recharge rate with Q_{SW} or SGD, and also no interaction of SGD with Q_{SW}. A partial interaction (R^2 = 0.22) of the water level difference between the peatland (7LS) and the Baltic Sea with Q_{SW} was found. However, Q_{SW} did not vary to great extent (between 9 L/s and 17 L/s) and a longer simulation period might provide more information. Interestingly, the interaction of the water level difference between the peatland (7LS) and the Baltic Sea with SGD was higher (R^2 = 0.4) than for Q_{SW}. The interaction of the water level difference between 2LS and the sea level with SGD even increased to 0.58, which is due to the decreasing influence of drainage at the dune dike.

The amount of simulated Q_{SW} matched the calculated discharge curve by Miegel et al. (2016) with approx. 9 L/s for water levels between 0.51 to 0.53 m upstream of the ground sill. A deviation in the discharge can result from differences in the water level downstream of the ground sill.

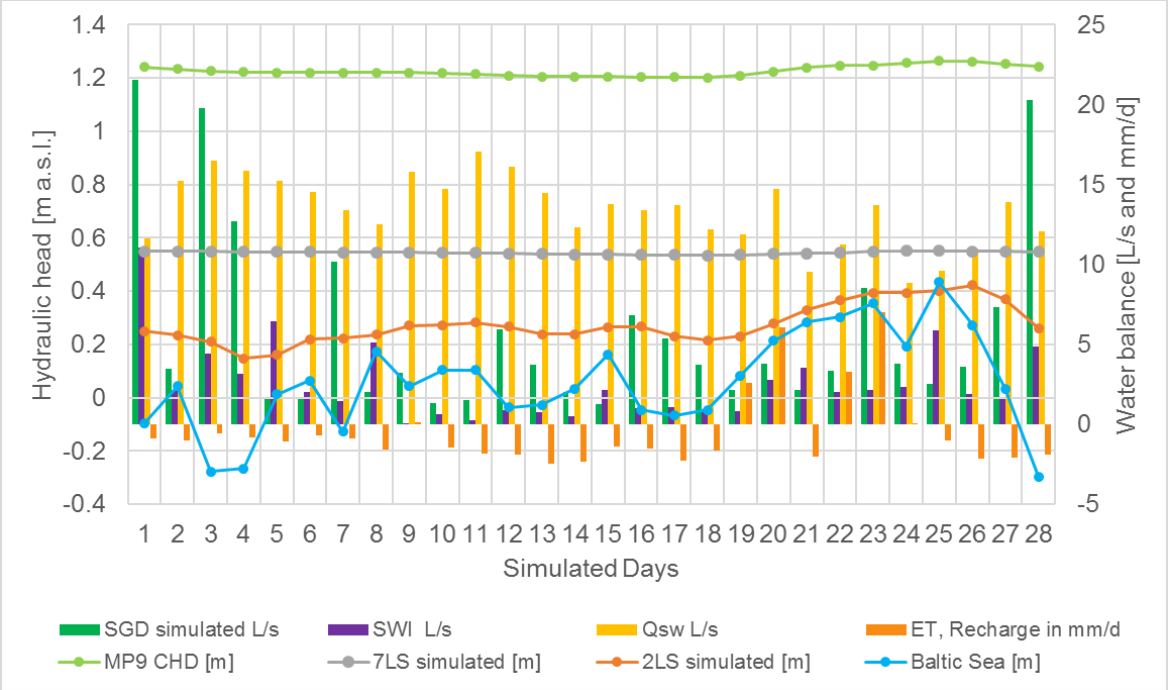

Figure 5.1: Water balance and hydraulic heads for the simulated period. Note that ET and recharge are in mm/d. CHD: constant-head (boundary condition).

5 of the 28 days from Fig. 5.1 were selected in Fig. 5.2, which will be looked at more closely in the following chapters.

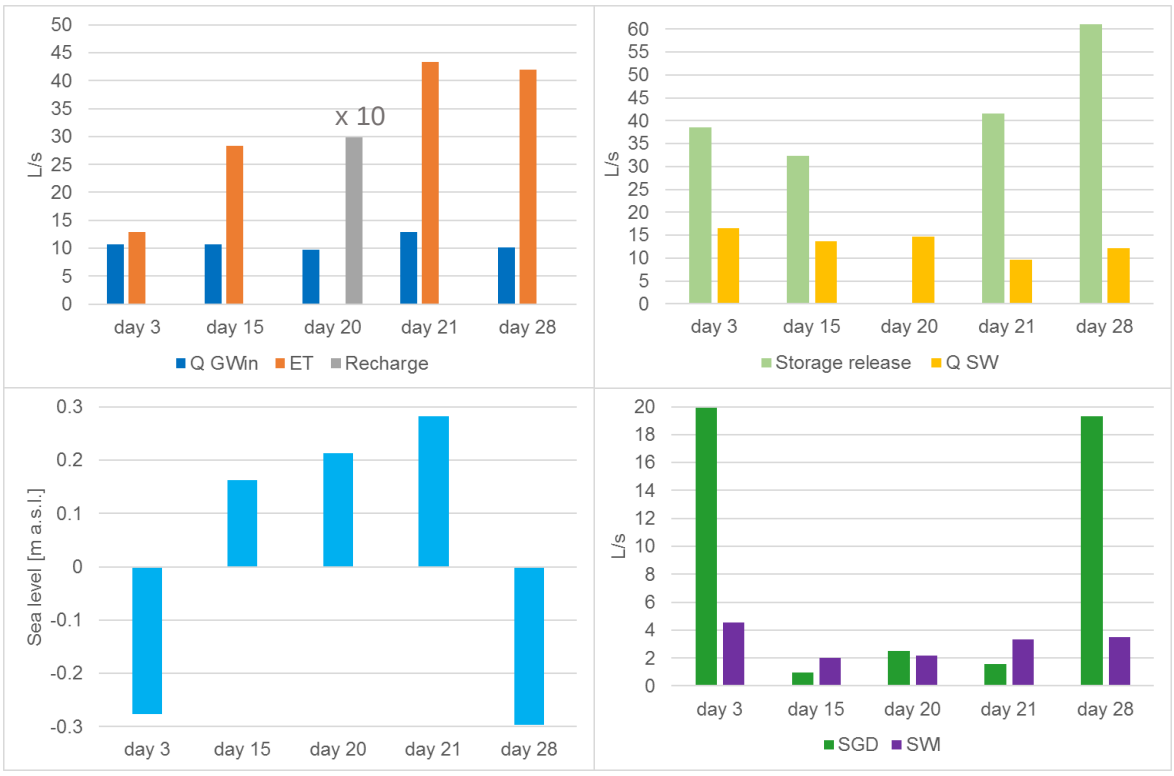

Figure 5.2: Water balance calculated with the Zonebudget package for the simulated days 3, 15, 20, 21 and 28. a) Q_{GWin} is the inflowing groundwater to the model domain based on CHD-BC; ET is the evapotranspiration. Note that recharge on day 20 is 10 times higher. b) The storage release refers mainly to changes in storage of surface water in the peatland. On day 20 290 L/s went into the storage (not shown). c) Baltic sea level assigned as CHD-BC. d) SGD is submarine groundwater discharge and SWI seawater intrusion.

5.2 Spatial and temporal distribution of SGD and SWI

5.2.1 Temporal distribution

A comparison (Fig. 5.3) of simulated total SGD and SWI to the calculated discharge within the aquifer and dune with Darcy's law (see Chapter 3.2.7) showed that the simulated SGD varied more than the calculated discharge from the dune and

aquifer. Further, simulated SGD was often much higher than the calculated discharge. This could indicate a large proportion of recirculating seawater at the sea-sediment interface. Simulated SWI, an indicator for recirculating seawater, exceeded SGD at 6 of 28 days (Fig. 5.3). However, the simulated period is rather characterized by increased groundwater discharge from the landside. The total SGD can be as high as river runoff or even higher (Moore 2010), whereas freshwater SGD is 0.01 % to 10 % of river runoff on a global scale (Jiao and Post 2019). Here, the total SGD was between 9 % and 185 % (average 45 %) of Q_{sw} for the simulated period of one month. If freshwater SGD was 10 % of Q_{sw}, then it should amount in 1 L/s to 1.7 L/s.

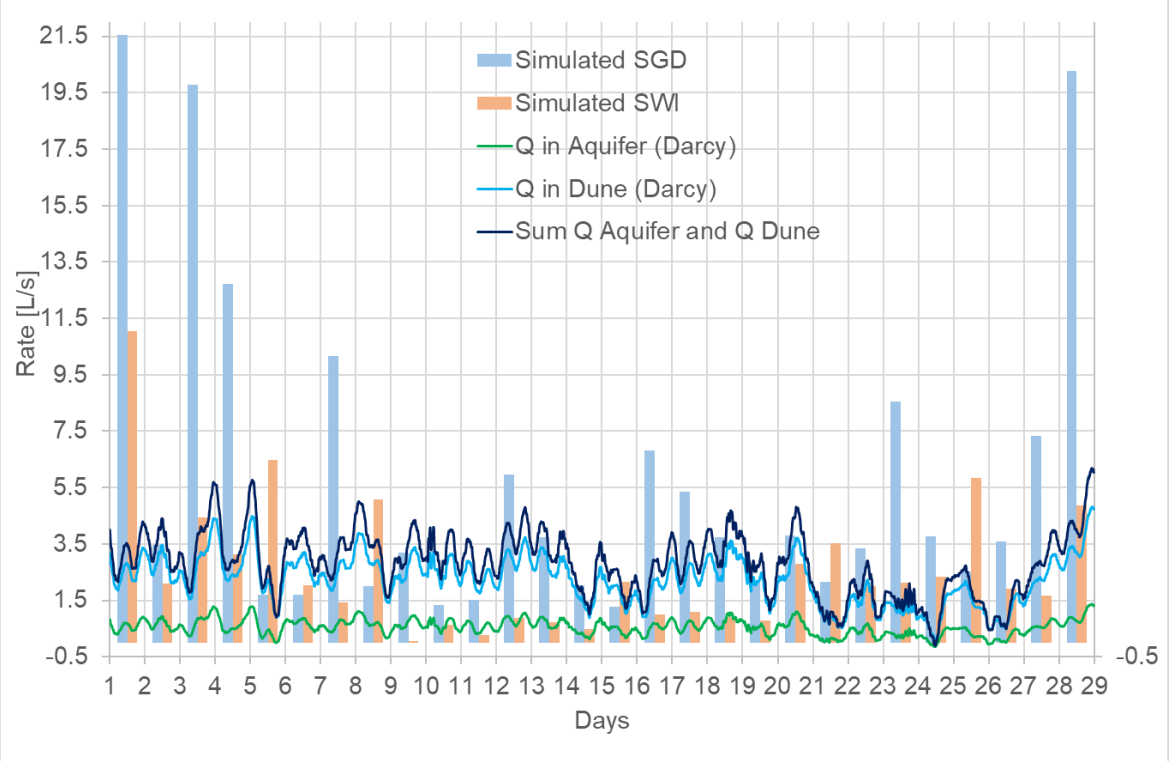

Figure 5.3: Simulated SGD and SWI (bars) and groundwater discharge within the aquifer and dune (lines) calculated with Darcy's law (see Chapter 3). Note that Q is not equal to fresh SGD (see Chapter 3.2.7).

5.2.2 Depth distribution

Fig. 5.4 shows exemplary for 5 selected days (compare to Fig. 5.3) the amount of SGD and SWI over the depth of the sea floor. Most of the SGD and SWI occurred at the shoreline within the first 0.75 m of the water column, and hence within approximately 20 m distance to the shoreline. During day 3 and 28 with a low sea level (~ -0.3 m) most of the SGD occurred between -0.5 and -0.75 m depth with ~10.5 L/s and partly between -0.25 and -0.5 m with ~ 3L/s. Hence, SGD occurred directly below the sea level. In depths below -1 m, SGD still occurred with rates less than 0.6 L/s. During days 15, 20 and 21 with a higher sea level and low SGD rates, most of the SGD (~1.2 L/s) occurred between 0 and -0.25 m depth. However, also on day 3 (high SGD) a similar rate of SGD occurred at the same depth. Interestingly SWI occurred in opposite depths to SGD depending on the sea level: if most of the SGD occurred in greater depth during low sea levels (day 3, 28) SWI occurred above the SGD (0 to -0.25 m depth). This could be due to infiltrating sea water from the previous stress period with higher sea levels (Fig. 5.3). If SGD only occurred in shallow depth during high sea levels (day 15, 20, 21), SWI occurred mainly below the SGD between -0.25 to -0.75 m depth.

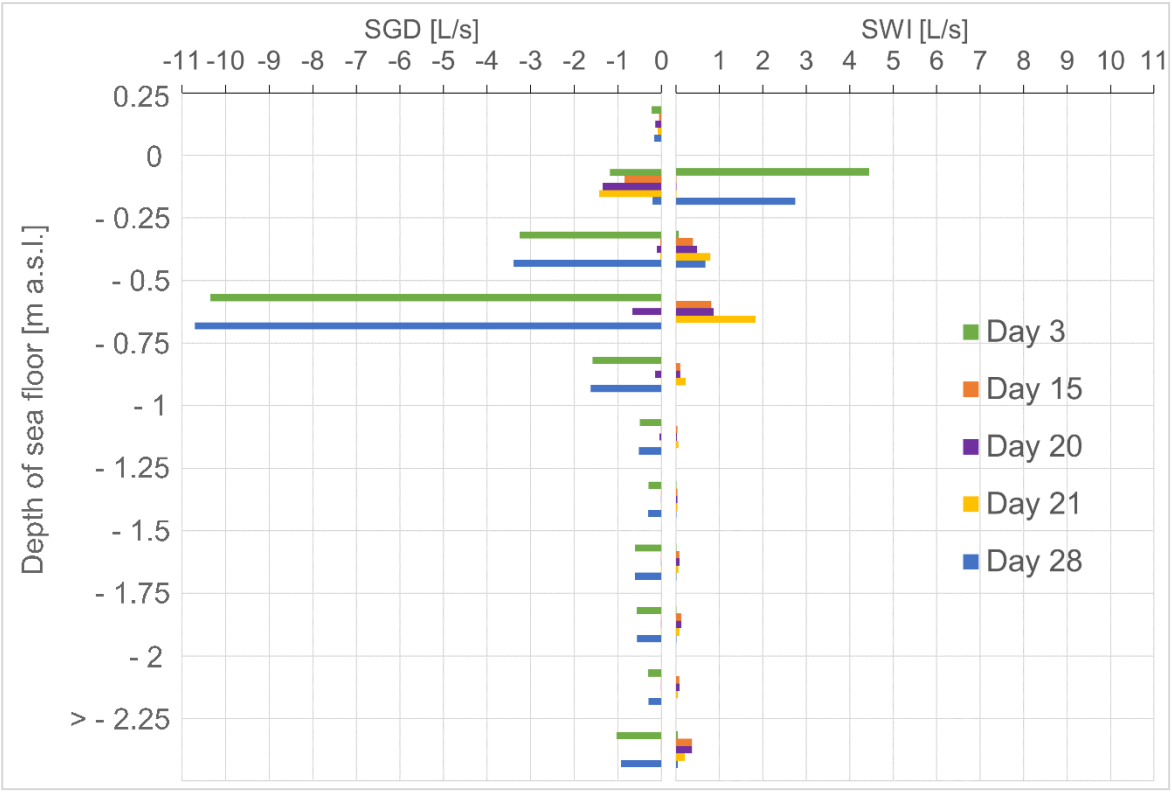

Figure 5.4: SGD and SWI calculated with the Zonebudget package over the depth of the sea floor.

The depth distribution in Fig. 5.4 gives only a rough idea of the locations influenced by SGD and SWI. Variable density effects on flow were not considered in the simulation. They could change the amount of SGD and SWI, as well as flow paths. At the study site the highest freshwater discharge and maximum density differences (0.01 g/m^3) occur both at the dune-beach interface. This indicates that convective mixing and dispersion of freshwater and recirculating seawater (e.g. Smith 2004) might be an important mechanism. Because tides are negligible, the typical formation of an upper saline plume and a "freshwater discharge tube" below (resulting in freshwater SGD seawards of that plume during low tide (e.g. (Robinson et al. 2007b)) is not expected here. Greskowiak (2014) illustrated in numerical experiments that a low transmissivity, a low beach slope (0.02) and a high tidal amplitude (1 to 1.5 m) promoted salt-fingering flow (a destabilization of the upper saline plume) in the beach sediments and led to heterogeneous freshwater

discharge locations in time and space. Here, the beach slope is rather high (~0.05) and the tidal amplitude very low with a maximum of 0.2 m. The depth and extent of the peat surface at the coastal interface also affect fresh SGD from the dune as it limits a downward flow and defines the cross-sectional area of the overlying sand for discharge. A shallow depth (1.5 to 10 m) of the unconfined aquifer was found to limit salt-fingering flow (Li et al. 2008). Hence, a saltwater-fingering is not expected. However, the density-difference usually assumed when simulating variable density flow experiments at the coastal interface is 0.025 g/m^3 (e.g. Robinson et al. 2007a, 2007b Röper et al. 2015). The effect of a lower density difference might lead to less convective mixing because the buoyancy force decreases.

Further, unsaturated zone processes were not considered and numerical issues like the sometimes observed non-rewetting of dry cells during high sea level along the shoreline might influence the simulated amount and distribution of SGD and SWI (Mulligan et al. 2011).

Changes in the hydraulic gradient due to seasonal variations (sea level driven by storm intensity, recharge, drought) or artificial changes (drainage, rewetting) could lead to a land- or seaward movement of recirculating seawater and freshwater SGD along the beach interface.

In greater depth the simulated SGD accounts for recirculating seawater or advective pore water exchange that is driven by sea level fluctuations. Some proportion however is assumed to originate from the confined aquifer.

5.2.3 Influence of geology on flow paths at the coastal interface

The confining geological zones (peat and silt-clay sediments) will influence the distribution of land-derived SGD. These zones occur in depth between -0.5 and -3 m. Fig. 5.5 (Day 3 and Day 21) shows profile B along the beach (compare to Fig. 3.2) and it can be seen that the outcropping peat and silt-clay sediments influence the

hydraulic head distribution. Vertical gradients also exist where these layers intersect the marine sediment and aquifer.

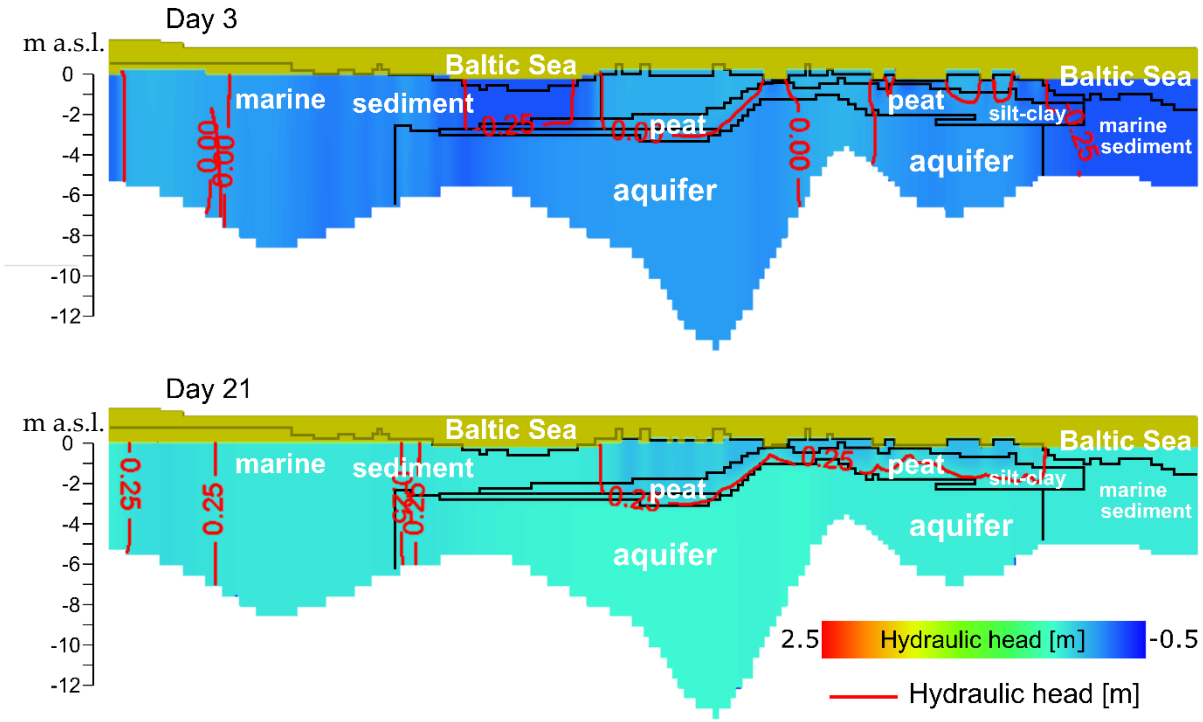

Figure 5.5: Geology and hydraulic heads along profile B along the beach at low sea level (Day 3) and high sea level (Day 21). Brown area indicates dry cells. Length of the profile 3000 m.

Three example profiles (Fig. 5.6 and 5.7) perpendicular to the coast are shown analogous for the geological cases described in Chapter 3 (Fig. 3.10) to illustrate the influence of geological heterogeneity on flow paths. The three profiles *a*, *b*, *c* are shown for day 3 with high SGD (Fig. 5.6) and day 21 with low SGD (Fig. 5.7). The arrows in Fig. 5.6 and 5.7 indicate flow direction. The flow direction is diverted in three directions in the actual simulation and although shown for 2D profiles here, the arrows have to be interpreted as 3D. In profile *a*, the peat crops out below the dune dike, in profile *b* it crops out offshore within the marine sediment, and in profile *c* it crops out in the shallow sea directly at the seafloor.

On both days, flow on the landside was directed downwards through the peat layer and within the aquifer towards the coast. In profile *c* the flow direction was influenced by a downward directed flow into the ancient glacial river valley south of profile *c*. Profile *a* lies closest to the ground sill and hence the surface water discharge led to enhanced upward directed flow in the upper peat towards the ditch system. In profile *b* the thick peat layer inhibited upward directed flow.

During low sea level (Fig. 5.6) groundwater flow at the shoreline was upward directed over the whole thickness in profile *a*. In profile *b* and *c*, flow was only upward directed above the peat layer. Below the peat, the groundwater flowed further seaward and upward where the peat crops out (profile *b* and *c*). There, SGD could occur in low rates.

During a high sea level (Fig. 5.7) there was still a seaward directed flow in the dune body but also inflow of seawater at the shoreline due to a zone of lower hydraulic heads that was maintained in the dune above the peat (Fig. 5.7 profile *b* and *c*). In profile *a* this zone extended over the whole depth of the profile below the dune. Flow in the offshore sediment was always downward in profile *a*, while in profile *b* and *c* the flow in the confined aquifer continued seaward and even upward, as far as the peat cropped out. Further seaward, flow was also directed downward within the sediment. Hence, the confining peat can lead to SGD in greater depth and further offshore despite higher sea levels.

The simulated flow directions depicted in Fig. 5.6 and 5.7 illustrate that downward flow of water through the peat on the landside will result in enhanced nutrient and carbon loads which were measured in the aquifer (Table A2), and eventually discharge into the sea. Where the peat crops out offshore (as in profile *b* and *c* in Fig. 5.6 and 5.7) the water will be in contact a second time with peat during upward directed flow. In case of profile *b* (Fig. 5.6 and 5.7) an upward flow of nutrient-enriched water in greater distance to the shoreline is possible. However, the peat is submerged in greater depth and hence the solutes will likely undergo biogeochemical processes in the marine sediments on top of the peat. In profile *c*

the nearshore peat is only partly covered with a thin sand layer. During low, but also during high sea level, flow was upward through the nearshore peat (profile c Fig. 5.6 and 5.7). In that area Jurasinski et al. (2018) reported enhanced CH_4 emissions.

Kreuzburg et al. (submitted) found in column experiments with sediment cores from the same shallow submerged peat area that low-saline, oxygen-poor groundwater discharge from below enhances the release of DOC from the peat and production of DIC with subsequent CO_2 emission. Methane production was enhanced in the peat due to higher microbial activity. Sulphate originating from downward flow of seawater, induced at the top of the column, resulted in lower DOC, DIC, CH_4 and CO_2 release.

The variation in SGD and SWI is highly time-dependent due to sea level fluctuations. The oscillation of downward and upward movement can enhance dispersive mixing despite low advective flow velocities (Reeve et al. 2000, 2001). Further, the quality (e.g. the carbon content) of the land-derived groundwater is important for biogeochemical reactions and CH_4 emissions (Porubsky et al. 2014). The quality is assumed to depend on the recharge point on the landside, the residence time in the peat of varying thickness and permeability, and the travel time through the aquifer towards its discharging point. The analysed water samples (Table A2) showed high DOC and nutrient concentrations in the central peat (6P and 7P) compared to the deep peat covered with dune sand (2P). Further, DIC was higher than DOC at 2P and 2LS (Table A2), indicating advanced mineralisation.

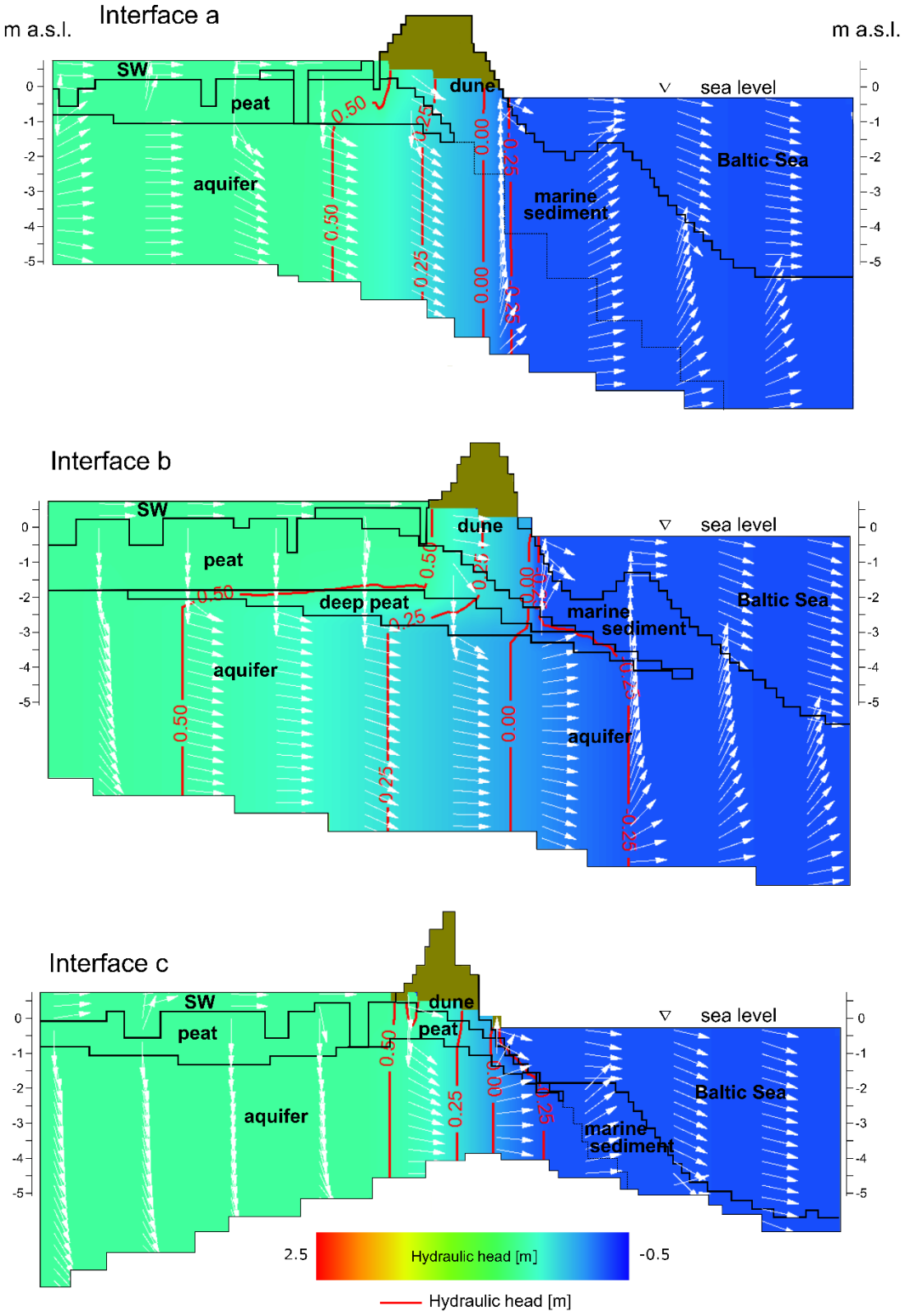

Figure 5.6: Groundwater flow direction (white arrows, not magnitude of flow) at the coastal interface with a sea level of -0.28 m a.s.l.. Length of the profile 677 m.

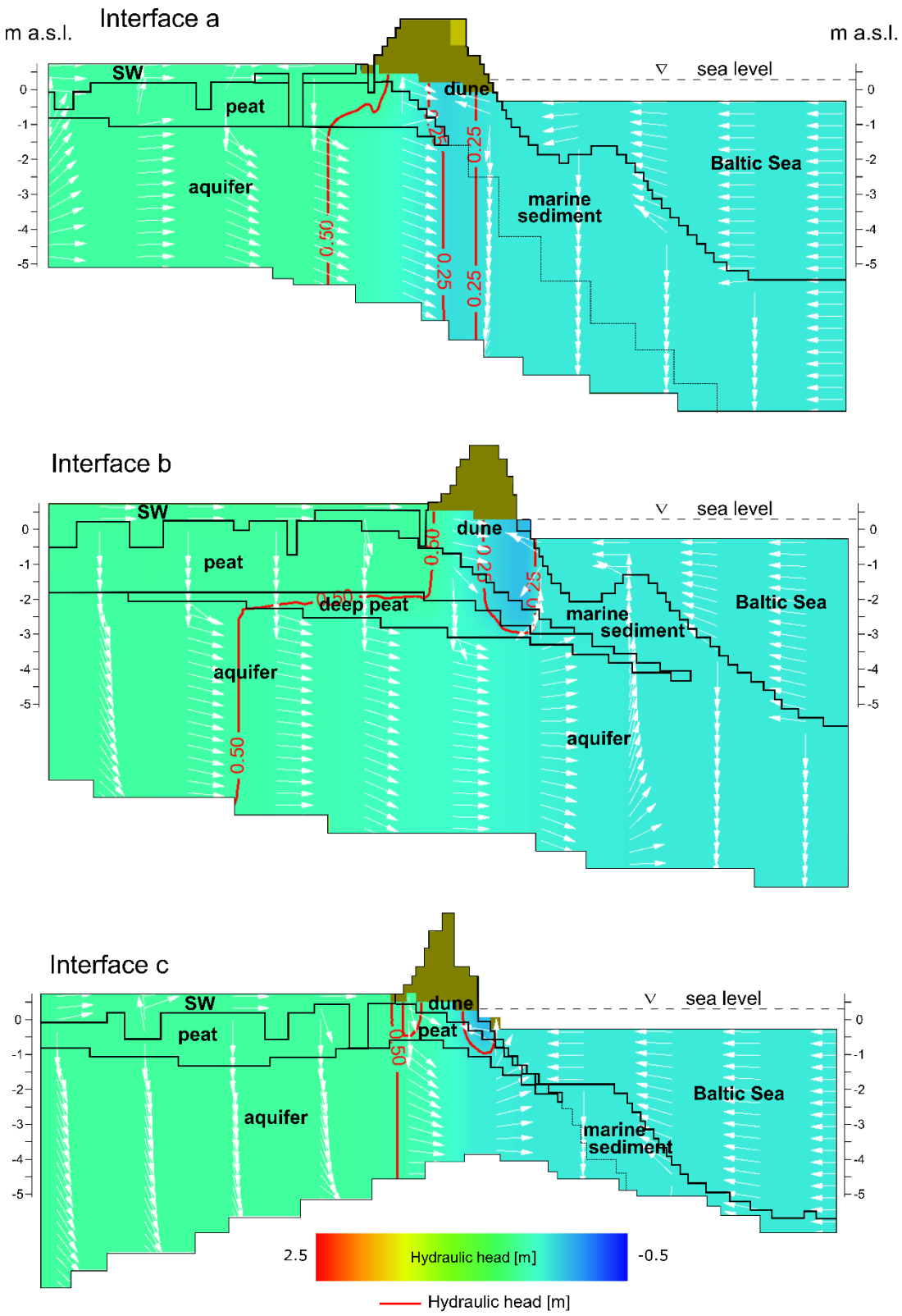

Figure 5.7: Groundwater flow direction (white arrows, not magnitude of flow) at the coastal interface with a sea level of 0.28 m a.s.l.. Length of the profile 677 m.

5.3 Heterogeneity of short-term flow reversals in the peatland

The quality and quantity of submarine groundwater discharge depends on the hydro(geo)logical state of the peatland. To illustrate groundwater flow in the peatland and the driving forces, two profiles, C and D, parallel to the shoreline were chosen with different hydro(geo)logical features and distance to the coast (Fig. 5.8). Profile C lies in 465 m distance to the coast and has a peat thickness of up to 2.5 m, and profile D lies in 1350 m distance to the coast with a peat thickness of up to 1 m. Profile D intersects the observation well MP7. Recharge and ET conditions are shown in terms of groundwater flow directions. Day 23 (recharge conditions) was characterized by a high sea level of 0.35 m, a recharge of 7.1 mm/d (or 343 L/s), and – due to the high recharge – by a Q_{SW} of 13.7 L/s. Day 13 (ET conditions) was characterized by a sea level of -0.03 m, an ET of -2.2 mm/d (or 51 L/s), and a Q_{SW} of 14.5 L/s.

In profile C (Fig. 5.8) the ditches partly cut into the aquifer. At the points where the peat is thicker, the shallow ditches are not in contact with the aquifer. The flow direction was in general influenced by a low seaward directed gradient (not visible in profile C). A larger gradient existed at the elevated north-eastern (right side) of the profile, leading to upward directed flow at the border between forest and peatland. Towards the southwest (left side) groundwater flow was southwest and upward directed due to increasing influence of ditches towards the ground sill. Both during recharge and ET conditions, groundwater flow was downward directed in the area with thick peat and shallow ditches. During recharge, this downward directed flow also occurred through thin peat and at ditches. The conceptual ideas in Chapter 3.2.6 only considered ditches as a discharge point. ET conditions with at the same time slightly enhanced discharge led to upward directed flow especially on the south-western side (ground sill), where large parts of the aquifer are connected to the ditch system, but also on the north-eastern side characterized by thin peat. Flow in the aquifer was diverted but mainly downward, except in the thinner part of the aquifer near the south-western border that was influenced by drainage.

In profile D (Fig. 5.8) the peat layer is very thin, and ditches cut into the aquifer. The aquifer geometry differs largely with up to 17 m thickness in the forest on the north-eastern side and partly only 2 m towards the southwest. The large hydraulic gradient at the border of forest and peatland led to an upward directed flow towards the ditches near the forest. Deep groundwater flowed upward where the aquifer gets thinner. During recharge conditions flow was in general downward through the peat layer, while during ET conditions flow was upward towards the ditches and partly downward between the ditches.

Hence, today small changes in recharge or ET lead to short-term flow reversals that influence groundwater flow both in the peat and the shallow aquifer, but to less or no extent in the deeper aquifer depending on the connectivity to ditches. Reeve et al. (2006) found through numerical simulations of groundwater flow of a bog-fen-complex (Glacial Lake Agassiz Peatland) that the amplitude of flow path reversals induced by varying recharge and ET increased with increasing peat storativity (due to specific storage) because the increased storage capacity maintained the vertical hydraulic head differences over a longer period and water could flow further. However, they further concluded that advective fluxes on a seasonal scale are not significant and vertical downward flow takes decades or longer. Vertical oscillation might enhance dispersive mixing over the peat column, especially when heterogeneities of the peat are considered (Reeve et al. 2001, 2006). This might have implications for the investigated site because the upper peat contains freshwater from the rewetting process, while in a depth below 30 cm brackish, and hence older water prevails (Koebsch et al. 2019). The apparent tritium-helium age of 7 years below in the aquifer at 7 LS, which is younger than the brackish water above (last inundation in 1995), indicates a preferential flow path. Furthermore, gas formation due to bacterial activity (Siegel et al. 2001, Rosenberry et al. 2003, Glaser et al. 2004), and ebullition (Romanowicz et al. 1993), can change hydraulic head gradients due to changes in pressure.

In general, it was seen that flow direction is a function of the aquifer geometry, peat thickness, depth of ditches, and distance to the coast. Seasonal short-term flow

reversals in the long-term might lead to a mixing of fresh and saltwater, however, freshwater is constantly supplied, and recharge conditions dominate. In the long-term changes in the hydrological system might affect the dominant flow direction (e.g. Kopp et al. 2013).

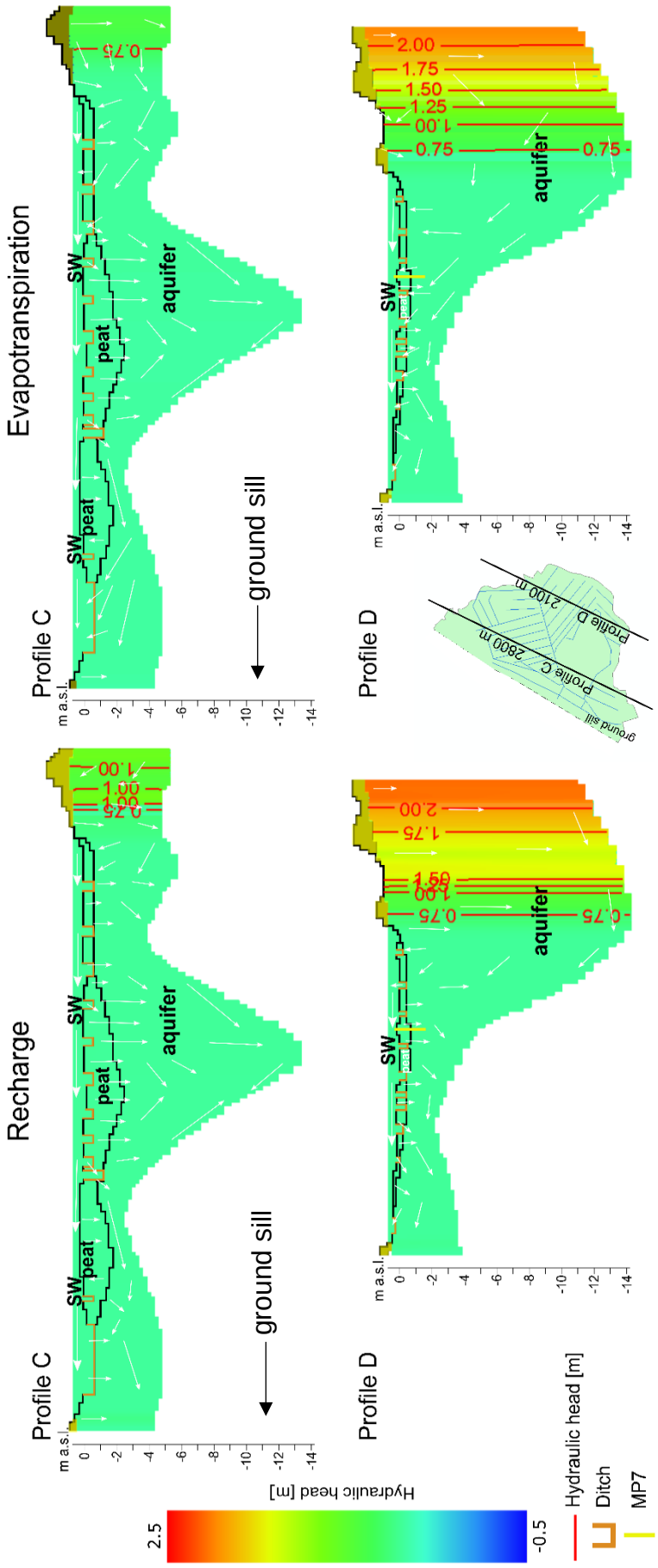

Figure 5.8: Groundwater flow directions (white arrow, not magnitude of flow) and hydraulic heads for profile C and D during recharge (Day23) and evapotranspiration conditions (Day 13).

5.4 Scenario simulation: long-term effects

Scenario simulations of pristine and drainage conditions in steady-state were performed to estimate the effect of anthropogenic interferences on (local) biogeochemistry, apparent groundwater age distribution (Chapter 3.2.4), and flow direction in the peatland and at the coastal interface. First, the pristine and drainage scenarios are briefly described individually, followed by a final comparison of the water balance and flow paths of the two scenarios pristine and drainage with today's conditions. Advective travel times and recharge and discharge points are compared for drainage and rewetting only, because the pristine scenario needs further adjustments to simulate realistic travel times. The boundary conditions of the calibrated steady-state model (Chapter 4.2.4, landside boundary, sea level (0.11m a.s.l.), recharge of 0.17 mm/d in the dune dike area) were assigned for all three scenarios. Changes to initiate the scenario are described in each scenario section.

5.4.1 Scenario I: pristine conditions

Pristine conditions were simulated in a first simple approach with the same BC's at the landside boundary as for the calibrated steady-state model, which implies the lowered constant heads at the southern border. In a second and third pristine scenario, additional recharge of 0.01 mm/d and 0.1 mm/d to the peat area was assigned because it was assumed that the scenario is more sensitive to recharge when the drainage system is absent, and the hydraulic conductivity of peat higher than today.

All hydraulic property zones previously defined as ditch or colmation layer were turned back into peat of aquifer as in the conceptual geological model (Chapter 4.2.2). The upper peat (according to Table 4.3) was assigned a K of $1*10^{-6}$ m/s (isotropic). K of the deep peat and peat below the dune dike was not changed. The surface water cells on the landside were assigned a K of $1*10^{-6}$ m/s. The surface elevation of the peat was then 0.75 m. Shallow creeks flowing through the peatland

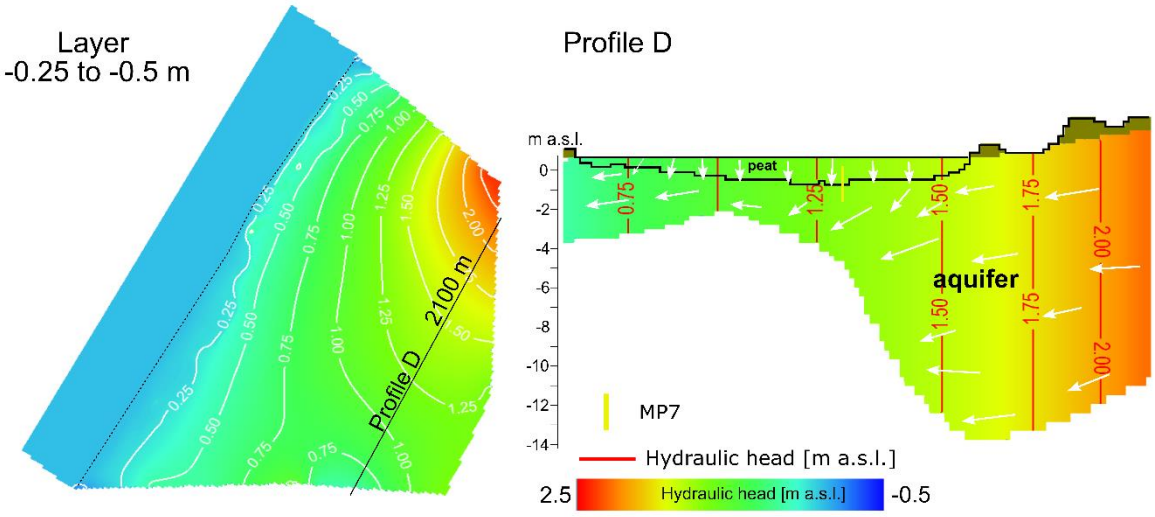

Figure 5.9: Simulated hydraulic head distribution in steady-state pristine conditions with additional recharge of 0.01 mm/d in the peat area. The white arrows indicate groundwater flow direction, not the magnitude of flow.

and discharging into the Baltic Sea were not considered in this simple scenario. The resulting hydraulic heads (Fig. 5.9) showed a smooth horizontal gradient from the forest to the Baltic Sea (Layer view Fig. 5.9). Inflowing groundwater originated from the elevated forest northeast. In profile D, horizontal flow in the aquifer towards the south dominated due to the lowered CHD-BC. Downward flow occurred in the peat without affecting much the horizontal flow direction in the underlying aquifer. Without additional recharge in the peat area, flow in the peat was also horizontal (not shown). Enhanced recharge of 0.1 mm/d (not shown) led to elevated hydraulic heads in the area of the 'Hütelmoor' (bog-type, Bohne and Bohne 2008) characterized by a shallow depth of the impermeable till.

In general, the simulated heads were in some areas higher than the elevation of the peat surface of 0.75 m (Fig. 5.9 Layer view). The influence of shallow creeks, which should not have been deeper than a few decimetres back then, should be further tested. However, the drainage function of a few shallow creeks was spatially limited. Surface and sub-surface water discharge in the micro-relief (e.g. Frei et al. 2010) is another process not considered that would decrease the simulated hydraulic heads (Fig. 5.9). A simple numerical approach to minimize over-pressurized zones was demonstrated by (Feinstein et al. 2019) by implementing

seepage with the Unsaturated Zone Flow (UZF) package (Niswonger and Prudic 2006) in MODFLOW for a regional steady-state simulation of a fen fed by discharging groundwater. This should be considered for the pristine scenario to obtain a more realistic hydraulic head distribution.

5.4.2 Scenario II: drainage

To initiate drainage, a CHD-BC at the elevation of the river bed (- 0.5 m a.s.l.) of the ground sill was assigned. To initiate a larger drawdown of the water level as reported for periods of more intensive drainage, the BC (pumping well) would have needed to be placed in the deeper main ditch, where the actual pumping station was located. However, the CHD-BC at the ground sill led to a decrease of the water level down to -0.2 m (equal to the depth of the riverbed at the ground sill) in the peatland and thus below sea level (Fig. 5.10). The water level near MP1 did not drop as far as in the area influenced by ditches. In profile C and D (Fig. 5.10) it can be seen that the groundwater flow in the aquifer and in the peat was upward directed despite a thick peat layer in profile C. Flow between the ditches was mainly toward the next ditch in direction of the ground sill seen in the profiles C and D, but also in the horizontal view ("Layer" in Fig. 5.10). A general low hydraulic gradient from the northern to the southern (ground sill) part of the peatland exists. The upward directed flow is also well seen in Fig. 5.10 (profile D).

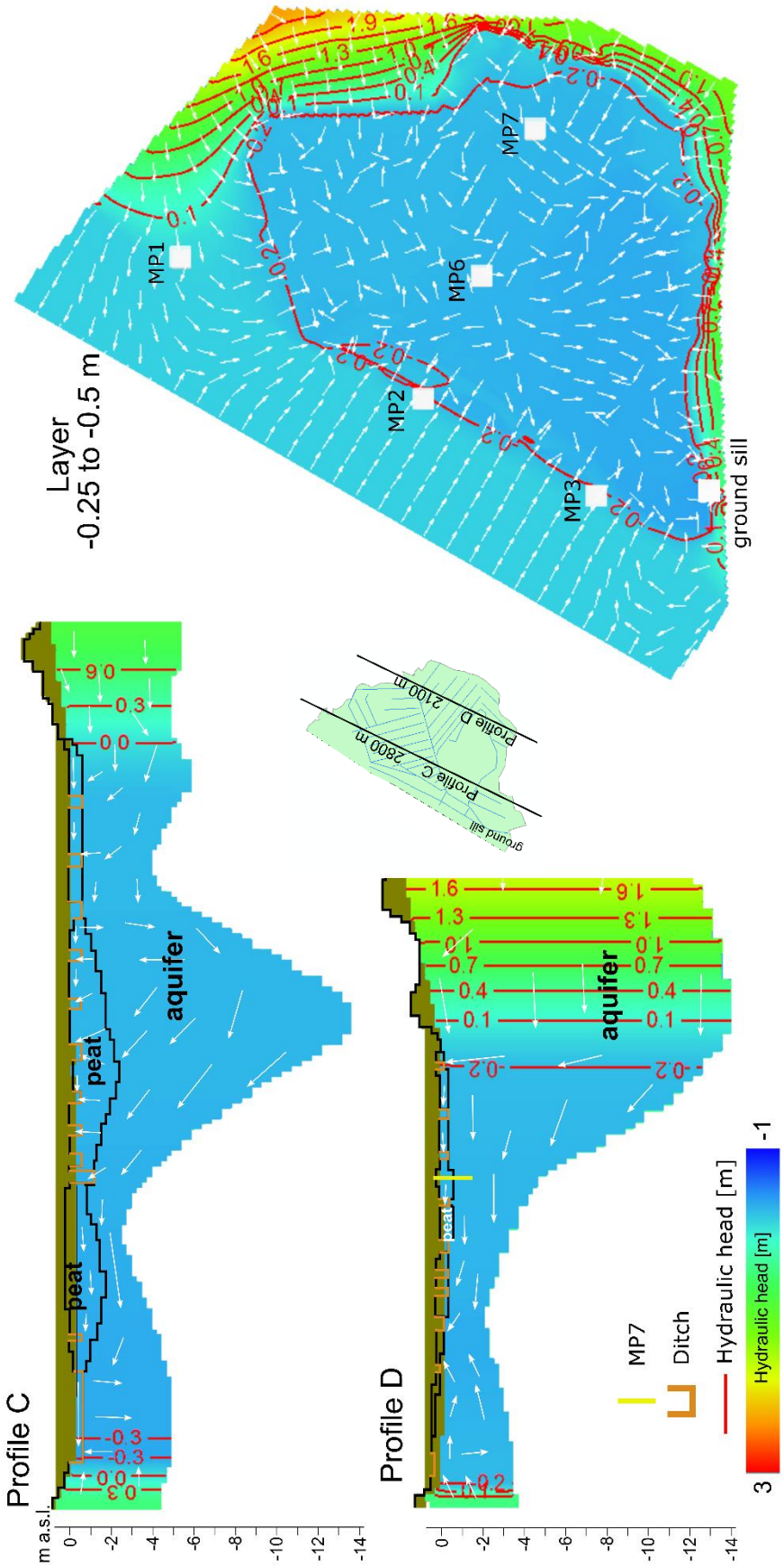

Figure 5.10: Groundwater flow direction (white arrows) and hydraulic heads under intensive drainage conditions. Note that the arrows only indicate direction of flow. Brown cells are dry. The colour scale for hydraulic heads here is slightly different.

5.4.3 Comparison of pristine, drained and rewetted scenario

5.4.3.1 Flow paths and water balance

The comparison of the 3 steady-state scenarios Pristine, Drainage and Rewetted in Fig. 5.11 illustrates the heterogeneous flow patterns within the peatland induced by drainage ditches, and at the coastal interface induced in combination with reversed hydraulic gradients during drainage. The ditch system under rewetted conditions induces a stronger hydraulic gradient at the coast in the dune than under pristine conditions (Fig. 5.11). This further leads to downward flow through the peat into

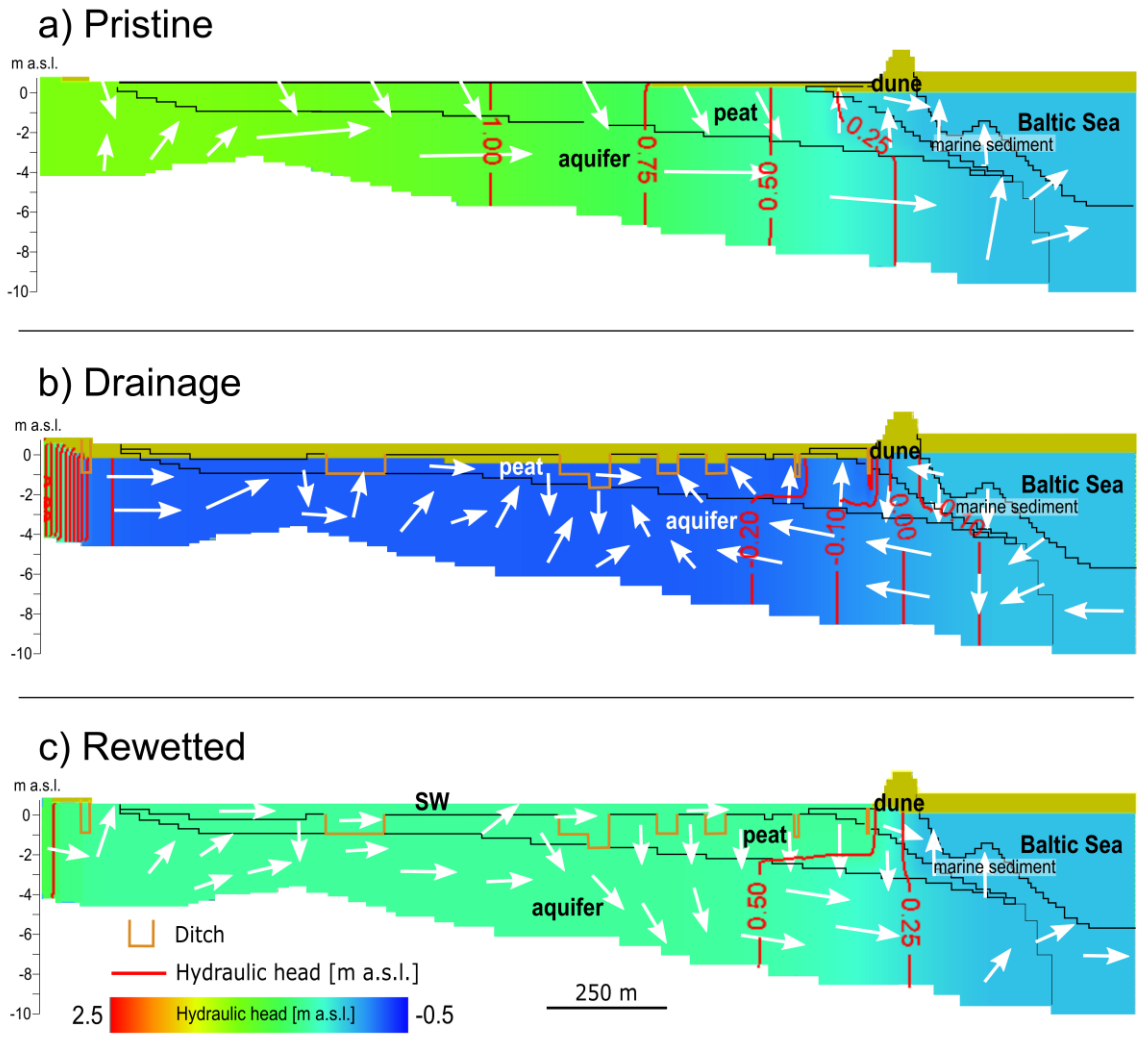

Figure 5.11: Hydraulic head distribution along profile A for the 3 scenarios: Pristine (neglecting any kind of surface water discharge), Drainage and Rewetted (today). White arrows indicate only flow direction. Brown cells are dry. Profile length is 2300 m.

the aquifer today, while in the pristine state flow was upward. The upward flow could supply solutes from the aquifer and the peat to the upper dune and beach interface. This had consequences for the SGD rate, which was two times higher in the rewetted scenario (Table 5.1) compared to the pristine state. SWI for the two scenarios was the same. During drainage, SWI was higher and SGD decreased largely (Table 5.1). In general, the SGD and SWI rates were low compared to transient conditions (see Fig. 5.3). A fluctuating sea level might enhance the exchange between sea and sediment (recirculating seawater). Hence, the SGD rates under steady-state conditions might rather reflect freshwater SGD.

Table 5.1: Simulated water balance of the steady-state scenarios.

Rate L/s	Pristine	Drainage	Rewetted
Recharge	0.74	0.74	0.74
SGD	0.97	0.16	2.08
SWI	0.72	1.21	0.72
Q_{sw}	-	10.74	9.01

5.4.3.2 Recharge and discharge points during drainage and rewetting

To estimate the influence of changed hydrological conditions on travel times with consequences for transport processes MODPATH was used. MODPATH calculated travel times (Fig. 5.12) both for forward and backward tracking (10 particles in a radius of 5 m) from the well screens 2LS, 6LS and 7LS, which then were compared to apparent groundwater ages (Chapter 3.2.4). Further, recharge and discharge points of the water particles were identified (Fig. 5.13). This was done for the rewetted case and drainage scenario because they impacted mainly today's water composition. The pristine scenario needs further adjustments before it can be used to estimate flow paths and travel times.

Backward tracking was used to visualize and calculate the flow path and time a water particle needs to reach the filter screen, and forward tracking was used to visualize and calculate the flow path to the discharge point of water passing the filter screen. The presented flow paths and travel times are highly dependent on recharge or ET conditions, hydraulic gradients, and hydraulic conductivity (part of the calibration) and effective porosity of the geological zones. Meyer et al. (2018) emphasized the importance of n_e for advective flow paths. Therefore, the sensitivity to changes of n_e from originally 0.12 to 0.08 for the aquifer (0.08 to 0.12 is the range for silty sand according to Hölting and Coldewey 2013) was tested for the rewetted case (Table 5.2).

Table 5.2: Backward and forward particle paths with years to travel the distance from the recharge point to the filter screen (2LS, 6LS, 7L,S respectively) and from the filter screen to the discharge point, respectively. n_e for the aquifer was 0.12, the rewetted case was tested also with a n_e of 0.08 (years in brackets). For further values of n_e see Table 4.3.

Particle path		Rewetted	Drainage
2LS backward	Years	82 (76)*	68
	Distance [m]	88	94
	Recharge point/ depth in [m a.s.l.]	Between 1st and 2nd ditch landwards from MP2/ land surface	Shallow sea/ 0 to -0.5 m
2LS forward	Years	53 (46)	74
	Distance [m]	107	190
	Discharge point/ depth [m a.s.l.]	Nearshore/ – 1m	2nd ditch landwards/ -1 m
6LS backward	Years	131 (87)	865
	Distance [m]	18	795
	Recharge point/ depth [m a.s.l.]	Main ditch/ -1.5 m	Sandbar offshore/ -1 m
6LS forward	Years	746 (498)	27
	Distance [m]	821	36
	Discharge point/ depth [m a.s.l.]	Sandbar offshore/ -1.5 to -2 m	Main ditch/ -1.6 m
7LS backward	Years	8000	540
	Distance [m]	100	405
	Recharge point/ depth [m a.s.l.]	Aquifer	Glacial valley/ -14 m
7LS forward	Years	8000	1046
	Distance [m]	85	276
	Discharge point	Ditches/aquifer	Ditches

Under drainage conditions the water at 7LS originated from the bottom of the ancient glacial river valley in 13 m depth (Fig. 5.13) and flowed upwards at the slope of the valley-ridge structure (Fig. 5.10 profile D) (the real recharge point was probably outside the model domain). The total flow path length was 405 m and took 540 years for the water particles to reach 7LS. Under steady-state conditions today water would originate from within the aquifer and is partly diverted by ditches (Fig. 5.12). However, flow would be very slow (Table 5.2).

The transient simulation of today's conditions however showed vertical flow reversals in the peat layer near MP7. Upwelling was only enhanced during increased ET and surface water discharge. Reeve et al. (2006) pointed out, based on several studies (e.g. Glaser et al. 1997, Reeve et al. 2001, Siegel 1983) that vertical flow in large peat basins is driven by permeable mineral sediments below the peat with distant recharge zones, and valley-ridge structures of the bedrock (e.g. impermeable till) that force groundwater to flow upwards. Locally enhanced upwelling of old groundwater that recharged in the surrounding forest with a podsol soil could have led to enhanced iron supply (depending on the pH and redox conditions) to areas in the peatland impacted by the ancient glacial river valley structure and ditches cutting into the aquifer (Fig. 5.12). Koebsch et al. (2019) found enhanced concentrations of iron-species near MP7 (see also Chapter 3.2.3) with local consequences for biogeochemical processes, but without effects on ecosystem scale.

At 6LS water originates today from infiltration at the bottom of the nearby 'Prahmgraben' (main ditch) at -1.5 m depth. It would take 131 years to reach the filter screen. Afterwards, the water flows downward in the ancient river valley structure to -9 m, followed by abrupt upward flow approx. 100 m offshore with the discharge point at the elevated sandbar. The flow path from 6LS to the sandbar would take 746 years. During drainage, this flow path was simply reversed, taking 865 years from the sand bar to 6LS, and another 27 years to discharge into the main ditch. Hence, the water component not dateable with the tritium-helium method and relatively high $^4He_{rad}$ concentrations (Chapter 3.2.4) originated from upward flow of old water from the ancient glacial river valley. The younger water component of apparent 56 years (Chapter 3.2.4) would be too young compared to the simulated time it takes under today's conditions to reach 6LS from recharge through the ditch. Recharge was enhanced after the rewetting in 2010 and could have led to faster downward flow. Also ΔNe indicates recharge through the peat as a source for a part of the water sample. The investigated flow paths are based on particles that were only placed in one depth around the well screen. However,

during pumping, water from different depths and a larger radius was sampled and hence, some amount of the water sampled could have also originated from recharge through the peat that was not tracked with MODPATH.

Groundwater ages older than dateable with the tritium-helium method at 2LS could result from low recharge through the peat but given the hydrological changes, a landward flow during drainage and a subsequent seaward flow suggest a long residence time of the water. High ΔNe and a low $^{4}He_{rad}$ concentration (Chapter 3.2.4) indicate a long residence time of the water in the peat. This can be explained with initial recharge of imaginary water particles, that were sampled in 2017, into the peat before intensive drainage was initiated, assuming that moderate drainage over centuries without pumping did not led to water levels below sea level. Intensive drainage led to subsequent upward flow in the peat towards the ditch, and finally rewetting resulted in a downward flow of the particles through the peat into the aquifer.

Overall, the advective flow ages indicate long residence times. Hence, a period of 20 years of intensive drainage would not have been enough to lead to significant saltwater intrusion at the coast. Also upwelling of old groundwater enriched with solutes like iron could not have been limited to that period. Moderate drainage persisted for centuries, and a low upward directed flow was likely. Further, the pristine scenario simulation should be investigated with adjusted BC's and shallow creeks to estimate the intensity of upwelling.

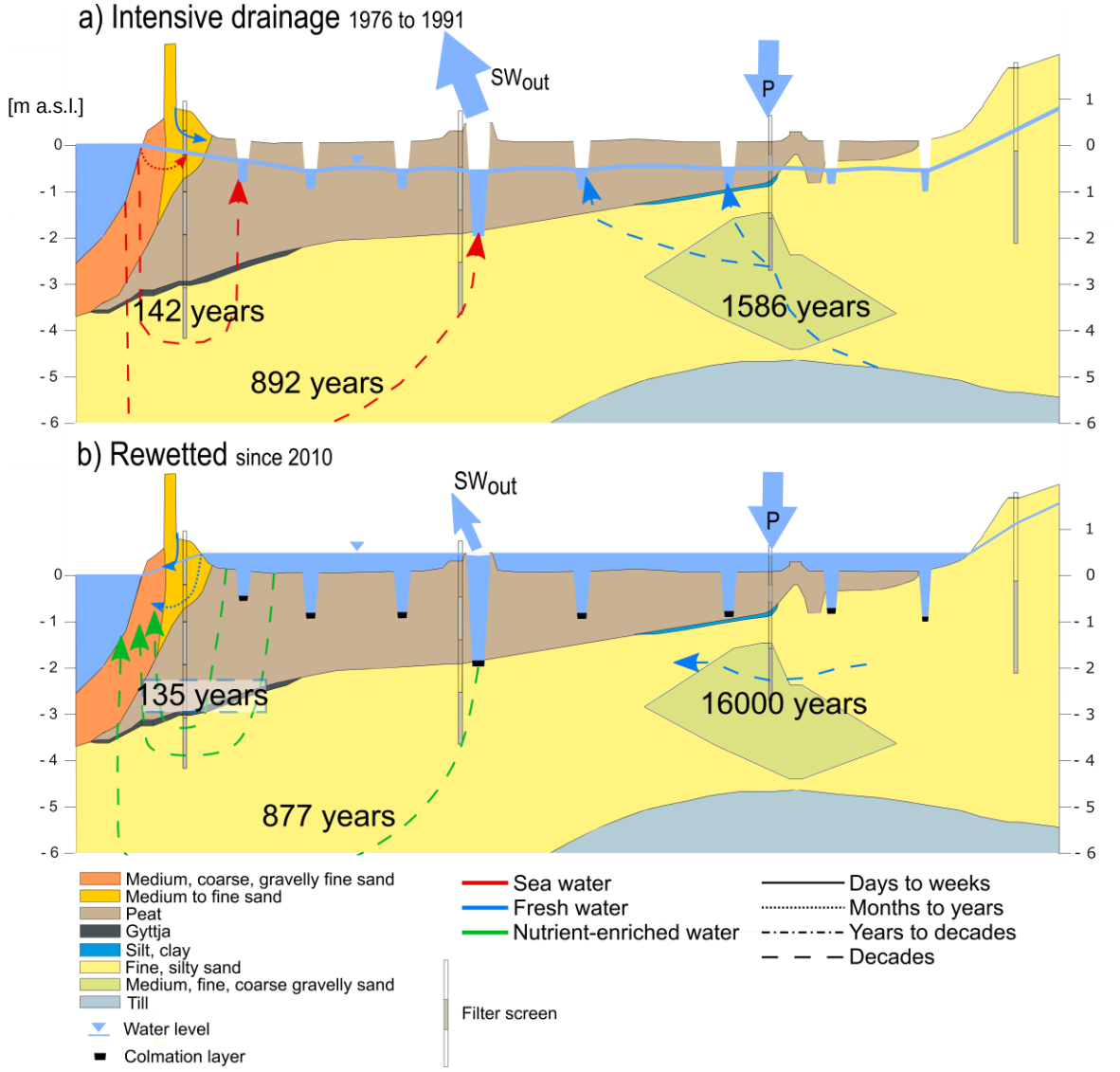

Figure 5.12: Illustration of flow paths and travel times from recharge to discharge point derived with particle tracking. For values of n_e see Table 4.3. Note that only recharge and steady-state conditions were considered. Note in a) that the water level is in the simulation around -0.2 m a.s.l. in the peatland; the recharge point at 7LS was at -13 m depth (outside the profile).

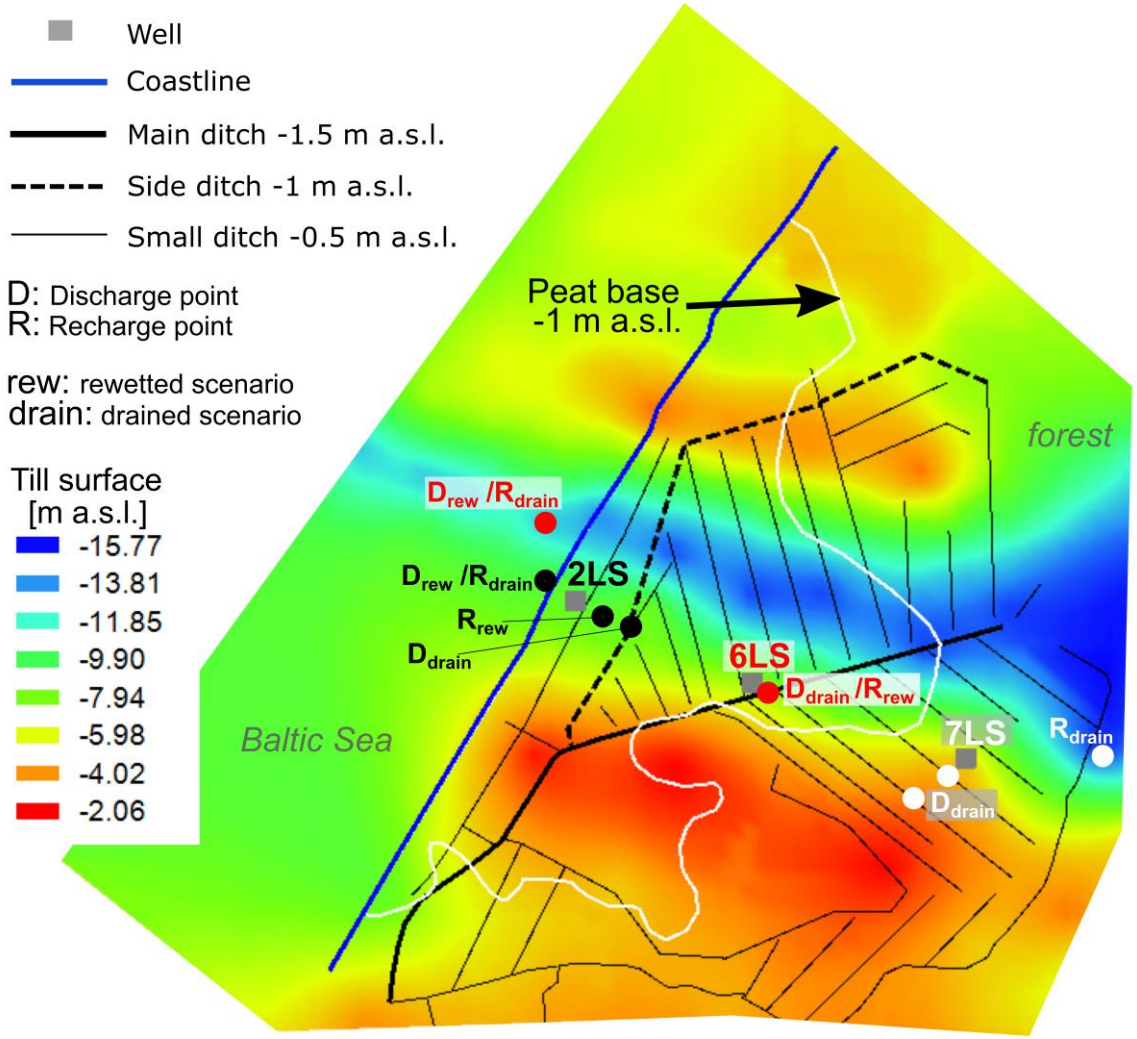

Figure 5.13: Discharge and recharge points for the rewetted and drained scenario for tracked water particles at individual filter screens of 2LS, 6LS and 7LS (grey squares). Depth of ditches (dashed or solid lines), peat base of -1 m a.s.l. (white line) and depth of the till surface is shown to illustrate hydraulic complexity. Towards the coast the peat base increases in depth, towards the land it decreases in depth and ditches are better connected to the underlying aquifer.

6 Conclusions and outlook

In a coastal fen hydrological conditions have changed over time following anthropogenic interferences (drainage, dike construction, rewetting). These changes were reconstructed by a combination of different proxies (chloride, tritium-helium groundwater ages, ΔNe, $^{4}He_{rad}$), today's hydraulic head and EC distribution, and numerical modelling.

A fine discretized 3D-groundwater flow model with surface water bodies implemented as high conductive zones unraveled complex groundwater flow paths in a system with very low groundwater flow velocities and water level differences. Transient simulation on a daily basis and steady-state simulations of different hydrological stages helped to differentiate between driving forces of groundwater flow on a short-term and on a long-term scale.

These heterogeneous flow patterns determined the distribution of salts and other compounds in the peat and aquifer, which crucially affect biogeochemical processes in the peat such as methane production. A wide range of groundwater ages and a mostly homogeneous distribution of chloride concentrations in the aquifer indicate that brackish conditions as a result of seawater inundations have prevailed over centuries.

The transient simulation on a daily basis showed clearly that short-term – usually weather-induced – vertical fluxes in the peat dominate. Daily changes of recharge and evapotranspiration, but also seasonal or interannual (e.g. droughts) varying climatic conditions lead to vertical oscillations. Steady-state simulations might oversee these processes with further impacts on water chemistry in the peat.

Changes in the overall advective groundwater flow direction due to principal changes of hydrological conditions, and involved advective transport, are more important on a larger timescale of several decades to centuries, as seen in the steady-state simulations. Hydrodynamic dispersive transport is assumed to dominate within a specific hydrological condition (e.g. intensive drainage) that controls the

overall advective flow, due to generally low groundwater flow velocities, and heterogeneities of mainly the peat. The low groundwater flow velocities also increase the time for biogeochemical reactions. On a short timescale, alternating recharge and evapotranspiration are decisive for biogeochemical reactions in the upper peat due to vertical oscillation enhancing dispersive mixing.

Preferential flow paths in the peat were identified through young apparent tritium-helium groundwater ages below the peat with brackish and hence older water above in the peat. The derived advective travel times from steady-state simulations of drained and rewetted conditions were not able to explain the younger apparent tritium-helium groundwater ages below the peat. This requires a transient simulation of the rewetting process. Further, peat heterogeneities and preferential flow paths should be investigated as they impact on dispersive transport.

At the coastal interface, rewetting revives and even enhances – compared to pristine conditions – submarine groundwater discharge despite low hydraulic gradients. It originates both from the deep, nutrient-enriched groundwater of the aquifer and from the rain-fed dune dike. The simulated groundwater flow paths and the water composition indicate that deep, land-derived submarine groundwater discharge differs in quality depending on its recharge point and the residence time in the peat and aquifer, where it undergoes biogeochemical reactions. Also, in the offshore peat dispersive mixing caused by vertical flow reversals is assumed to drive biogeochemical processes. The flow reversals are caused by the varying amount of land-derived SGD and advective porewater fluxes at the sediment-sea interface due to sea level fluctuations.

The deduced flow patterns are transferable to other coastal peatlands and peatlands in general, typically experiencing the same sequence of anthropogenic influences. However, the spatial complexity of groundwater flow suggests that geological features must be investigated individually at each site. The peat thickness, degradation of the peat, and connectivity of ditches to the aquifer lead to preferential recharge and discharge points depending on the hydrological state. In

general, the aquifer geometry in complex glacial deposit environments is decisive for discharge and recharge areas that either result in fen- or bog-type peatlands. Drainage can disturb the natural discharge and recharge areas with implications for the water chemistry, water table, and vegetation type. The extent and hydraulic properties of the underlying mineral sediment are assumed to further impact the connectivity with the adjacent sea, or a river or lake.

The modelling approach was very detailed with the objective to illustrate complex spatial and temporal variable groundwater flow patterns hydraulically connected to the adjacent Baltic Sea and to be able to use the model as a tool to explain biogeochemical processes observed at the study site. The latter must be further implemented in ongoing research to confirm the relevance of the simulated flow patterns for biogeochemical processes. For example, the model can be a helpful tool for a strategic sampling both on the land- and seaside. To simulate reactive transport processes, the relatively large model might not be convenient due to the complexity of the biogeochemistry. However, the current groundwater flow model can be used to define local boundary conditions for transport models.

The model results, especially simulated SGD and SWI rates and locations at the coastal interface, should be improved through implementing variable-density flow. However, this requires careful development of the current density distribution which is likely not in a steady-state but influenced by previous hydrological conditions. Further, the model can be used for additional scenario simulations like a rising sea level.

For future investigations of similar locations, the knowledge of the history of the site, duration of individual hydrological stages, as well as the extent and the hydraulic characteristics of the peat and the underlying aquifer, can already help to improve the understanding of biogeochemical processes. For water management purposes simplifications in the modelling approach are possible (e.g. only simulating steady-state).

7 References

Åberg, S.C., Korkka-Niemi, K., Rautio, A., Veli-Pekka, S., Åberg, A.K., 2019. Groundwater recharge/discharge patterns and groundwater– surface water interactions in a sedimentary aquifer along the river kitinen in Sodankylä, northern Finland. Boreal Environ. Res. 24, 155–187.

Andersen, M.S., Baron, L., Gudbjerg, J., Gregersen, J., Chapellier, D., Jakobsen, R., Postma, D., 2007. Discharge of nitrate-containing groundwater into a coastal marine environment. J. Hydrol. 336, 98–114. https://doi.org/10.1016/j.jhydrol.2006.12.023

Anderson, M.P., Hunt, R.J., Krohelski, J.T., Chung, K., 2002. Using high hydraulic conductivity nodes to simulate seepage lakes. Ground Water 40, 117–122. https://doi.org/10.1111/j.1745-6584.2002.tb02496.x

Ardón, M., Helton, A.M., Bernhardt, E.S., 2016. Drought and saltwater incursion synergistically reduce dissolved organic carbon export from coastal freshwater wetlands. Biogeochemistry 127, 411–426. https://doi.org/10.1007/s10533-016-0189-5

Ardón, M., Morse, J.L., Colman, B.P., Bernhardt, E.S., 2013. Drought-induced saltwater incursion leads to increased wetland nitrogen export. Glob. Chang. Biol. 19, 2976–2985. https://doi.org/10.1111/gcb.12287

Beyer, W., 1964. Zur Bestimmung der Wasserdurchlässigkeit von Kiesen und Sanden aus der Kornverteilung. Wasserwirtschaft-Wassertechnik (WWT) 14, 165–169.

Bohne, B., Bohne, K., 2008. Monitoring zum Wasserhaushalt einer auf litoralem Versumpfungsmoor gewachsenen Regenmoorkalotte - Beispiel Naturschutzgebiet „Hütelmoor“ bei Rostock. Weißensee Verlag, Berlin.

Bundesamt für Seeschifffahrt und Hydrographie (BSH), 2018.

Burnett, W.C., Bokuniewicz, H., Moore, W.S., Taniguchi, M., 2003. Groundwater and pore water inputs to the coastal zone. Biogeochemistry 66, 3–33. https://doi.org/10.1023/B:BIOG.0000006066.21240.53

Canfield, D.E., 2001. Isotope fractionation by natural populations of sulfate-reducing bacteria. Geochim. Cosmochim. Acta 65, 1117–1124. https://doi.org/10.1016/S0016-7037(00)00584-6

Chambers, L.G., Reddy, K.R., Osborne, T.Z., 2011. Short-term response of carbon cycling to salinity pulses in a freshwater wetland. Soil Sci. Soc. Am. J. 75, 2000. https://doi.org/10.2136/sssaj2011.0026

Chason, D.B., Siegel, D.I., 1986. Hydraulic conductivity and related physical properties of peat, lost river peatland, northern minnesota. Soil Sci. 142, 91–99. https://doi.org/10.1097/00010694-198608000-00005

Cogley, J.G., 1979. Reply to comments on “The albedo of water as a function of latitude”. Mon. Weather Rev. https://doi.org/10.1016/0198-0254(80)95759-3

Cooper, H.H., 1959. A hypothesis concerning the dynamic balance of fresh water and salt water in a coastal aquifer. J. Geophys. Res. 64, 461–467. https://doi.org/10.1029/jz064i004p00461

Dahms, P., 1991. Studie Wasserregulierung Hütelmoor. Rostock.

Devito, K.J., Waddington, J.M., Branfireun, B.A., 1997. Flow reversals in peatlands influenced by local groundwater systems. Hydrol. Process. 11, 103–110. https://doi.org/10.1002/(SICI)1099-1085(199701)11:1<103::AID-HYP417>3.0.CO;2-E

Drexler, J.Z., Bedford, B.L., Scognamiglio, R., Siegel, D.I., 1999. Fine-scale characteristics of groundwater flow in a peatland. Hydrol. Process. 13, 1341–1359. https://doi.org/10.1002/(SICI)1099-1085(19990630)13:9<1341::AID-HYP810>3.0.CO;2-5

DWD (Deutscher Wetterdienst), 2018. Warnemünde. Available online at https://www.dwd.de/DE/wetter/wetterundklima_vorort/mecklenburg-vorpommern/warnemuende/_node.html. Last accessed 08/10/2018

Erkens, G., Van Der Meulen, M.J., Middelkoop, H., 2016. Double trouble: Subsidence and CO 2 respiration due to 1,000 years of Dutch coastal peatlands cultivation. Hydrogeol. J. 24, 551–568. https://doi.org/10.1007/s10040-016-1380-4

Feinstein, D.T., Hart, D.J., Gatzke, S., Hunt, R.J., Niswonger, R.G., Fienen, M.N., 2019. A simple method for simulating groundwater interactions with fens to forecast development effects. Groundwater 169–187. https://doi.org/10.1111/gwat.12931

Fofonoff, N.P., Millard Jr, R.C., 1983. Algorithms for the computation of fundamental properties of seawater. UNESCO Tech. Pap. Mar. Sci. 44, 53.

Fraser, C.J.D., Roulet, N.T., Lafleur, M., 2001. Groundwater flow patterns in a large peatland. J. Hydrol. 246, 142–154. https://doi.org/10.1016/S0022-1694(01)00362-6

Frei, S., Lischeid, G., Fleckenstein, J.H., 2010. Effects of micro-topography on surface–subsurface exchange and runoff generation in a virtual riparian wetland — A modeling study. Adv. Water Resour. 33, 1388–1401. https://doi.org/10.1016/j.advwatres.2010.07.006

Glaser, P.H., Hansen, B.C.S., Siegel, D.I., Reeve, A.S., Morin, P.J., 2004. Rates, pathways and drivers for peatland development in the Hudson Bay Lowlands, northern Ontario, Canada. J. Ecol. 92, 1036–1053. https://doi.org/10.1111/j.0022-0477.2004.00931.x

Glaser, P.H., Siegel, D.I., Romanowicz, E.A., Shen, Y.P., 1997. Regional Linkages Between Raised Bogs and the Climate, Groundwater, and Landscape of North-Western Minnesota. J. Ecol. 85, 3. https://doi.org/10.2307/2960623

Global Network of Isotopes in Precipitation (GNIP).

Gorham, E., 1995. The biogeochemistry of northern peatlands and its possible responses to global warming, in: Woodwell, G.M., Mackenzie, F.T. (Eds.), Biotic Feedbacks in the Global Climate System: Will the Warming Feed the Warming? Oxford Univ. Press, pp. 169–187.

Gosch, L., Janssen, M., Lennartz, B., 2018. Impact of the water salinity on the hydraulic conductivity of fen peat. Hydrol. Process. 32, 1214–1222. https://doi.org/10.1002/hyp.11478

Greskowiak, J., 2014. Tide-induced salt-fingering flow during submarine groundwater discharge. Geophys. Res. Lett. 41, 6413–6419. https://doi.org/10.1002/2014GL061184

Grinsted, A., Jevrejeva, S., Riva, R.E.M., Dahl-Jensen, D., 2015. Sea level rise projections for Northern Europe under RCP8.5. Clim. Res. 64, 15–23. https://doi.org/10.3354/cr01309

Häckel, H., 1999. Meteorologie, 4th ed. Ulmer, Stuttgart.

Hahn, J., Köhler, S., Glatzel, S., Jurasinski, G., 2015. Methane exchange in a coastal fen in the first year after flooding - A systems shift. PLoS One 10, 1–25. https://doi.org/10.1371/journal.pone.0140657

Hallema, D.W., Périard, Y., Lafond, J.A., Gumiere, S.J., Caron, J., 2015. Characterization of water retention curves for a series of cultivated histosols. Vadose Zo. J. 14, 0. https://doi.org/10.2136/vzj2014.10.0148

Harbaugh, A.W., 1990. A computer program for calculating subregional water budgets using results from the U.S. Geological Survey Modular Three-Dimensional Finite- Difference Ground-Water Flow Model. https://doi.org/https://doi.org/10.3133/ofr90392

Harbaugh, A.W., Banta, E.R., Hill, M.C., McDonald, M.G., 2000. MODFLOW-2000 , The U. S. Geological Survey Modular Ground-Water Model - User Guide to Modularization Concepts and the Ground-Water Flow Process: U.S. Geological Survey Open-File Report 00-92 (ALSO LPF). Open-File Rep. 00-92 121.

Hazen, A., 1892. Some physical properties of sands and gravels, with special reference to their use in filtration. Boston.

Heathwaite, A.L., 1993. Mires: process, exploitation and conservation. John Wiley & Sons, Chichester.

Helton, A.M., Bernhardt, E.S., Fedders, A., 2014. Biogeochemical regime shifts in coastal landscapes : the contrasting effects of saltwater incursion and agricultural pollution on greenhouse gas emissions from a freshwater wetland 133–147. https://doi.org/10.1007/s10533-014-9986-x

Hoag, R.S., Price, J.S., 1997. The effects of matrix diffusion on solute transport and retardation in undisturbed peat in laboratory columns. J. Contam. Hydrol. 28, 193–205. https://doi.org/10.1016/S0169-7722(96)00085-X

Hölting, B., Coldewey, W.G., 2013. Hydrogeologie. Spektrum Akademischer Verlag, Heidelberg. https://doi.org/10.1007/978-3-8274-2354-2

HRO (Hanse- und Universitätsstadt Rostock), 2017. Karte der Hanse- und Universitätsstadt Rostock und Umgebung nach Friedrich Wilhelm Carl Graf von Schmettau von 1788 im Originalmaßstab 1:50000 (Map of the city of Rostock and surroundings after Friedrich Wilhelm Carl Graf von Schmettau from 1788 in original scale 1:50000). Available online at https://www.opendata-hro.de/dataset/schmettau_1788, last accessed 28/08/2019

Huettel, M., Ziebis, W., Forster, S., Luther, G.W., 1998. Advective transport affecting metal and nutrient distributions and interfacial fluxes in permeable sediments. Geochim. Cosmochim. Acta 62, 613–631. https://doi.org/10.1016/S0016-7037(97)00371-2

Hyder, Z., Butler, J.J., McElwee, C.D., Liu, W., 1994. Slug tests in partially penetrating wells. Water Resour. Res. 30, 2945–2957. https://doi.org/10.1029/94WR01670

International Atomic Energy Agency (IAEA).

IOW (Leibniz Institute for Baltic Sea Research Warnemünde) 2018. Environmental

long-term data programme, station TFO5 - Oceanographic Database Search with Interactive Navigation - ODIN2. Available online at https://odin2.io-warnemuende.de/#/

Iqbal, M., 1983. An introduction to solar radiation. Academic Press.

Ivanov, K.E., 1981. Water movement in Mirelands. Academic Press, London.

Jiao, J., Post, V., 2019. Coastal Hydrogeology. Cambridge University Press. https://doi.org/10.1017/9781139344142

Johnson, A.I., 1967. Specific yield: compilation of specific yields for various materials. Washington, D.C. https://doi.org/10.3133/wsp1662D

Jonathan, S.P., Susanne, M.S., 1999. Importance of shrinkage and compression in determining water storage changes in peat: the case of a mined peatland. Hydrol. Process. 13, 2591–2601.

Joosten, H., 1997. European mires: a preliminary status report. Int. Mire Conserv. Group Members Newsl.. 3. 10-13.

Joosten, H., Tanneberger, F., Moen, A. (Eds.), 2017. Mires and peatlands of Europe. Schweizerbart Science Publishers, Stuttgart, Germany.

Jørgensen, B.B., 1982. Ecology of the bacteria of the sulphur cycle with special reference to anoxic-oxic interface environments. Philos. Trans. R. Soc. Lond. B. Biol. Sci. 298, 543–561. https://doi.org/10.1098/rstb.1982.0096

Jurasinski, G., Janssen, M., Voss, M., Böttcher, M.E., Brede, M., Burchard, H., Forster, S., Gosch, L., Gräwe, U., Gründling-Pfaff, S., Haider, F., Ibenthal, M., Karow, N., Karsten, U., Kreuzburg, M., Lange, X., Leinweber, P., Massmann, G., Ptak, T., Rezanezhad, F., Rehder, G., Romoth, K., Schade, H., Schubert, H., Schulz-Vogt, H., Sokolova, I.M., Strehse, R., Unger, V., Westphal, J., Lennartz, B., 2018. Understanding the coastal ecocline: assessing sea–land interactions at non-tidal, low-lying coasts through interdisciplinary research. Front. Mar. Sci. 5, 1–22. https://doi.org/10.3389/fmars.2018.00342

Kleimeier, C., Rezanezhad, F., Van Cappellen, P., Lennartz, B., 2017. Influence of pore structure on solute transport in degraded and undegraded fen peat soils. Mires Peat 19, 1–9. https://doi.org/10.19189/MaP.2017.OMB.282

Koch, M., Koebsch, F., Hahn, J., Jurasinski, G., 2017. From meadow to shallow lake: Monitoring secondary succession in a coastal fen after rewetting by flooding based on aerial imagery and plot data. Mires Peat 19, 1–17. https://doi.org/10.19189/MaP.2015.OMB.188

Koebsch, F., Glatzel, S., Hofmann, J., Forbrich, I., Jurasinski, G., 2013a. CO<inf>2</inf> exchange of a temperate fen during the conversion from moderately rewetting to flooding. J. Geophys. Res. Biogeosciences 118, 940–950. https://doi.org/10.1002/jgrg.20069

Koebsch, F., Glatzel, S., Jurasinski, G., 2013b. Vegetation controls methane emissions in a coastal brackish fen. Wetl. Ecol. Manag. 21, 323–337. https://doi.org/10.1007/s11273-013-9304-8

Koebsch, F., Jurasinski, G., Koch, M., Hofmann, J., Glatzel, S., 2015. Controls for multi-scale temporal variation in ecosystem methane exchange during the growing season of a permanently inundated fen. Agric. For. Meteorol. 204, 94–105. https://doi.org/10.1016/j.agrformet.2015.02.002

Koebsch, F., Winkel, M., Liebner, S., Liu, B., Westphal, J., Schmiedinger, I., Spitzy,

A., Gehre, M., Jurasinski, G., Köhler, S., Unger, V., Koch, M., Sachs, T., Böttcher, M.E., 2019. Sulfate deprivation triggers high methane production in a disturbed and rewetted coastal peatland. Biogeosciences 16, 1937–1953. https://doi.org/10.5194/bg-16-1937-2019

Kolp, O., 1957. Die Nordöstliche Heide Mecklenburgs. Deutscher Verlag Der Wissenschaften, Berlin.

Kooi, H., Groen, J., 2001. Offshore continuation of coastal groundwater systems; predictions using sharp-interface approximations and variable-density flow modelling. J. Hydrol. 246, 19–35. https://doi.org/10.1016/S0022-1694(01)00354-7

Kopp, B.J., Fleckenstein, J.H., Roulet, N.T., Humphreys, E., Talbot, J., Blodau, C., 2013. Impact of long-term drainage on summer groundwater flow patterns in the Mer Bleue peatland, Ontario, Canada. Hydrol. Earth Syst. Sci. 17, 3485–3498. https://doi.org/10.5194/hess-17-3485-2013

Kreuzburg, M., Ibenthal, M., Janssen, M., Rehder, G., Voss, M., Naumann, M., Feldens, P., 2018. Sub-marine continuation of peat deposits from a coastal peatland in the southern Baltic Sea and its holocene development. Front. Earth Sci. 6. https://doi.org/10.3389/feart.2018.00103

Kreuzburg, M., Rezanezhad, F., Milojevic, T., Voss, M., Gosch, L., Liebner, S., Van Cappellen, P., Rehder, G. (submitted): Carbon release and transformation from coastal peat deposits controlled by submarine 1 groundwater discharge: A column experiment study

Krüger, K., 1995. Untersuchung zur Salzbeeinflussung überflutungsgefährdeter, forstlich genutzter Flächen im Naturschutzgebiet Hütelmoor-Heiligensee. Rostock.

LAiV MV Landesamt für innere Verwaltung Mecklenburg-Vorpommern, 2015.

Lamers, L.P.M., Tomassen, H.B.M., Roelofs, J.G.M., 1998. Sulfate-induced eutrophication and phytotoxicity in freshwater wetlands. Environ. Sci. Technol. 32, 199–205. https://doi.org/10.1021/es970362f

Lampe, R., 2002. Holocene Evolution of the South-Western Baltic Coast – Geological, Archaeological and Palaeo-environmental Aspects. Field meeting of INQUA Subcommission V Sea-level Changes and Coastal Evolution. Western Europe September 22 – 27, 2002, Greifswalder Geographische Arbeiten.

Lennartz, B., Liu, H., 2019. Hydraulic functions of peat soils and ecosystem service. Front. Environ. Sci. 7, 169–187. https://doi.org/10.3389/fenvs.2019.00092

Li, H., Boufadel, M.C., Weaver, J.W., 2008. Tide-induced seawater-groundwater circulation in shallow beach aquifers. J. Hydrol. 352, 211–224. https://doi.org/10.1016/j.jhydrol.2008.01.013

Limpens, J., Berendse, F., Blodau, C., Canadel, J.G., Freeman, C., Holden, J., Roulet, N., Rydin, H., Schaepman-Strub, G., 2008. Erratum: Peatlands and the carbon cycle: From local processes to global implications a synthesis (Biogeosciences, 5, 1475-1491, (2008)). Biogeosciences 5, 1739. https://doi.org/10.5194/bg-5-1739-2008

Loxham, M., 1980. Theoretical considerations of transport of pollutants in peats. Proc. 6th Int. Symp. Peatlands, Duluth, MN, USA.

Lucas, L.L., Unterweger, M.P., 2000. Comprehensive review and critical evaluation 105, 541–549.

LUNG (Landesamt für Umwelt, Naturschutz und Geologie), 2016. Tiefenlage der Grundwasseroberfläche in Mecklenburg-Vorpommern (Depth of the groundwater surface in Mecklenburg-Western Pomerania). Found online at https://www.umweltkarten.mv-regierung.de/atlas/script/index.php, last accessed 15/07/2019

Mamyrin, B.A., Tolstikhin, L.N., 1984. Developments in Geochemistry 3 - Helium Isotopes in Nature. Elsevier B.V.

McDonald, M.G., Harbaugh, A.W., 1988. A modular three-dimensional finite-difference ground-water flow model. https://doi.org/10.3133/twri06A1

Meyer, R., Engesgaard, P., Hinsby, K., Piotrowski, J.A., Sonnenborg, T.O., 2018. Estimation of effective porosity in large-scale groundwater models by combining particle tracking, auto-calibration and 14 C dating. Hydrol. Earth Syst. Sci. 22, 4843–4865. https://doi.org/10.5194/hess-22-4843-2018

Michael, H.A., Mulligan, A.E., Harvey, C.F., 2005. Seasonal oscillations in water exchange between aquifers and the coastal ocean. Nature 436, 1145–1148. https://doi.org/10.1038/nature03935

Miegel, K., Graeff, T., Selle, B., Salzmann, T., Franck, C., Bronstert, A., 2016. Untersuchung eines renaturierten Niedermoores an der mecklenburgischen Ostseeküste - Teil I: systembeschreibung und hydrologische Grundcharakterisierung (Investigation of a renatured fen on the Baltic Sea coast of Mecklenburg - Part I: system description . HyWa 60, 242–258.

Miegel, K., Gräff, T., Franck, C., Salzmann, T., Bronstert, A., Walther, M., Oswald, S.E., 2017. Auswirkungen des Sturmhochwassers der Ostsee am 4./5. Januar 2017 auf das renaturierte Niedermoor „Hütelmoor und Heiligensee“ an der deutschen Ostseeküste. HyWa 61, 232–243.

Moore, W.S., 2010. The effect of submarine groundwater discharge on the ocean. Ann. Rev. Mar. Sci. 2, 59–88. https://doi.org/10.1146/annurev-marine-120308-081019

Moore, W.S., 1999. The subterranean estuary: A reaction zone of ground water and sea water. Mar. Chem. 65, 111–125. https://doi.org/10.1016/S0304-4203(99)00014-6

Mulligan, A.E., Langevin, C., Post, V.E.A., 2011. Tidal boundary conditions in SEAWAT. Ground Water 49, 866–879. https://doi.org/10.1111/j.1745-6584.2010.00788.x

Niswonger, R.G., Prudic, D.E., 2006. Documentation of the Unsaturated-Zone Flow (UZF1) Package for modeling unsaturated flow between the land surface and the water table with MODFLOW-2005. https://doi.org/. Prudic, and R. Steven Regan https://doi.org/10.3133/tm6A19

Oke, T.R., 1978. Boundary Layer Climates. London: Methuem & Ltd. A.

Otto, J., Berveiller, D., Bréon, F.M., Delpierre, N., Geppert, G., Granier, A., Jans, W., Knohl, A., Kuusk, A., Longdoz, B., Moors, E., Mund, M., Pinty, B., Schelhaas, M.J., Luyssaert, S., 2014. Forest summer albedo is sensitive to species and thinning: How should we account for this in Earth system models? Biogeosciences 11, 2411–2427. https://doi.org/10.5194/bg-11-2411-2014

Ours, D.P., Siegel, D.I., Glaser, P.H., 1997. Chemical dilation and the dual porosity of humified bog peat. J. Hydrol. 196, 348–360. https://doi.org/10.1016/S0022-1694(96)03247-7

Penman, H.L., 1948. Natural evaporation from open water, hare soil and grass. Proc. R. Soc. Lond. A. Math. Phys. Sci. 193, 120–145. https://doi.org/10.1098/rspa.1948.0037

Pollock, D.W., 2016. User guide for MODPATH Version 7—A particle-tracking model for MODFLOW. https://doi.org/http://dx.doi.org/10.3133/ofr20161086

Portnoy, J.W., 1999. Salt marsh diking and restoration: Biogeochemical implications of altered wetland hydrology. Environ. Manage. 24, 111–120. https://doi.org/10.1007/s002679900219

Porubsky, W.P., Weston, N.B., Moore, W.S., Ruppel, C., Joye, S.B., 2014. Dynamics of submarine groundwater discharge and associated fluxes of dissolved nutrients, carbon, and trace gases to the coastal zone (Okatee River estuary, South Carolina). Geochim. Cosmochim. Acta 131, 81–97. https://doi.org/10.1016/j.gca.2013.12.030

Post, V., Kooi, H., Simmons, C., 2007. Using hydraulic head measurements in variable-density ground water flow analyses. Ground Water 45, 664–671. https://doi.org/10.1111/j.1745-6584.2007.00339.x

Post, V.E.A., Vandenbohede, A., Werner, A.D., Maimun, Teubner, M.D., 2013. Groundwater ages in coastal aquifers. Adv. Water Resour. 57, 1–11. https://doi.org/10.1016/j.advwatres.2013.03.011

Postma, D., Jakobsen, R., 1996. Redox zonation: Equilibrium constraints on the Fe(III)/SO4-reduction interface. Geochim. Cosmochim. Acta 60, 3169–3175. https://doi.org/10.1016/0016-7037(96)00156-1

Price, J.S., 1996. Hydrology and microclimate of a partly restored cutover bog, Quebec. Hydrol. Process. 10, 1263–1272. https://doi.org/10.1002/(SICI)1099-1085(199610)10:10<1263::AID-HYP458>3.0.CO;2-1

Price, J.S., Schlotzhauer, S.M., 1999. Importance of shrinkage and compression in determining water storage changes in peat: the case of a mined peatland. Hydrol. Process., 13: 2591-2601. doi:10.1002/(SICI)1099-1085(199911)13:16<2591::AID-HYP933>3.0.CO;2-E

Rau, G.C., Post, V.E.A., Shanafield, M., Krekeler, T., Banks, E.W., Blum, P., 2019. Error in hydraulic head and gradient time-series measurements: A quantitative appraisal. Hydrol. Earth Syst. Sci. 23, 3603–3629. https://doi.org/10.5194/hess-23-3603-2019

Reeve, A.S., Evensen, R., Glaser, P.H., Siegel, D.I., Rosenberry, D., 2006. Flow path oscillations in transient ground-water simulations of large peatland systems. J. Hydrol. 316, 313–324. https://doi.org/10.1016/j.jhydrol.2005.05.005

Reeve, A.S., Siegel, D.I., Glaser, P.H., 2001. Simulating dispersive mixing in large peatlands. J. Hydrol. 242, 103–114. https://doi.org/10.1016/S0022-1694(00)00386-3

Reeve, A.S., Siegel, D.I., Glaser, P.H., 2000. Simulating vertical flow in large peatlands. J. Hydrol. 227, 207–217. https://doi.org/10.1016/S0022-1694(99)00183-3

Reynolds, W.D., Brown, D.A., Mathur, S.P., Overend, R.P., 1992. Effect of in-situ gas accumulation on the hydraulic conductivity of peat. Soil Sci. 153, 397–408. https://doi.org/10.1097/00010694-199205000-00007

Robinson, C., Li, L., Barry, D.A., 2007a. Effect of tidal forcing on a subterranean estuary. Adv. Water Resour. 30, 851–865.

https://doi.org/10.1016/j.advwatres.2006.07.006

Robinson, C., Li, L., Prommer, H., 2007b. Tide-induced recirculation across the aquifer-ocean interface. Water Resour. Res. 43, 1–14. https://doi.org/10.1029/2006WR005679

Robinson, C.E., Xin, P., Santos, I.R., Charette, M.A., Li, L., Barry, D.A., 2018. Groundwater dynamics in subterranean estuaries of coastal unconfined aquifers: Controls on submarine groundwater discharge and chemical inputs to the ocean. Adv. Water Resour. 115, 315–331. https://doi.org/10.1016/j.advwatres.2017.10.041

Romanowicz, E.A., Siegel, D.I., Glaser, P.H., 1993. Hydraulic reversals and episodic methane emissions during drought cycles in mires. Geology 21, 231–234. https://doi.org/10.1130/0091-7613(1993)021<0231:HRAEME>2.3.CO;2

Röper, T., Greskowiak, J., Massmann, G., 2015. Instabilities of submarine groundwater discharge under tidal forcing. Limnol. Oceanogr. 60, 22–28. https://doi.org/10.1002/lno.10005

Rosenberry, D.O., Glaser, P.H., Siegel, D.I., Weeks, E.P., 2003. Use of hydraulic head to estimate volumetric gas content and ebullition flux in northern peatlands. Water Resour. Res. 39. https://doi.org/10.1029/2002WR001377

Russoniello, C.J., Fernandez, C., Bratton, J.F., Banaszak, J.F., Krantz, D.E., Andres, A.S., Konikow, L.F., Michael, H.A., 2013. Geologic effects on groundwater salinity and discharge into an estuary. J. Hydrol. 498, 1–12. https://doi.org/10.1016/j.jhydrol.2013.05.049

Schafmeister, M.T., Darsow, A., 2011. Potential change in groundwater discharge as response to varying climatic conditions – An experimental model study at catchment scale, in: Harff, J., Björck, S., Hoth, P. (Eds.), The Baltic Sea Basin, Central and Eastern European Development Studies (CEEDES). Springer Berlin Heidelberg, Berlin, Heidelberg, pp. 391–404. https://doi.org/10.1007/978-3-642-17220-5

Schlüter, M., Sauter, E.J., Andersen, C.E., Dahlgaard, H., Dando, P.R., 2004. Spatial distribution and budget for submarine groundwater discharge in Eckernförde Bay (Western Baltic Sea). Limnol. Oceanogr. 49, 157–167. https://doi.org/10.4319/lo.2004.49.1.0157

Schutte, C.A., Joye, S.B., Wilson, A.M., Evans, T., Moore, W.S., Casciotti, K., 2015. Global Biogeochemical Cycles sediment revealed by a nitrous oxide hot spot. Global Biogeochem. Cycles 1584–1598. https://doi.org/10.1002/2014GB005052

Schutte, C.A., Wilson, A.M., Evans, T., Moore, W.S., Joye, S.B., 2016. Methanotrophy controls groundwater methane export from a barrier island. Geochim. Cosmochim. Acta 179, 242–256. https://doi.org/10.1016/j.gca.2016.01.022

Selle, B., Graeff, T., Salzmann, T., Oswald, S.E., Walther, M., Miegel, K., 2016. Untersuchung eines renaturierten Niedermoores an der mecklenburgischen Ostseeküste - Teil II: salzdynamik und Wasserhaushalt (Investigation of a renatured fen catchment on the Baltic Sea coast of Mecklenburg - Part II: salt dynamics and water balance). HyWa 60, 259–268.

Siegel, D.I., 1983. Ground Water and the Evolution of Patterned Mires, Glacial Lake Agassiz Peatlands, Northern Minnesota. J. Ecol. 71, 913. https://doi.org/10.2307/2259601

Siegel, D.I., Chanton, J.R., Glaser, P.H., Chasar, L.S., Rosenberry, D.O., 2001. Estimating methane production rates in bogs and landfills by deuterium

enrichment of pore water. Global Biogeochem. Cycles 15, 967–975. https://doi.org/10.1029/2000GB001329

Siegel, D.I., Glaser, P.H., 1987. Groundwater Flow in a Bog-Fen Complex, Lost River Peatland, Northern Minnesota. J. Ecol. 75, 743. https://doi.org/10.2307/2260203

Smid, P., 1975. Evaporation from a Reedswamp. J. Ecol. 63, 299. https://doi.org/10.2307/2258856

Smith, A.J., 2004. Mixed convection and density-dependent seawater circulation in coastal aquifers. Water Resour. Res. 40, 169–187. https://doi.org/10.1029/2003WR002977

Solomon, D.K., Cook, P.G., 2000. 3H and 3He, in: Cook, P.G., Herczeg, A.L. (Eds.), Environmental Tracers in Subsurface Hydrology. Springer US, Boston, MA, pp. 397–424. https://doi.org/10.1007/978-1-4615-4557-6

Solomon, D.K., Hunt, A., Poreda, R.J., 1996. Source of radiogenic helium 4 in shallow aquifers: Implications for dating young groundwater. Water Resour. Res. 32, 1805–1813. https://doi.org/10.1029/96WR00600

Sterr, H., 2008. Assessment of vulnerability and adaptation to sea-level rise for the coastal zone of Germany. J. Coast. Res. 242, 380–393. https://doi.org/10.2112/07a-0011.1

Stoutjesdijk, P.H., Barkman, J.J., 2014. Microclimate, Vegetation and Fauna. KNNV Publishing. https://doi.org/10.1163/9789004297807

Succow, M., Joosten, H. (Eds.), 2001. Landschaftsökologische Moorkunde, 2nd ed. Schweizerbart Science Publishers, Stuttgart, Germany.

Sültenfuß, J., Roether, W., Rhein, M., 2009. The Bremen mass spectrometric facility for the measurement of helium isotopes, neon, and tritium in water. Isotopes Environ. Health Stud. 45, 83–95. https://doi.org/10.1080/10256010902871929

Sültenfuβ, J., Purtschert, R., Führböter, J.F., 2011. Age structure and recharge conditions of a coastal aquifer (northern Germany) investigated with 39Ar, 14C, 3H, He isotopes and Ne. Hydrogeol. J. 19, 221–236. https://doi.org/10.1007/s10040-010-0663-4

Sumner, M.E., 2000. Handbook of Soil Science. CRC Press.

Szymczycha, B., Vogler, S., Pempkowiak, J., 2012. Nutrient fluxes via submarine groundwater discharge to the Bay of Puck, southern Baltic Sea. Sci. Total Environ. 438, 86–93. https://doi.org/10.1016/j.scitotenv.2012.08.058

Tiemeyer, B., Pfaffner, N., Frank, S., Kaiser, K., Fiedler, S., 2017. Pore water velocity and ionic strength effects on DOC release from peat-sand mixtures: Results from laboratory and field experiments. Geoderma 296, 86–97. https://doi.org/10.1016/j.geoderma.2017.02.024

van Dijk, G., Smolders, A.J.P., Loeb, R., Bout, A., Roelofs, J.G.M., Lamers, L.P.M., 2015. Salinization of coastal freshwater wetlands; effects of constant versus fluctuating salinity on sediment biogeochemistry. Biogeochemistry 126, 71–84. https://doi.org/10.1007/s10533-015-0140-1

van Loon, A.H., Schot, P.P., Bierkens, M.F.P., Griffioen, J., Wassen, M.J., 2009. Local and regional impact of anthropogenic drainage on fen contiguity. Hydrol. Earth Syst. Sci. 13, 1837–1848. https://doi.org/10.5194/hess-13-1837-2009

van Wijk, W.R. and Ubing, D.S., 1963. Radiation. Physics of plant environment. North-Holland Pub. Co., Amsterdam, 62-101. Q. J. R. Meteorol. Soc.

https://doi.org/10.1002/qj.49709038628

Vasander, H., Tuittila, E.S., Lode, E., Lundin, L., Ilomets, M., Sallantaus, T., Heikkilä, R., Pitkänen, M.L., Laine, J., 2003. Status and restoration of peatlands in northern Europe. Wetl. Ecol. Manag. 11, 51–63. https://doi.org/doi.org/10.1023/A:1022061622602

Voigtländer, U., Schmidt, J., Scheller, W., 1996. Pflege-und Entwicklungsplan NSG Heiligensee und Hütelmoor.

Waddington, J.M., Roulet, N.T., 1997. Groundwater flow and dissolved carbon movement in a boreal peatland. J. Hydrol. 191, 122–138. https://doi.org/10.1016/S0022-1694(96)03075-2

Wassen, M.J., Joosten, H., 1996. In search of a hydrological explanation for vegetation changes along a fen gradient in the Biebrza Upper Basin (Poland). Vegetatio 124, 191–209.

Weiss, R.A.Y.F., 1971. Solubility of Helium and Neon in Water and Seawater 16, 235–241. https://doi.org/10.1021/je60049a019

Whiting, G.J., Chanton, J.P., 2001. Greenhouse carbon balance of wetlands: Methane emission versus carbon sequestration. Tellus, Ser. B Chem. Phys. Meteorol. 53, 521–528. https://doi.org/10.3402/tellusb.v53i5.16628

Whittington, P.N., Price, J.S., 2006. The effects of water table draw-down (as a surrogate for climate change) on the hydrology of a fen peatland, Canada. Hydrol. Process. 20, 3589–3600. https://doi.org/doi:10.1002/hyp.6376

Yihdego, Y., Becht, R., 2013. Simulation of lake–aquifer interaction at Lake Naivasha, Kenya using a three-dimensional flow model with the high conductivity technique and a DEM with bathymetry. J. Hydrol. 503, 111–122. https://doi.org/10.1016/j.jhydrol.2013.08.034

8 Appendix

8.1 Properties of groundwater observation wells

Table A 1 Properties of the groundwater observation wells at the study site 'Heiligensee and Hütelmoor'.

Measuring point	Observation well	Substrate	Filter depth (m a.s.l.)	Parameters measured	Installed since
MP1	1DS	Dune sand	0.50 to -0.50	P,T,EC*	Sep 2016
	1LS	Lower sand (aquifer)	-3.52 to -4.64	P,T,EC	Nov 2016
MP2	2DS	Dune sand	0.13 to -0.38	P,T,EC	Sep 2016
	2P	Peat	-1.14 to -2.14	P,T,EC	Sep 2016
	2LS	Lower sand (aquifer)	-3.00 to -4.20	P,T,EC	Nov 2016
MP3	3P	Peat	-0.13 to -0.63	P,T,EC	Sep 2016
	3LS	Lower sand (aquifer)	-1.12 to -2.25	P,T,EC	Jan 2017
MP6	6P	Peat	-0.41 to -1-41	P,T,EC	Sep 2016
	6LS	Lower sand (aquifer)	-2.57 to -3.70	P,T,EC	Jan 2017
MP7	7P	Peat	-0.21 to -0.59	P,T,EC	Sep 2016
	7LS	Lower sand (aquifer)	-1.57 to -2.70	P,T,EC	Jan 2017
MP8	8LS	Lower sand (aquifer)	3.15 to -2.85	P,T	Sep 2016
MP9	9LS	Lower sand (aquifer)	-0.20 to -2.28	P,T,EC	Sep 2016
MP10	10LS	Lower sand (aquifer)	-1.28 to -3.28	P,T	Sep 2016
Ditch upstream of ground sill	D_{out1}	Ditch	n.a.	P,T	Jan 2017#
Ditch downstream of ground sill	D_{out2}	Ditch	n.a.	P,T	Jan 2017
Ditch central peatland near MP6	D_{ctr}	Ditch	n.a.	P,T,EC	Mar 2017

*P: pressure, T: temperature, EC: electrical conductivity, # no data between May 2017 and Apr 2018

8.2 Chemical parameters of groundwater samples

Table A 2 Concentrations of ions, DIC, DOC, tritium and tritiogenic helium at the study site 'Heiligensee and Hütelmoor'.

		MP1			MP2			MP6		MP7		MP9	MP10	Baltic
	Date#	1US	1LS	2US	2P	2LS	6P	6LS	7SW	7P	7LS	9LS	10LS	
EC* (mS/cm)	a	3.4	12.8	1.8	4.7	6.1		6.9		7.2	8.1	0.7	0.5	
	b	2.5	13.7	0.5	4.4	6.6	8.0	7.5	0.6	8.7	8.9	0.6	0.4	19.2
pH*	a	6.64	6.81	6.25	6.67	6.72		6.5		6.25	6.3	6.9	5.96	
	b	6.41	6.61	6.14	6.29	6.34		6.2	6.8	6.01	5.94	6.45	5.61	
Cl^- (mg/L)	a	799	3822	455	1361	1715		2075		1392	1696	40	92	
	b	455	3966	95	1421	1823	2017	2208	102	1551	1850	41	61	6339
SO_4^{2-} (mg/L)	a	<1	<1	<1	10	21		188		1745	2216	49	76	
	b	<1			67	<1	1051	231	11	2063	2189	60	47	1011
Br^- (mg/L)	a	4.0	21.4	1.8	7.4	8.1		4.8		<1	<1	<0.1	<0.1	
Mg^{2+} (mg/L)	a	35.7	281	31.4	97.8	125		229		237	230	9.8	18.3	
	b	30.9	276	7.4	90	87.6	206	132	10.5	233	213	9.2	10.5	384
Ca^{2+} (mg/L)	a	144	176	56	46	231		219		446	433	99	27	
	b	146	200	13	42	166	141	126	29	449	472	97	15	151
Na^+ (mg/L)	a	406	2117	338	968	1362		1723		938	976	30	50	
	b	259	2107	65	785	956	1092	1038	57	876	901	27	37	3164
K^+ (mg/L)	a	14.5	58.8	18.2	34.2	33.3		35,0		15,0	20.3	1.1	6.2	
	b	12.9	57.9	10.1	30.7	35.6	56.9	40.9	3.0	20.6	20.7	1.0	4.5	130
Fe^{2+} (mg/L)	b	3.31	5.45		0.25	0.16	0.46	0.40	1.35	115.75	103.66		0.73	
DIC (mg/L)	b	139.76	330.20	22.86	96.39	167.38	58.61	76.74	19.13	21.67	44.95		8.18	18.20
DOC (mg/L)	b	31.82	11.70	74.38	81.19	63.35	140.42	40.72	46.85	164.39	36.10		30.91	11.74
PO_4^{3-} (mg/L)	b	0.249	0.110	2.976	0.711	0.701	3.659	0.506	0.481	3.761			0.118	0.010
NH_4^+ (mg/L)	a	<1	<1	<1	14.35	<1		<1		58.8	34.1	<1	<1	
	b	<1	<1	1.01	12.7	15.1	33.3	17.8	<1	41.7	24.8	<1	<1	<1
Tritium (TU)	c		6.55			0.36		2.71			4.32	6.01		
$^3He_{trit}$ (TU)	c		2.03			0.00		58.80			2.00	25.15		

*values measured in-situ; #samples taken on (a) 22/08/2017, (b) 30/04/2018, (c) 07/02/2017

8.3 Drilling data

Table A 3 Drilling data and location from Dahms 1991, Krüger 1995, the LUNG database ("lg" and "Hy"), and own drilling, in [m a.s.l.].

Drilling ID	x	y	ground level	Beach/dune		peat surface	peat base	aquifer surface	aquifer base/till surface
				Surface	Base				
Krüger 42	315336	6011226	0.1			0.1	-2.4	-2.4	
Krüger 43	315532	6011155	-0.1			-0.1	-2.65	-2.65	
Krüger 27	315678	6010998	0			0	-1.75	-1.75	
Krüger 26	315735	6011174	0			0	-1.7	-1.7	
Krüger 25	315799	6011363	0			0	-1.8	-1.8	
Krüger 24	315863	6011553	0			0	-0.4	-0.4	
Krüger 23	315929	6011743	0.1			0.1	-0.15	-0.15	
Krüger 22	315992	6011930	0.1			0.1	-0.5	-0.5	
Krüger 35	315807	6011698	0.1			0.1	-0.6	-0.6	
Krüger 36	315999	6011629	0.2			0.2	-0.5	-0.5	
Krüger 37	316185	6011558	0.2			0.2	-0.25	-0.25	
Krüger 34	315619	6011767	0			0	-1.6	-1.6	
Krüger 38	316376	6011492	0.2			0.2	-0.05	-0.05	
Krüger 39	316559	6011420	2.1			2.1	1.85	1.85	
Krüger 28	315635	6012183	0.3			0.3	-1.65	-1.65	
Krüger 29	315909	6012087	0.1			0.1	-1.3	-1.3	
Krüger 30	316098	6012022	0.1			0.1	-0.5	-0.5	
Krüger 31	316282	6011954	0.1			0.1	-0.3	-0.3	
Krüger 32	316474	6011884	1.3			1.3	1.05	1.05	
Krüger 41	315223	6011267	0.8	0.8	0.5	0.5	-2.8	-2.8	
Krüger 50	314949.4	6010810	0.8	0.8	0.6	0.6	-2.45	-2.45	
Krüger 44	316288.2	6010851	-0.1			-0.1	-0.4	-0.4	
Krüger 45	316531	6010746	0.1			0.1	-0.2	-0.2	
Krüger 49	314600.2	6010319	0.5	0.5	0.05	0.05	-1	-1	
Krüger 53	315643.7	6010691	0.6	0.6	0.3	0.3	-0.65	-0.65	
Dahms 1	314910.69	6010520.5	0.3			0.3	-1.4	-1.4	
Dahms 2	314980.54	6010482.4	0.32			0.32	-1.18	-1.18	
Dahms 3	315073.674	6010440.07	0.24			0.24	-1.06	-1.06	
Dahms 4	315155.166	6010436.89	0.29			0.29	-1.31	-1.31	
Dahms 5	315248.299	6010422.08	0.34			0.34	-1.56	-1.56	
Dahms 6	315256.766	6010389.27	0.3			0.3	-0.9	-0.9	
Dahms 7	315231.366	6010353.28	0.14			0.14	-1.16	-1.16	
Dahms 8	315334.024	6010211.47	0.29			0.29	-0.91	-0.91	
Dahms 9	315418.691	6010193.47	0.34			0.34	-0.96	-0.96	
Dahms 10	315510.766	6010186.07	0.34			0.34	-0.46	-0.46	

Dahms 11	315580.616	6010208.29	0.32			0.32	-0.98	-0.98	
Dahms 12	315698.092	6010248.51	0.32			0.32	-0.18	-0.18	
Dahms 13	315828.002	6010322.5	0.52			0.52	-0.08	-0.08	
Dahms 14	316013.74	6010386.8	0.44			0.44	-0.06	-0.06	
Dahms 15	315943.096	6010506.65	0.54			0.54	0.04	0.04	
Dahms 16	315865.309	6010576.5	0.55			0.55	-0.05	-0.05	
Dahms 17	315781.965	6010620.16	0.54			0.54	0.04	0.04	
Dahms 18	315670.839	6010659.85	0.55			0.55	-0.45	-0.45	
Dahms 19	315604.958	6010673.34	0.64			0.64	-0.76	-0.76	
Dahms 20	315620.965	6010766.96	0.56			0.56	-0.74	-0.74	
Dahms 21	315623.611	6010833.64	0.35			0.35	-0.75	-0.75	
Dahms 22	315563.815	6010765.9	0.59			0.59	-0.81	-0.81	
Dahms 23	315512.486	6010792.36	0.55			0.55	-0.65	-0.65	
Dahms 24	315531.47	6010879.67	0.32			0.32	-0.18	-0.18	
Dahms 25	315426.615	6010897.17	0.34			0.34	-0.96	-0.96	
Dahms 26	315408.094	6010812.5	0.34			0.34	-0.46	-0.46	
Dahms 27	315312.315	6010830.49	0.44			0.44	-0.56	-0.56	
Dahms 28	315191.665	6010828.9	0.34			0.34	-1.66	-1.66	
Dahms 29	315142.452	6010786.04	0.32			0.32	-1.78	-1.78	
Dahms 30	315032.482	6010768.22	0.34			0.34	-1.86	-1.86	
Dahms 31	314985.519	6010687.52	0.34			0.34	-1.96	-1.96	
Dahms 32	314978.243	6010588.96	0.32			0.32	-1.68	-1.68	
Dahms 33	315157.201	6010539.61	0.44			0.44	-1.66	-1.66	
Dahms 34	315261.711	6010577.97	0.44			0.44	-1.56	-1.56	
Dahms 35	315376.805	6010652.72	0.74			0.74	-1.26	-1.26	
Dahms 36	315517.035	6010667.93	0.74			0.74	-1.16	-1.16	
Dahms 37	315469.41	6010529.68	0.79			0.79	-0.71	-0.71	
Dahms 38	315375.482	6010491.32	0.54			0.54	-1.16	-1.16	
Dahms 39	315347.198	6010312.22	0.34			0.34	-1.16	-1.16	
Dahms 40	315442.449	6010353.5	0.56			0.56	-1.14	-1.14	
Dahms 41	315618.132	6010358.79	0.76			0.76	-0.24	-0.24	
Dahms 42	315629.774	6010461.45	0.73			0.73	-0.27	-0.27	
Dahms 43	315578.974	6010581.04	0.64			0.64	-0.56	-0.56	
Dahms 44	315780.058	6010519.66	0.64			0.64	-0.26	-0.26	
Dahms 45	315838.636	6010422.18	0.59			0.59	0.09	0.09	
Dahms 46	315722.749	6010333.28	0.59			0.59	-0.01	-0.01	
Beach probing 1	315889.642	6012509.95	0.5576			0.5576	-0.162	-0.1624	
Beach probing 2	315874.845	6012494.1	0.5451			0.5451	-0.429	-0.4299	
Beach probing 3	315854.09	6012468.29	0.518			0.518	-0.757	-0.757	
Beach probing 4	315826.932	6012420.39	0.5464			0.5464	-0.878	-0.8786	
Beach probing 5	315804.853	6012357.12	0.4959			0.4959	-0.949	-0.9491	

Beach probing 6	315601.599	6012104.32	0.3472			0.3472	-1.348	-1.3478	
Beach probing 7	315572.927	6012059.63	0.391			0.391	-1.624	-1.624	
Beach probing 8	315529.78	6011957.34	0.4692			0.4692	-1.126	-1.1258	
Beach probing 9	315458.123	6011889.52	0.3814			0.3814	-1.134	-1.1336	
Beach probing 10	315400.757	6011781.95	0.487			0.487	-0.338	-0.338	
Beach probing 11	315281.15	6011586.88	0.5726			0.5726	-1.422	-1.4224	
Beach probing 12	315253.552	6011703.91	-0.636			-0.636	-1.311	-1.311	
Beach probing 13	315249.519	6011706.51	-0.7184			-0.7184	-0.923	-0.9234	
Beach probing 14	315265.187	6011730.96	-0.7594			-0.7594	-1.259	-1.2594	
Beach probing 15	315291.154	6011774.65	-0.7759			-0.7759	-1.2709	-1.2709	
Beach probing 16	315288.426	6011778.99	-0.955			-0.955	-1.15	-1.15	
Beach probing 17	315319.228	6011821.23	-0.6858			-0.6858	-1.0058	-1.0058	
Beach probing 18	315317.647	6011827.78	-0.8266			-0.8266	-1.0366	-1.0366	
Beach probing 19	315357.376	6011876.4	-0.5674			-0.5674	-1.7924	-1.7924	
Beach probing 20	315389.537	6011939.88	-0.6637			-0.6637	-2.0987	-2.0987	
Beach probing 21	315393.712	6011946.97	-0.8063			-0.8063	-1.3713	-1.3713	
Beach probing 22	315457.545	6012041.76	-0.6669			-0.6669	-1.3419	-1.3419	
Beach probing 23	315489.471	6012063.81	-0.2675			-0.2675	-0.6125	-0.6125	
Beach probing 24	315648.401	6012325.21	-0.3451			-0.3451	-0.9951	-0.9951	
Peatland probing 1	316277	6011207	0.29			0.29	-0.406	-0.406	
Peatland probing 2	316208	6011180	0.27			0.27	-0.905	-0.905	
Peatland probing 3	316073	6011138	0.24			0.24	-1.355	-1.355	
Peatland probing 4	316012	6011130	0.04			0.04	-1.365	-1.365	
Peatland probing 5	315885	6011089	0.04			0.04	-1.195	-1.195	
Peatland probing 6	315808	6011065	0.14			0.14	-1.78	-1.78	
Peatland probing 7	315731	6011089	-0.06			-0.06	-1.985	-1.985	
Peatland probing 8	315683	6011024	0.14			0.14	-1.815	-1.815	
Peatland probing 9	315711	6011153	-0.06			-0.06	-1.78	-1.78	
Peatland probing 10	316128.285	6010893.39	0.228			0.228	-1.063	-1.063	
Peatland probing 11	316413.51	6010683.5	0.128			0.128	-0.432	-0.432	

Peatland probing 12	316470.733	6010659.2	0.145			0.145	-0.545	-0.545	
Peatland probing 13	316514.682	6010643.66	0.574			0.574	0.294	0.294	
Peatland probing 14	316356.8	6010726.3	0.2			0.2	-0.62	-0.62	
Peatland probing 15	316219.591	6010656.01	0.007			0.007	-0.818	-0.818	
Peatland probing 16	316275.976	6010629.8	-0.135			-0.135	-1.095	-1.095	
Peatland probing 17	316156.21	6010601.6	0.102			0.102	-0.613	-0.613	
Peatland probing 18	316230.84	6010508.33	0.133			0.133	-0.497	-0.497	
Peatland probing 19	316121.469	6010462.71	0.249			0.249	-0.691	-0.691	
Peatland probing 20	316084.118	6010472.28	0.3			0.3	-0.471	-0.471	
Peatland probing 21	316187.133	6010380.3	0.068			0.068	-0.402	-0.402	
Peatland probing 22	316056.073	6010280.56	0.113			0.113	-0.292	-0.292	
Peatland probing 23	315886.723	6010270.62	0.494			0.494	0.109	0.109	
Peatland probing 24	316351.352	6010883.79	0.077			0.077	-0.538	-0.538	
Peatland probing 25	316435.159	6010845.91	0.014			0.014	-0.401	-0.401	
Peatland probing 26	316408.384	6010981.11	0.08			0.08	-0.46	-0.46	
Peatland probing 27	316503.811	6010922.67	0.19			0.19	-0.26	-0.26	
Peatland probing 28	316490.601	6011062.98	0.217			0.217	-0.133	-0.133	
Peatland probing 29	316531.947	6011041.89	0.476			0.476	0.001	0.001	
Peatland probing 30	316393.245	6011247.45	0.39			0.39	0.005	0.005	
Peatland probing 31	316368.95	6010296.32	0.567			0.567	0.117	0.117	
Peatland probing 32	315110.219	6010211.87	0.263			0.263	-0.077	-0.077	
Peatland probing 33	315095.399	6010283.9	0.109			0.109	-0.416	-0.416	
Peatland probing 34	315345.59	6010193.17	0.25			0.25	-0.73	-0.73	
Peatland probing 35	315315.249	6010173.68	0.3			0.3	-0.3	-0.3	
Peatland probing 36	315487.818	6010124.81	0.38			0.38	-0.507	-0.507	
Peatland probing 37	314908.762	6010208.06	0.006			0.006	-0.874	-0.874	
Peatland probing 38	314662.338	6010120.76	0.28			0.28	-0.265	-0.265	
Peatland probing 39	314624.206	6010009.88	0.508			0.508	0.028	0.028	
Peatland probing 40	314505.641	6010054.79	0.295			0.295	-0.19	-0.19	
B1	315711.398	6012315.92	0.5689	0.5689	-0.8111	-0.8111	-1.72	-1.72	-6
B2	315755.632	6012289.73	0.543	0.543	-1.117	-1.117	-2.137	-2.137	-4.457

B3	315677.59	6012348.36	0.2015	0.2015	-1.1185	-1.1185	-2.55	-2.55	-5
B4	315457.418	6012009.66	-0.1072			-0.1072	-1.5602	-1.5602	-6.12
B6	315023.781	6011299.3	0.2	0.2	-2.28	-2.28	-3.12	-3.12	-9
B5	315340.528	6011834.61	0.2354	0.2354	-0.1496	-0.1496	-0.645	-0.645	-3.375
B7	314611.329	6010571.7	0.2	0.2	-3.1	-3.1	-3.0035	-3.0035	-7.5
B9	315175.062	6011539.73	0.4211	0.4211	-1.5689	-1.5689	-2.9439	-2.9439	-14
MP2	315104.241	6011266.88	0.74	0.74	-0.7	-0.7	-2.93	-2.93	-8.9
MP3	314689.738	6010523.9	0.9155	0.9155	0.216	0.216	-0.8145	-0.8145	-6
MP6	315631.79	6011017.47	0.322			0.322	-1.91	-1.91	-7
MP7	316265.595	6010788.19	0.1555			0.1555	-0.745	-0.745	-5
way 7	316318	6010755	0.25			0.25	-0.3	-0.3	-4.7
B8	314799.594	6010871.63	0.658	0.658	-2.842	-2.842	-2.952	-2.952	-5.48
MP8	316794.41	6011913.75	3.554					3.55	-8
MP9	316746.459	6010555.68	1.7					1.7	-5.4
MP10	315556.959	6009991.6	1.92					1.92	-4.58
Ig GrMz 5/956	316152	6012149							
Hy GrMz 2/975	319242	6013376	2.7					2.7	-8.3
Hy GrMz 1/975	318165	6013702	5					5	-6
Ig Fsb-/956 (4)	314979	6010804	0.4			0.4	-1.3	-1.3	-2.3
Ig Fsb-/956 (3)	314549	6010342	0.4	0.4	-0.25	-0.25	-1.1	-1.1	-8.5
Ig GrMz 43/962	316338	6009575	2.52					2.52	-1.78
Ig Fsb-/956 (2)	314474	6009985	0.4			0.4	-0.2	-0.2	-3.9
Ig RU 138/979	314438	6009731	2.4					2.4	-4.8
Hy Fsb 21c/914	314010	6009434	1.5					1.5	-3
Hy RU 4/979	315157	6008635	1					1	-2
Ig RU 208/962	316122	6008494	3.4					3.4	0.6
Ig BwhR 28/956	315656	6008584	1.2					1.2	-1.65
Hy RU II/928	314402	6008767	1.2					1.2	-3.5
Hy RU 4/930	313834	6008831	2.1					2.1	-4.9
Ig GrMz 4/956	315319	6011250	0.5			0.5	-2.6	-2.6	-8.2
HyGrMz-951	316714	6011474	2					2	-14.3

8.4 Slug Test Analysis

Table A 4: Input parameters for the KGS-model in the software AQTESOLV

Well	h static water level [m a.s.l.l	Well depth [m a.s.l.]	Slug length in water [m]	H(0) [m] initial change	H [m] water column height [m]	b [m] aquifer thickness	b [m] (confined)	anisotropy ratio	d [m] well screen depth from static water level
MP 1 LS	0.32	-4.14	1.06	0.68	4.46	5.82	4	1	3.34
MP 1 US	0.58	-0.60	0.49	0.31	1.18	1.49	1.38	1	0.26
MP2 LS	0.09	-4.21	1.06	0.68	4.30	9.00	5.85	1	3.17
MP 2 P	0.33	-2.05	1.06	0.68	2.38	3.39	2.36	1	1.46
MP 2 US	0.54	-0.31	0.41	0.26	0.84	1.20	1.44	1	0.34
MP 3 LS	0.22	-2.25	1.06	0.68	2.47	5.38	4.3	1	1.34
MP 3 P	0.25	-1.59	1.06	0.68	1.84	1.10	1.00	1	1.34
MP 6 LS	0.46	-3.67	1.06	0.68	4.14	8.14	6.00	1	3.01
MP 6 P	0.42	-1.39	1.06	0.68	1.82	2.40	2.00	1	0.90
MP 7 LS	0.49	-2.71	1.06	0.68	3.19	5.75	4.52	1	2.065
MP 7 P	0.41	-0.59	0.35	0.22	1.00	1.17	0.90	1	0.615
MP 8	1.89	-2.86	1.06	0.68	4.75	9.34	11.00	1	-0.85
MP 9	1.37	-2.21	1.06	0.68	3.58	7.00	7.40	1	1.5
MP 10	0.67	-3.28	1.06	0.68	3.95	5.20	6.48	1	2.11

Well	L [m] length of well screen	transducer depth [m a.s.l.]	r (c) [m] inside radius well of casing	r (w) [m] radius of well	r_{sk} [m] outer radius of well skin	Ground surface [m a.s.l.]	Aquifer bottom [m a.s.l.[	Aquifer top [m a.s.l.]
MP 1 LS	1.125	3.25	0.025	0.025	0.03	0.50	-5.50	-1.50
MP 1 US	0.92	1.05	0.025	0.025	0.03	0.47	-0.91	0.47
MP2 LS	1.125	1.16	0.025	0.025	0.03	0.74	-8.91	-3.06
MP 2 P	0.92	1.75	0.025	0.025	0.03	0.74	-3.06	-0.70
MP 2 US	0.50	0.81	0.025	0.025	0.03	0.78	-0.66	0.78
MP 3 LS	1.125	2.29	0.025	0.025	0.03	0.84	-5.16	-0.86
MP 3 P	0.5		0.025	0.025	0.03	0.85	-0.85	0.15
MP 6 LS	1.125	2.94	0.025	0.025	0.03	0.32	-7.68	-1.68
MP 6 P	0.92	1.69	0.025	0.025	0.03	0.02	-1.98	0.02
MP 7 LS	1.125	3.01	0.025	0.025	0.03	0.24	-5.26	-0.74
MP 7 P	0.38	0.93	0.025	0.025	0.03	0.14	-0.76	0.14
MP 8	5.60	2.62	0.025	0.025	0.03	3.56	-7.45	3.56
MP 9	2.08	2.38	0.025	0.025	0.03	1.77	-5.63	1.77
MP 10	1.84	3.322	0.025	0.025	0.03	1.95	-4.53	1.95

1LS Falling Head KGS:

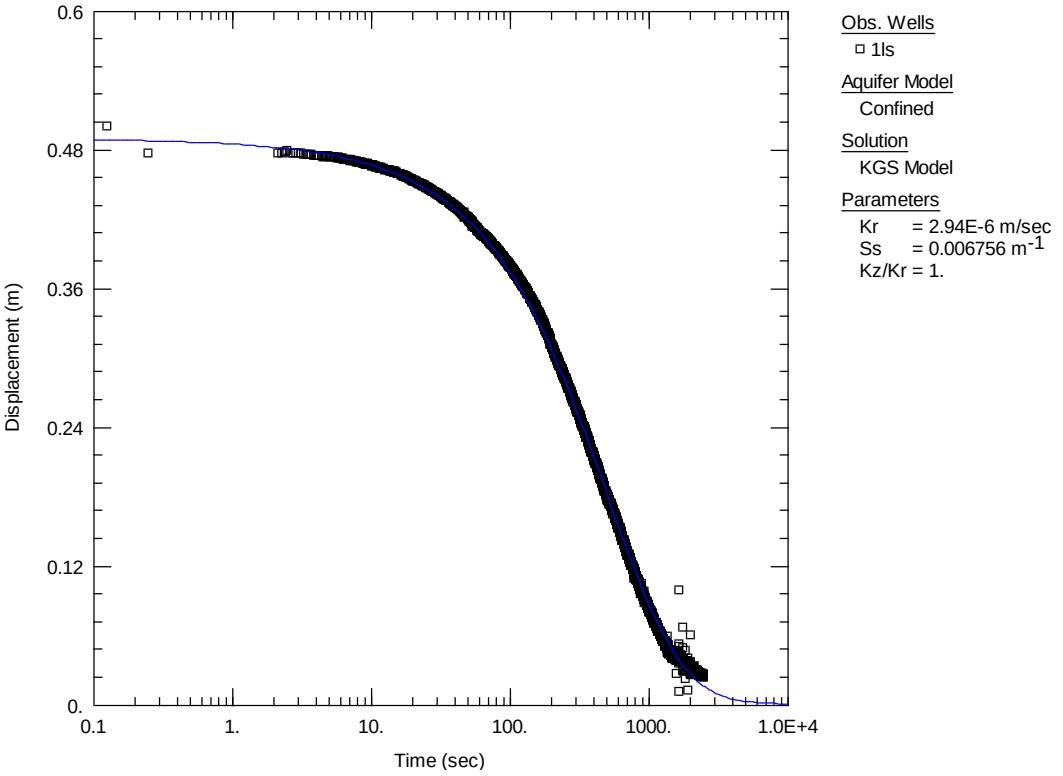

1LS Falling Head KGS wellbore skin:

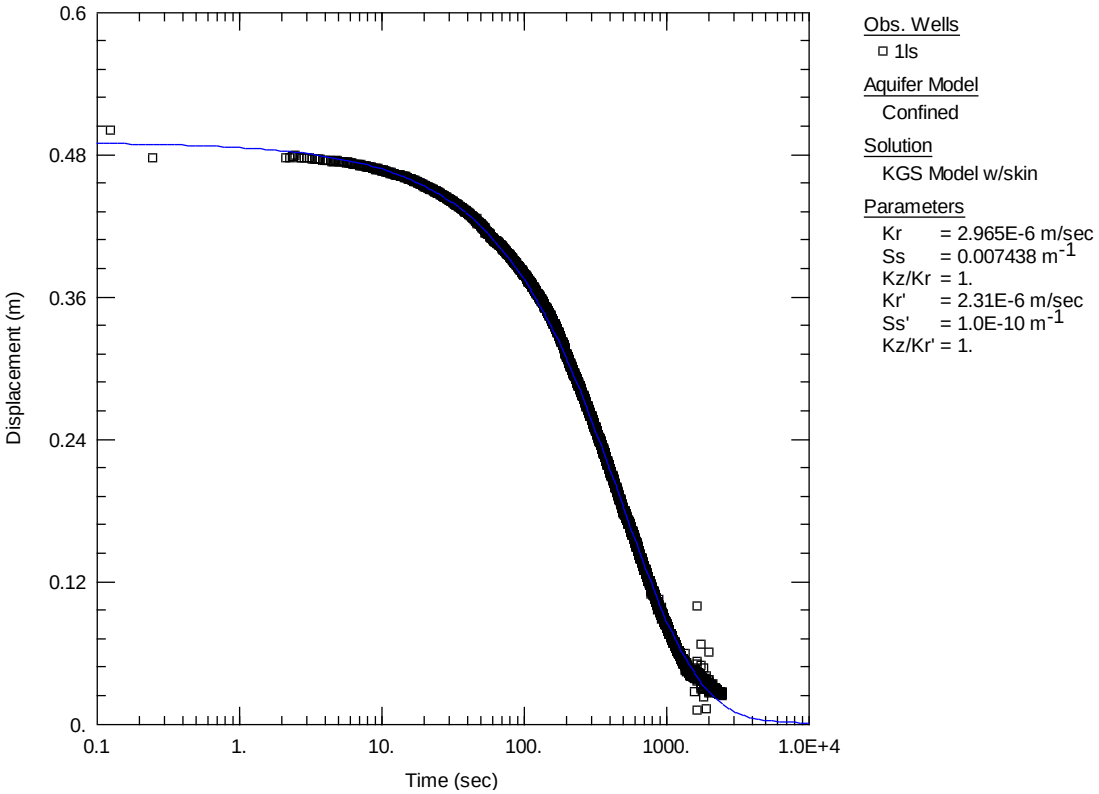

1LS Rising Head KGS:

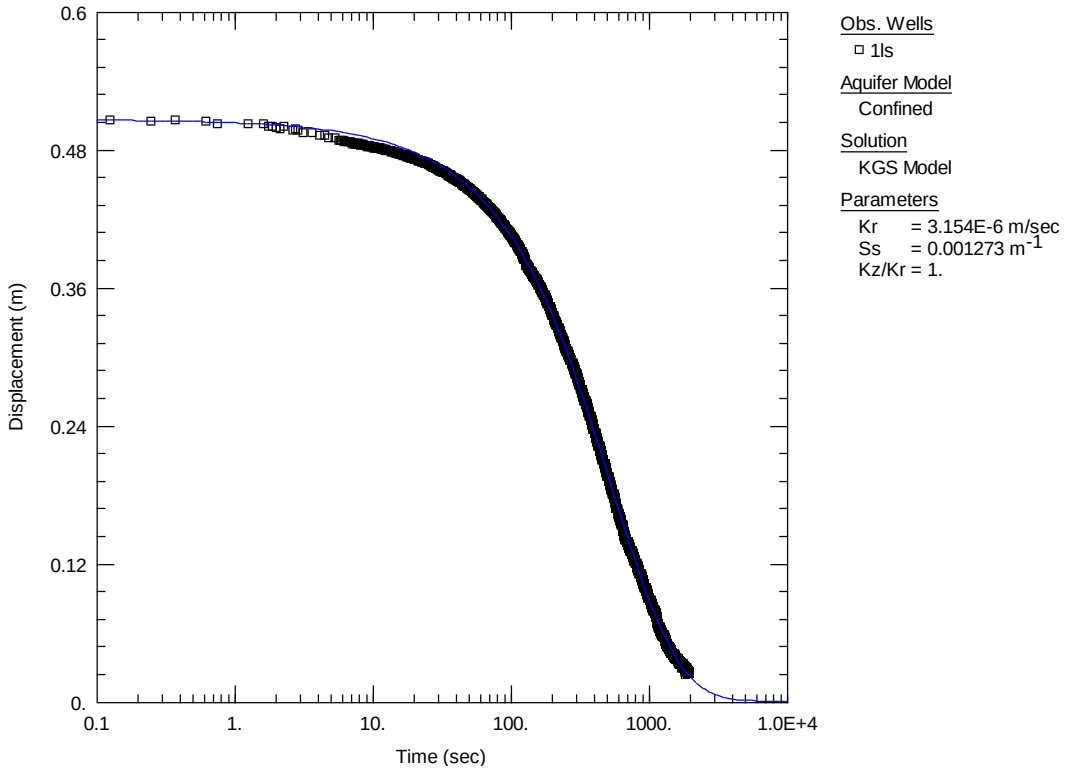

1LS Rising Head KGS wellbore skin:

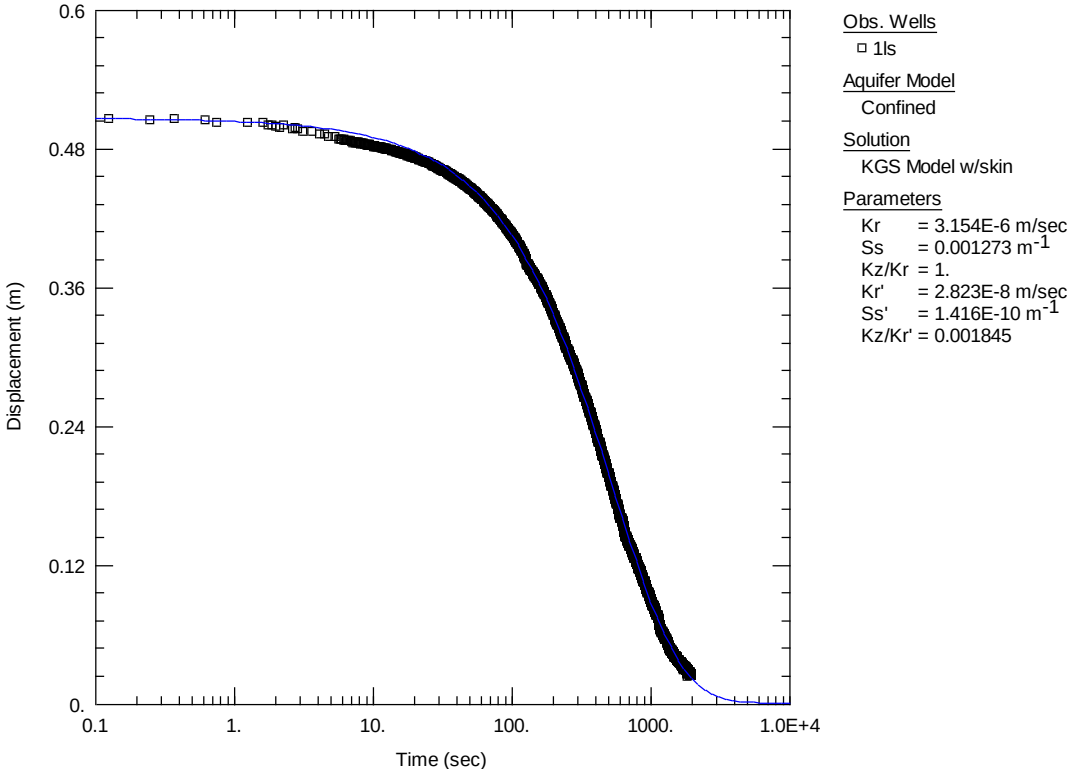

1US Falling head:

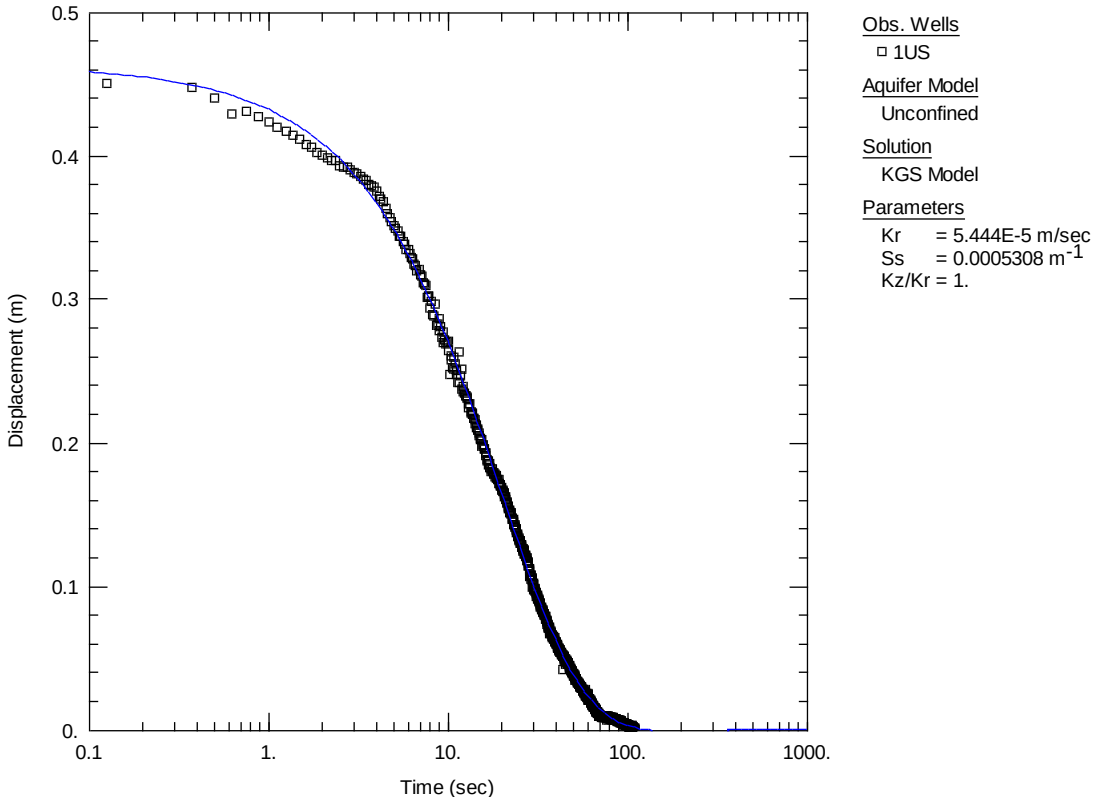

1US Falling head with wellbore skin:

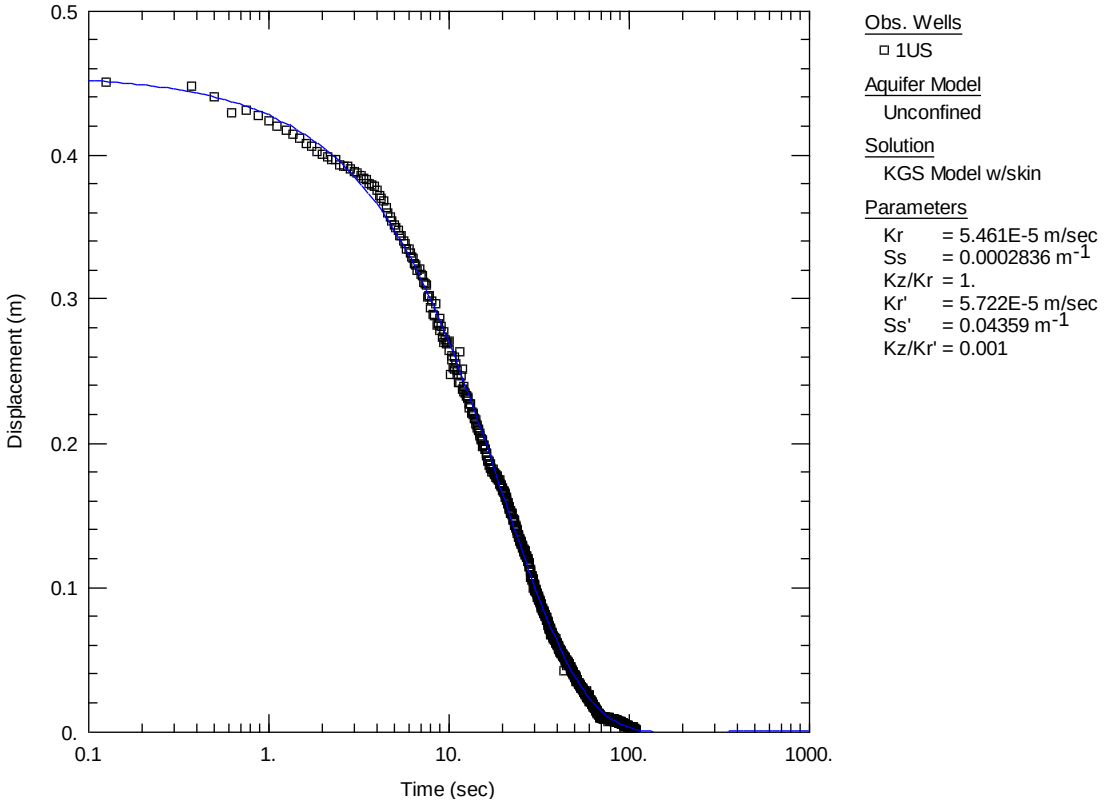

1US Rising head:

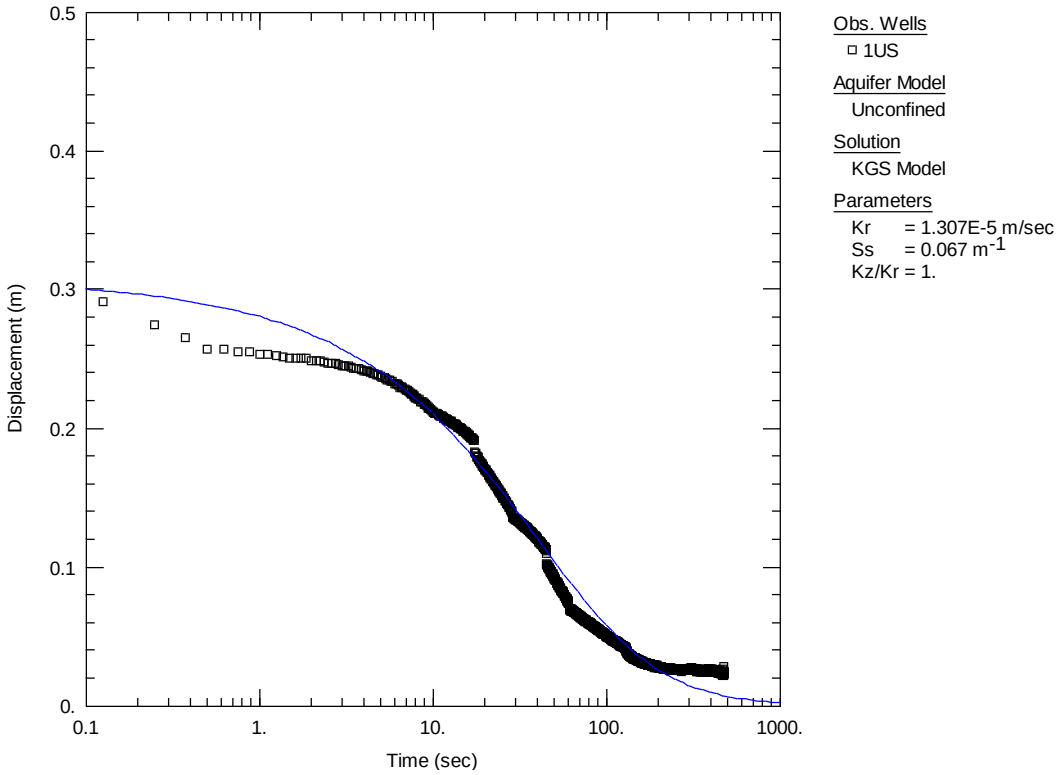

1US Rising head with wellbore skin:

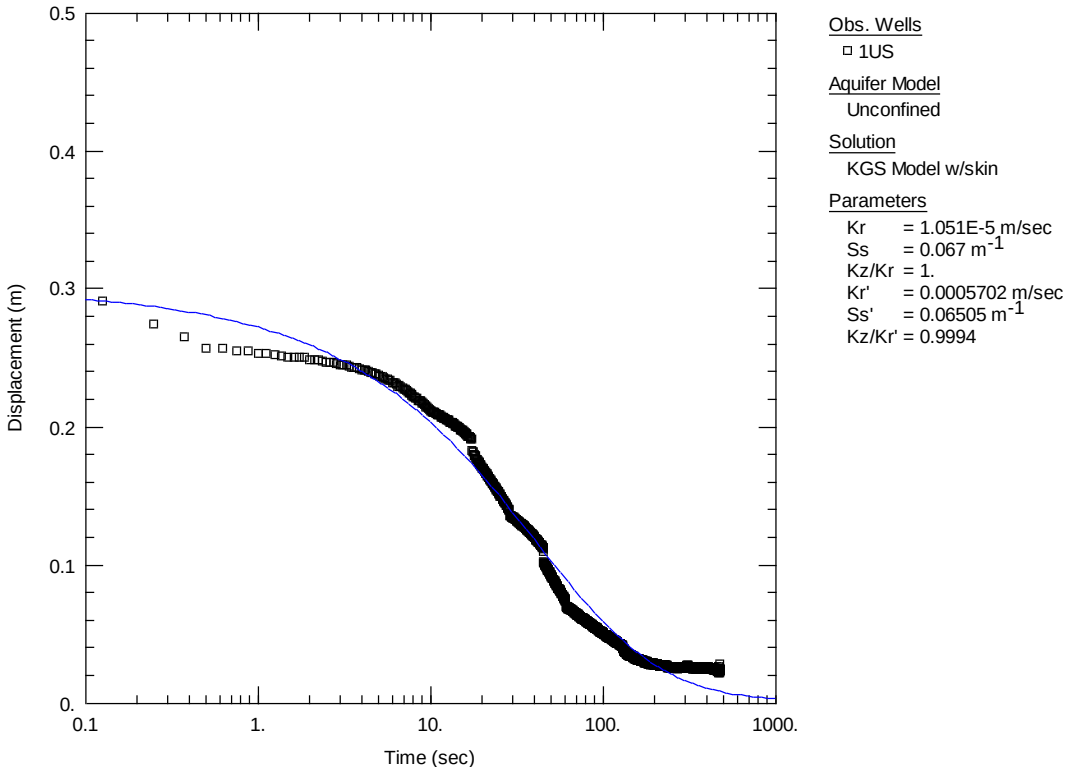

2LS Falling head:

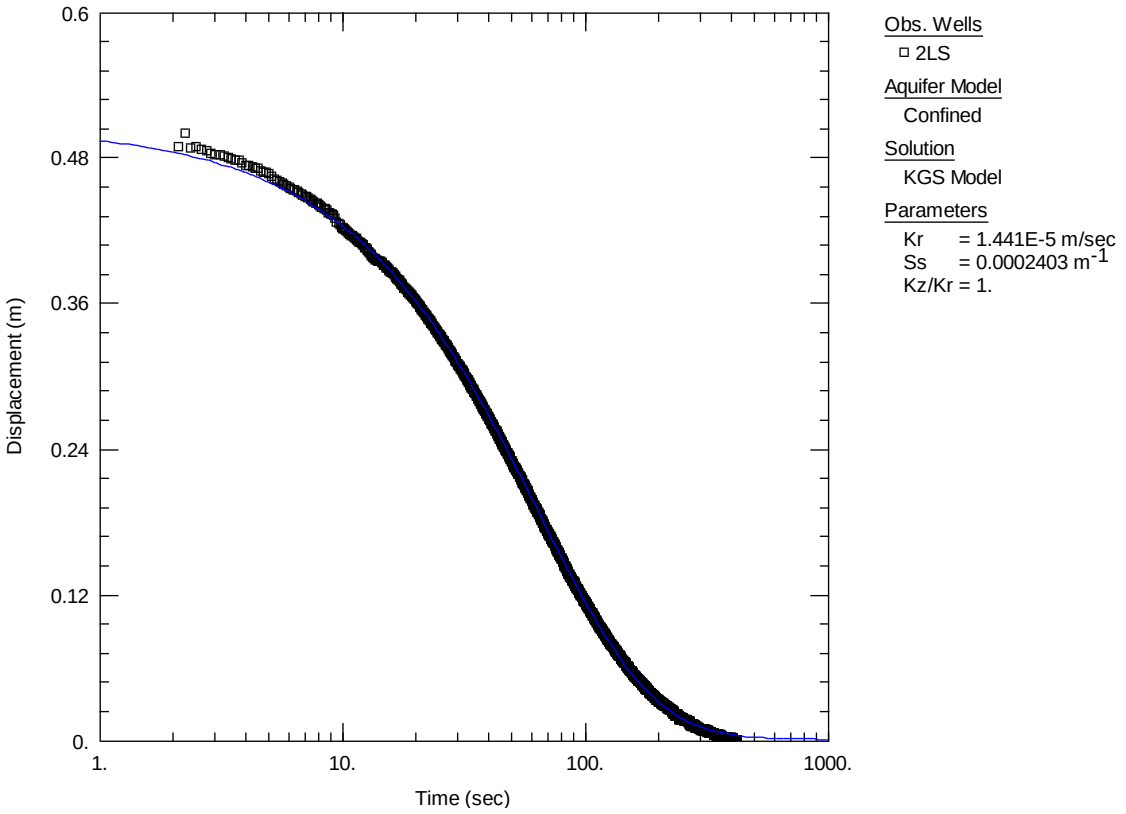

2LS Falling head with wellbore skin (convergence criteria not fulfilled):

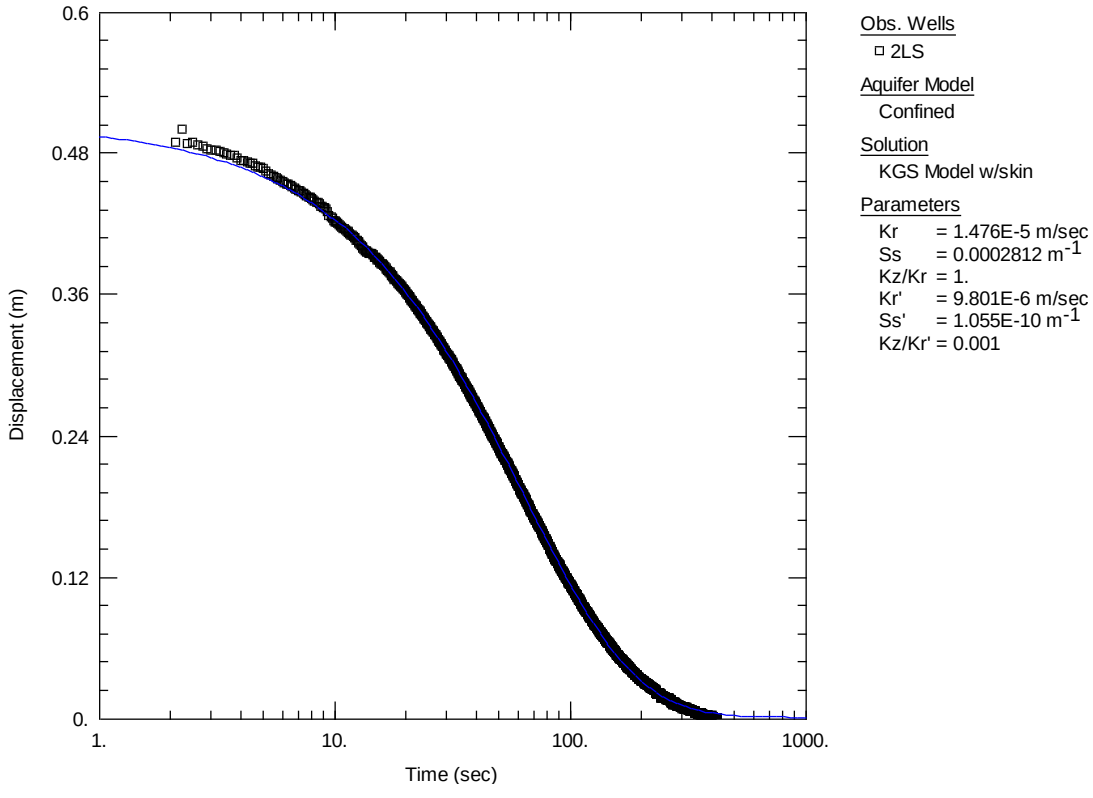

2LS Rising head:

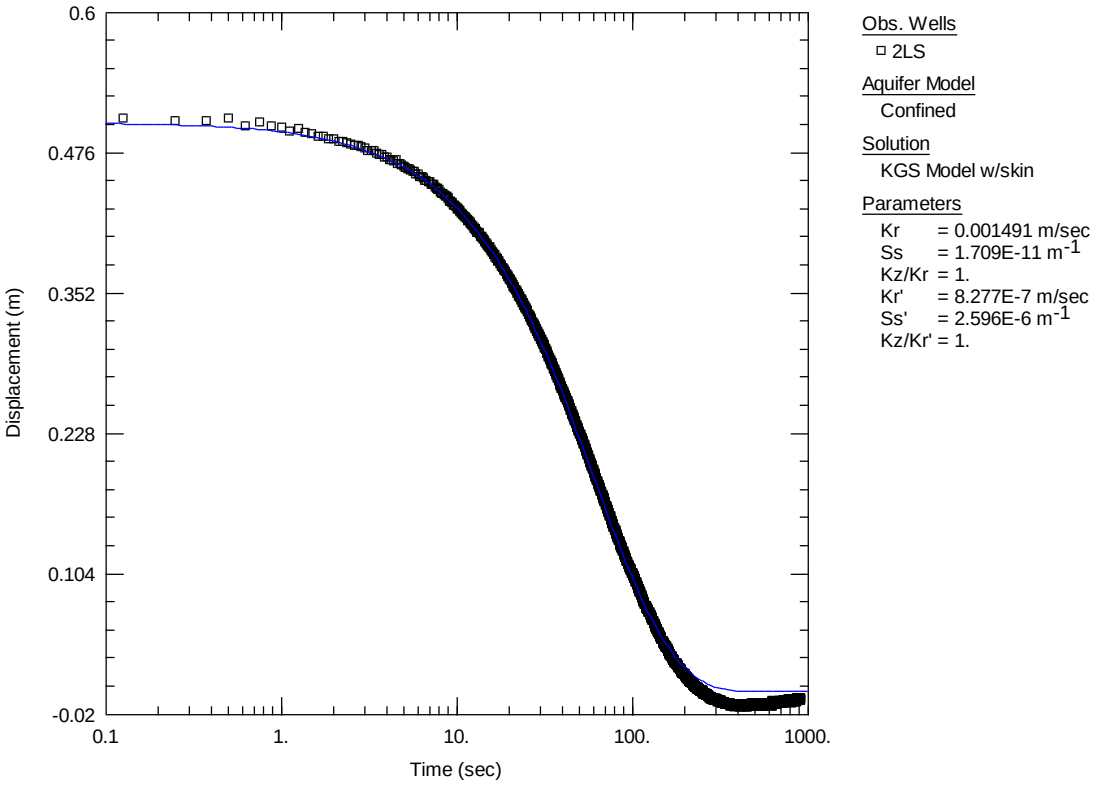

2LS Rising head with wellbore skin (convergence criteria not fulfilled):

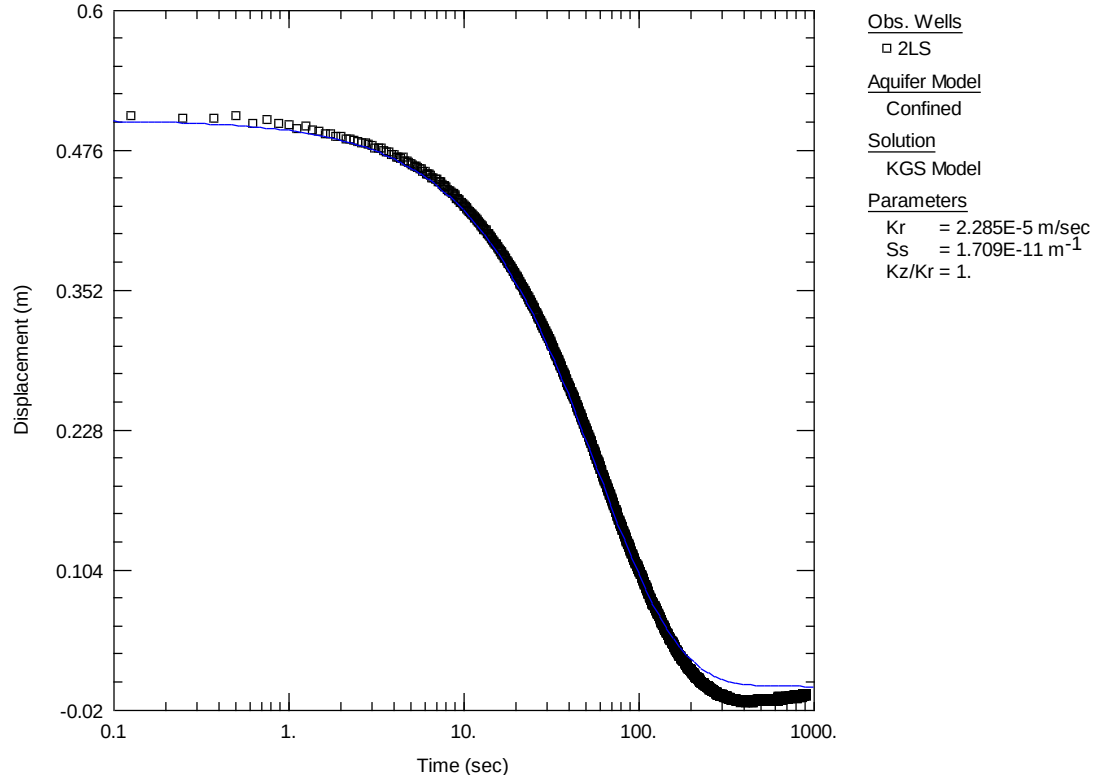

3LS Falling head:

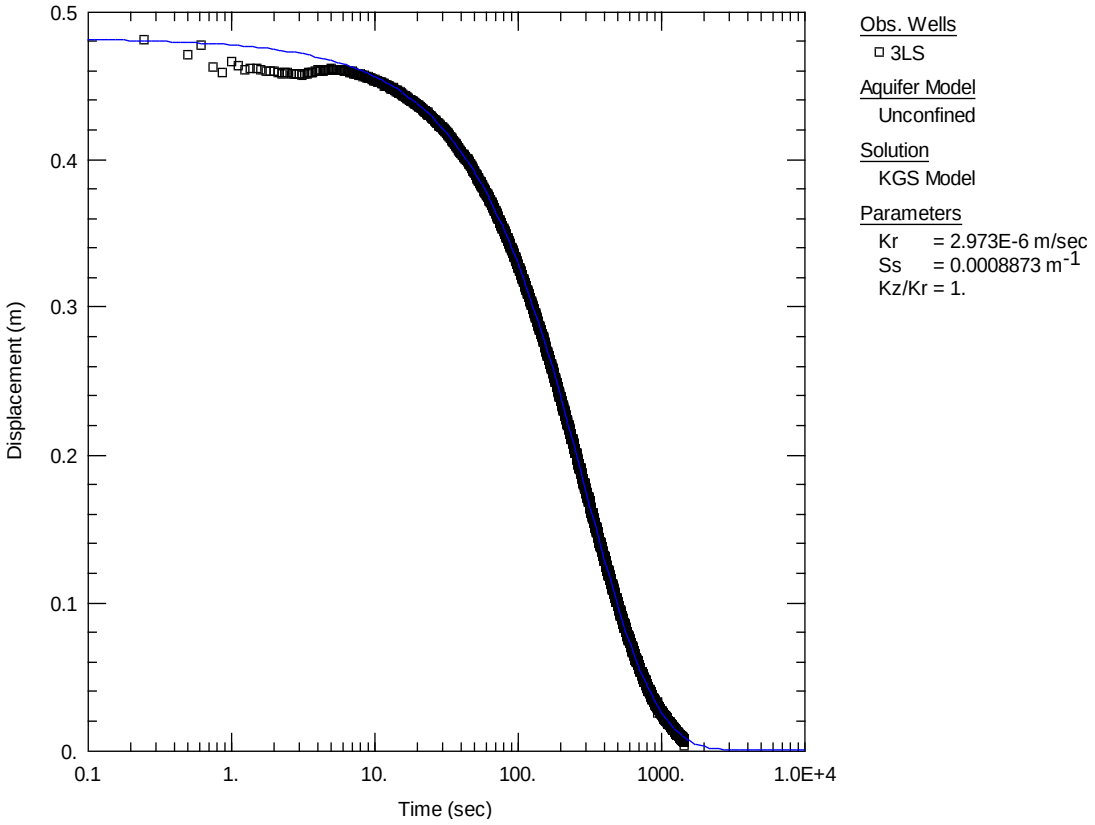

3LS Rising head:

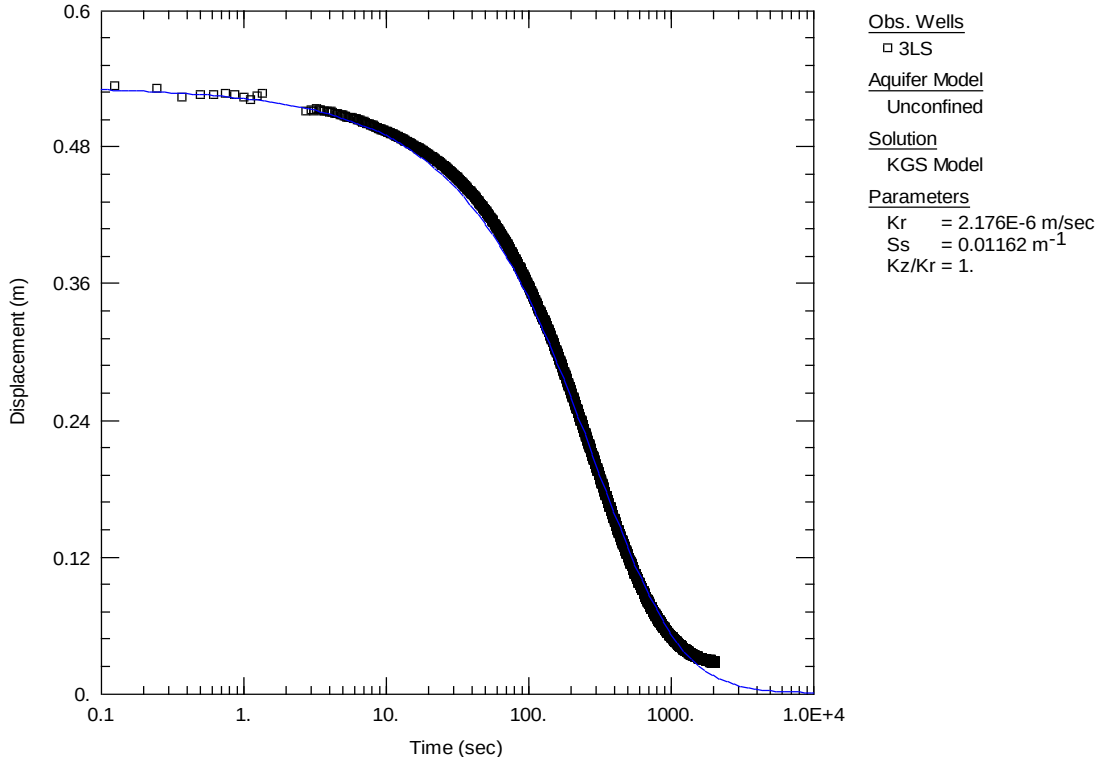

6LS Falling head KGS wellbore skin (0.5 cm thick):

6LS

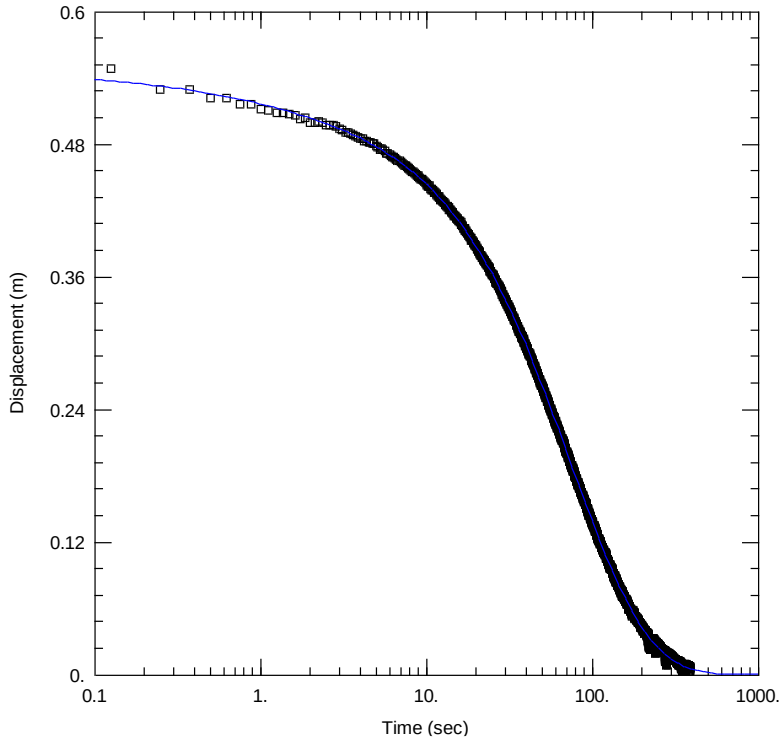

Falling head KGS without wellbore skin:

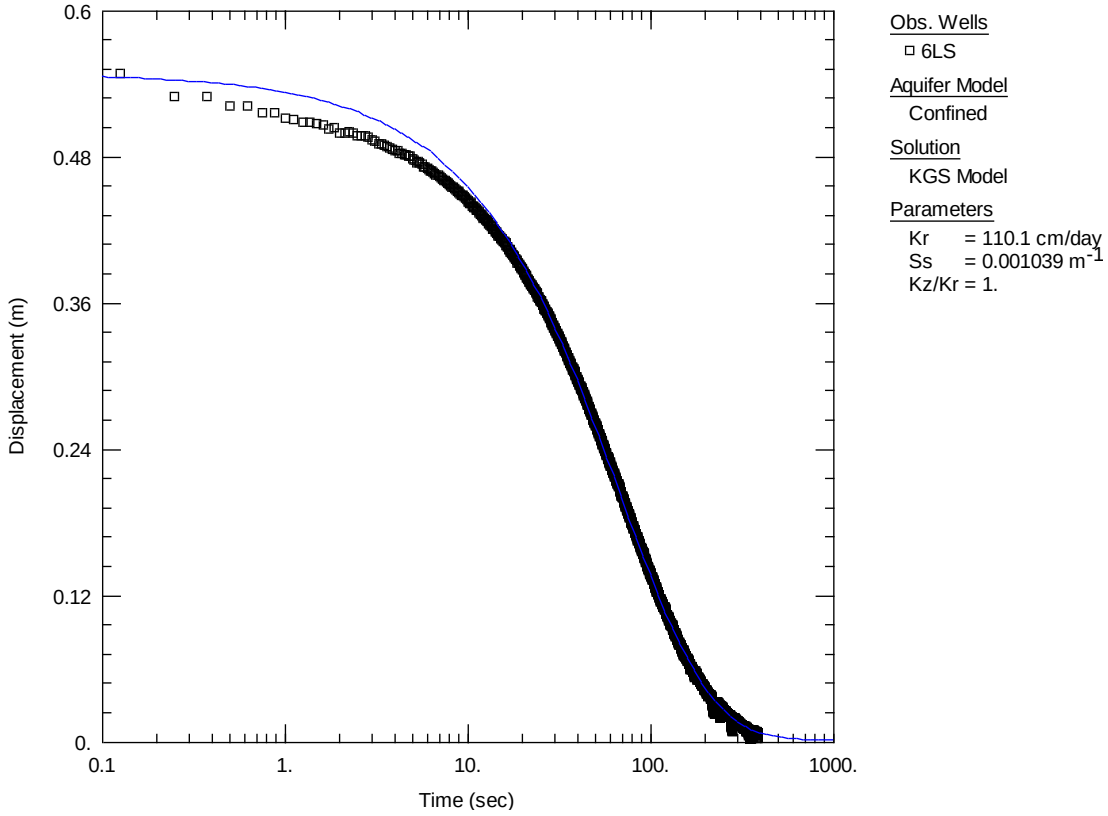

6LS Rising head KGS without wellbore skin:

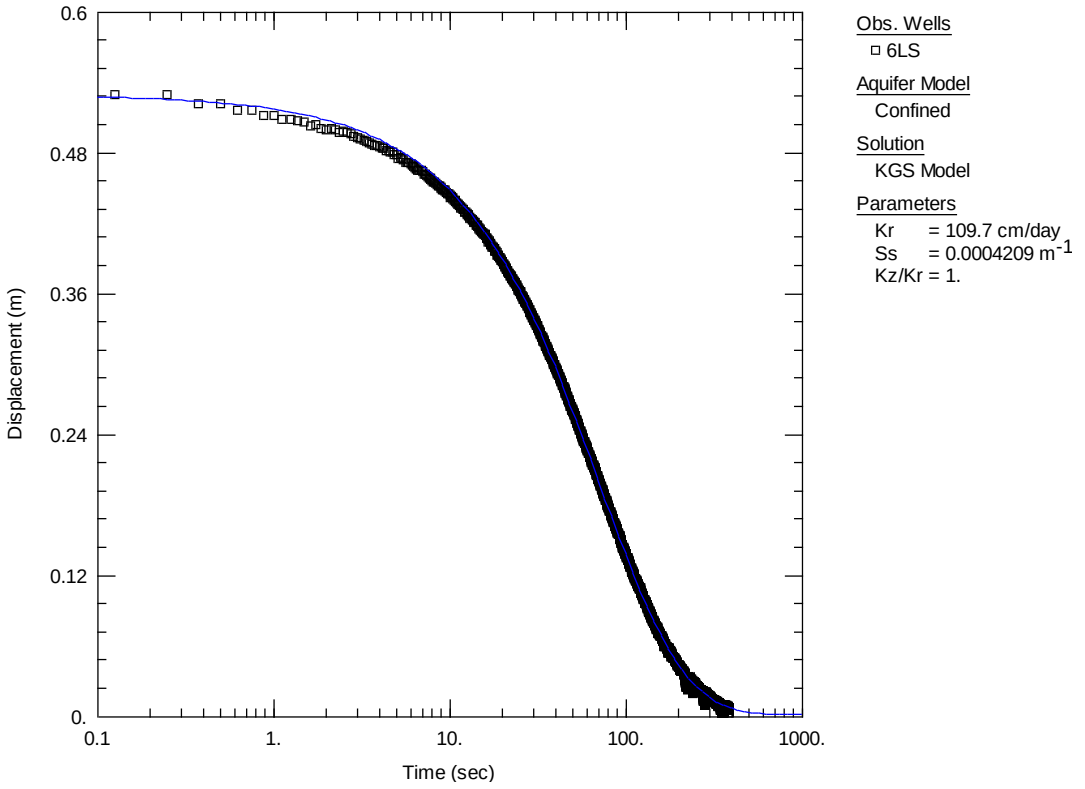

6LS Rising head KGS wellbore skin (0.5 cm):

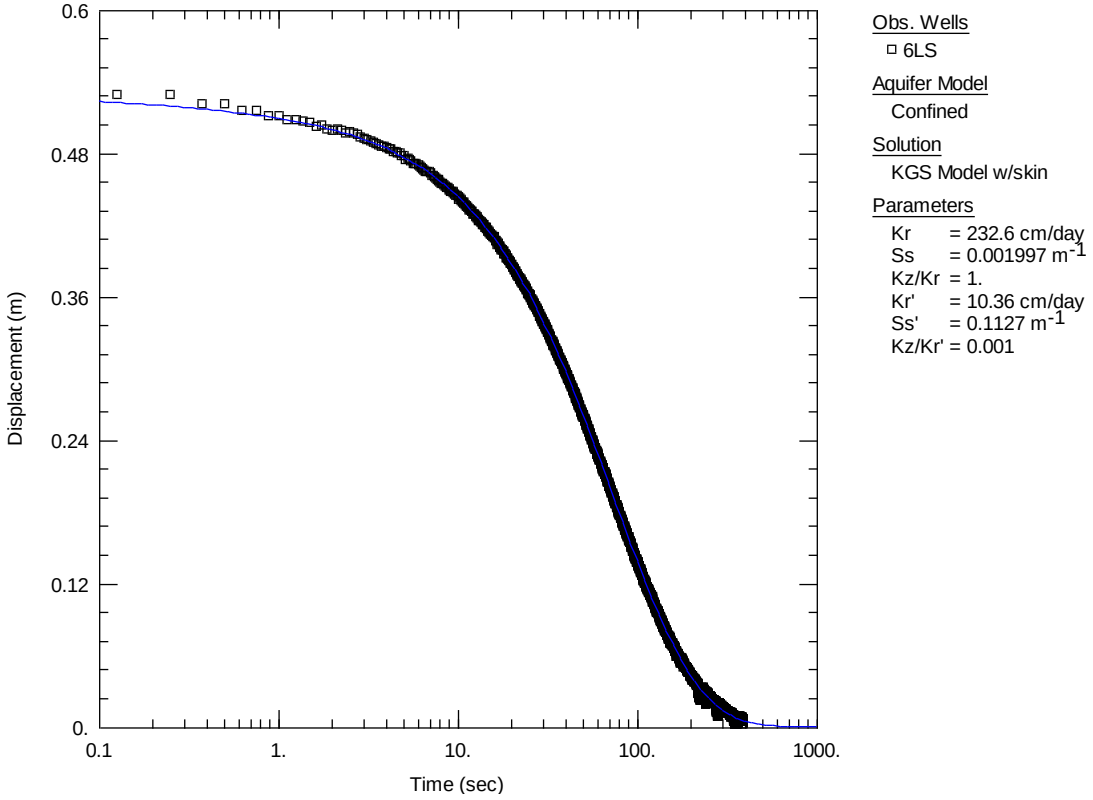

7LS Rising head wellbore skin (0.5 cm):

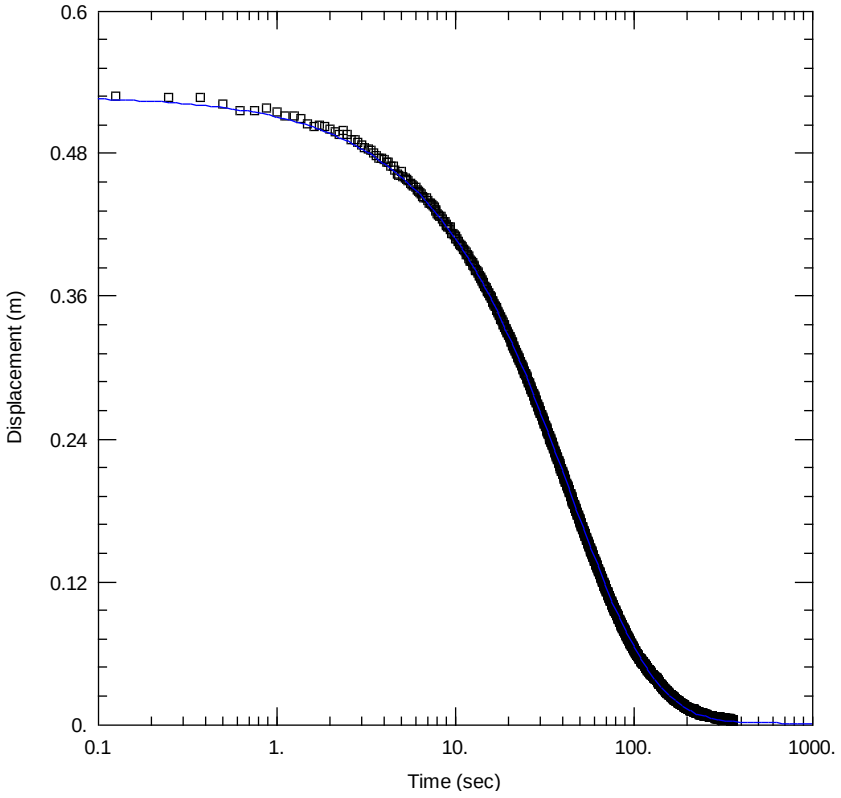

Obs. Wells
□ 7ls

Aquifer Model
Confined

Solution
KGS Model w/skin

Parameters
Kr = 235.2 cm/day
Ss = 0.001333 m^{-1}
Kz/Kr = 1.
Kr' = 31.47 cm/day
Ss' = 1.025E-10 m^{-1}
Kz/Kr' = 0.02516

7LS Rising head withhout wellbore skin:

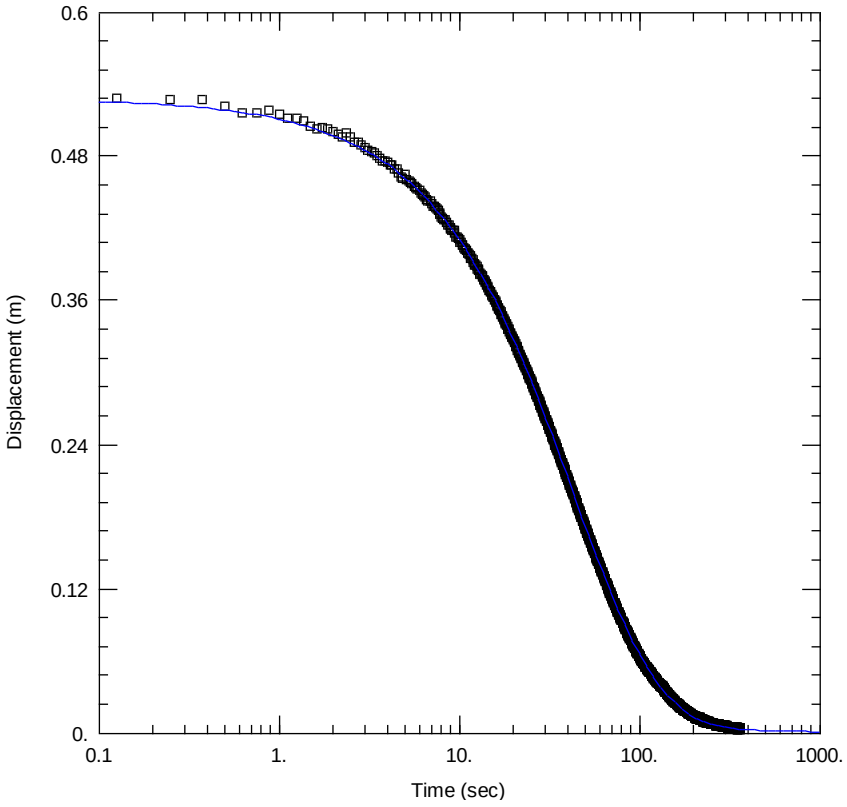

Obs. Wells
□ 7ls

Aquifer Model
Confined

Solution
KGS Model

Parameters
Kr = 183.4 cm/day
Ss = 0.0002443 m^{-1}
Kz/Kr = 1.

7LS Falling head wellbore skin (0.5 cm):

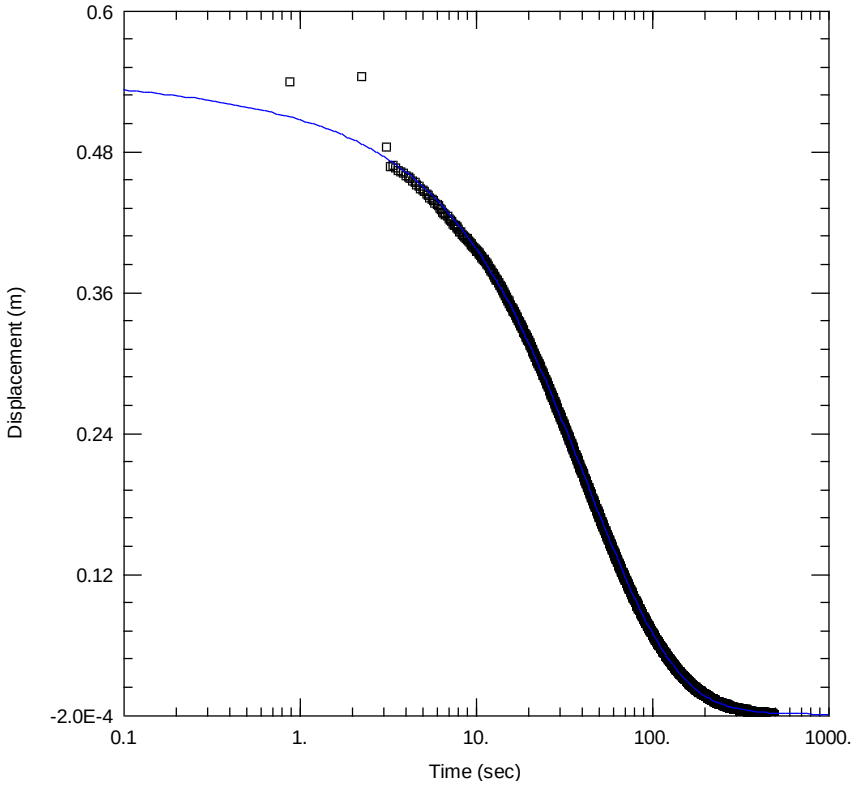

7LS Falling head without wellbore skin:

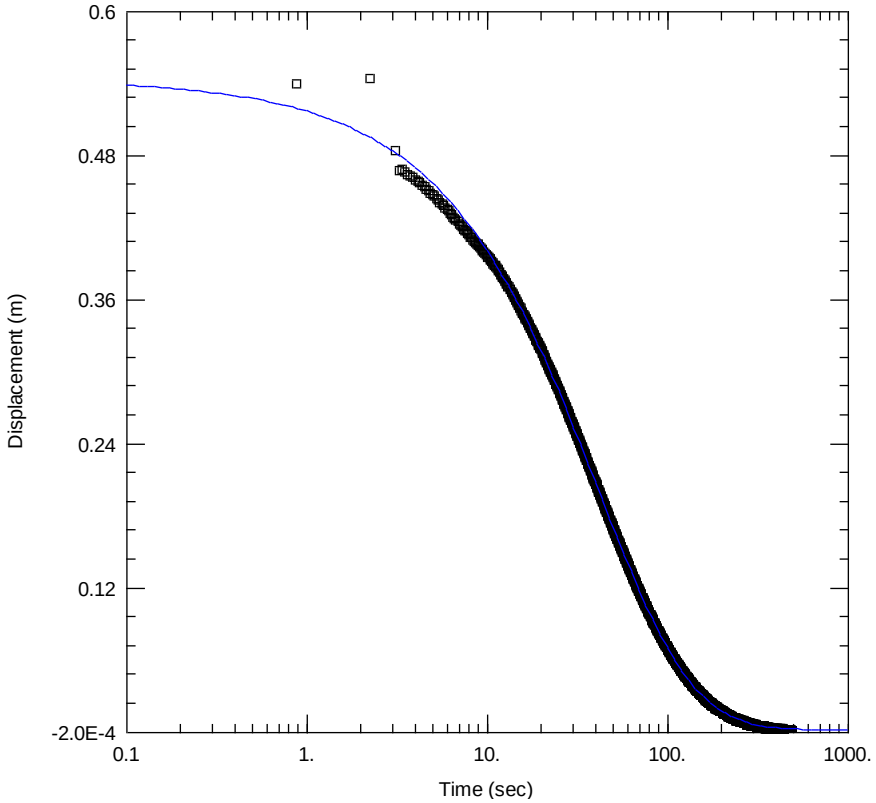

MP 8 Falling head:

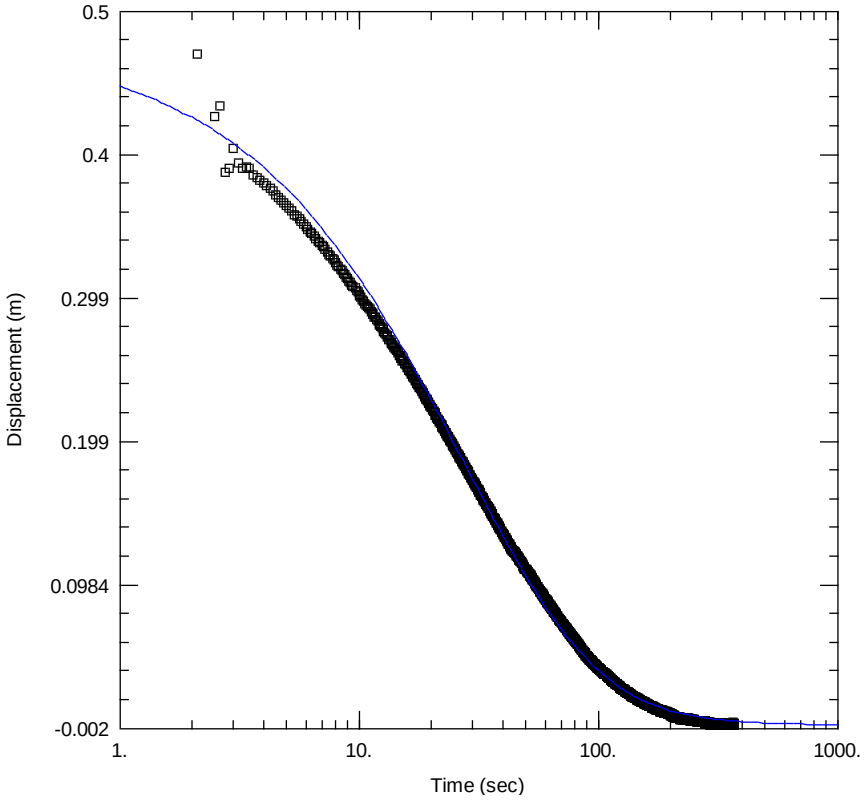

MP 8 Rising head:

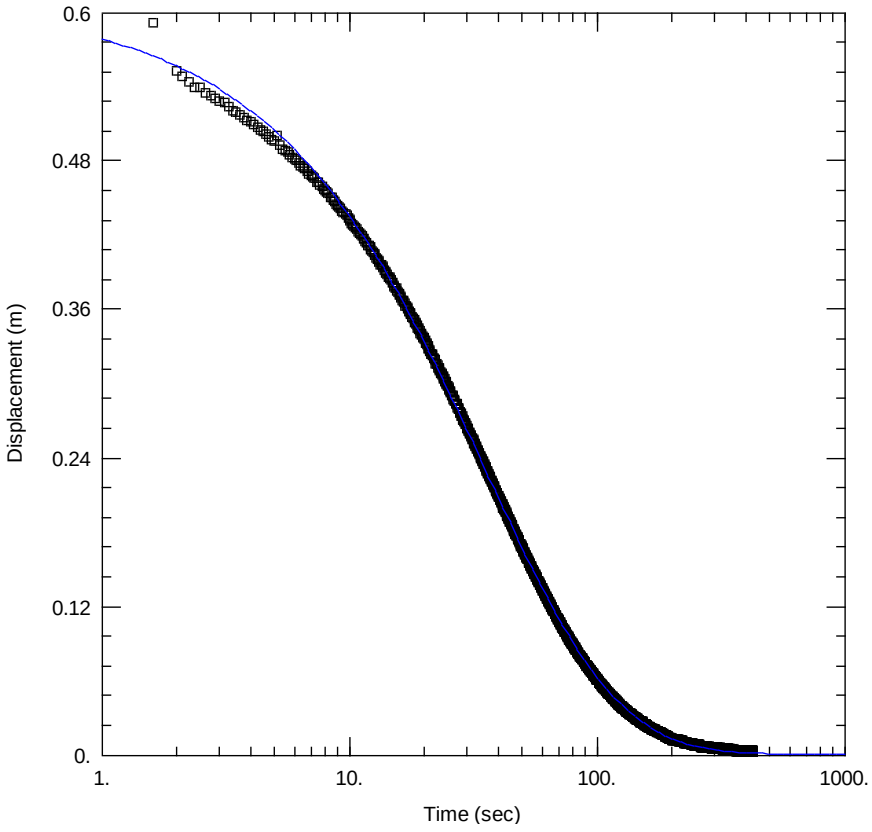

MP 9 Falling head:

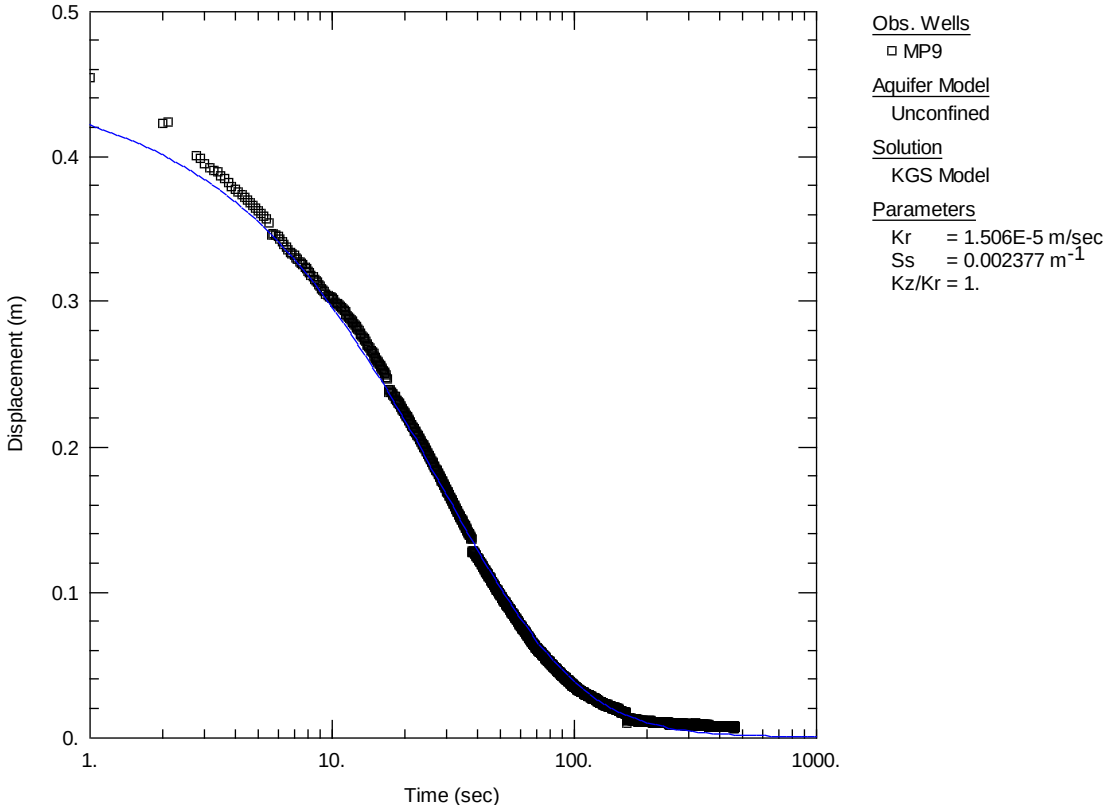

MP 9 Rising head:

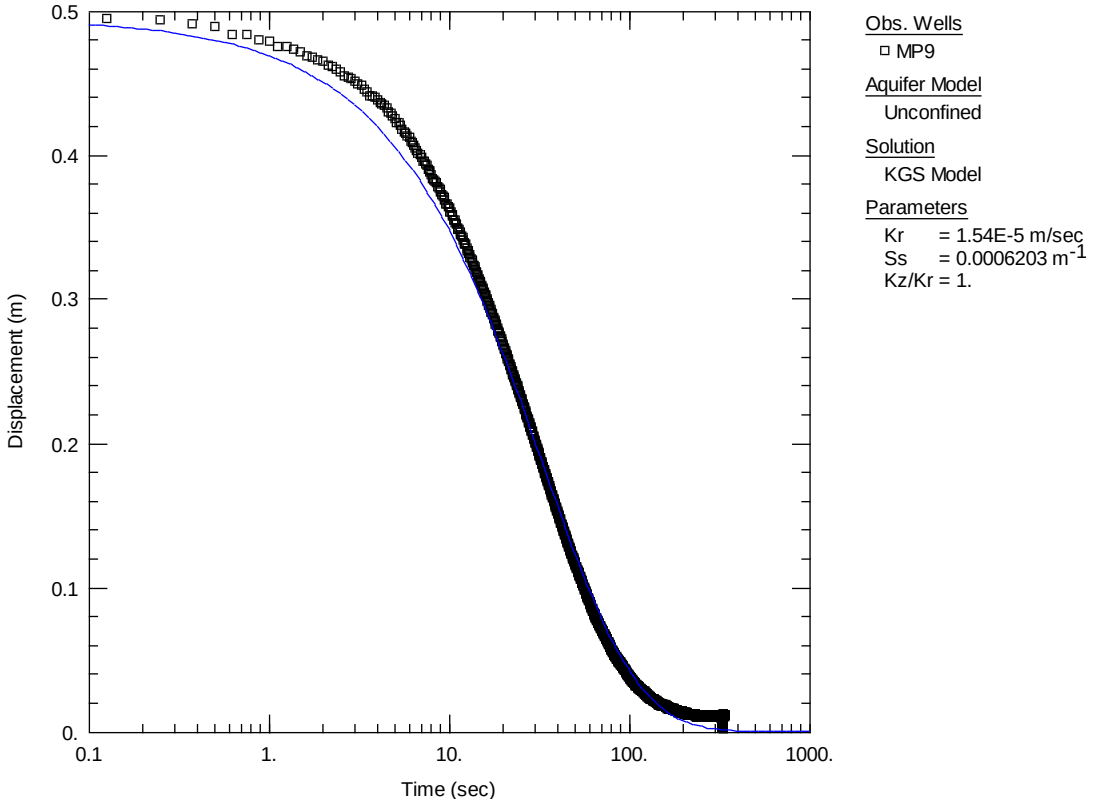

MP 10 Falling head:

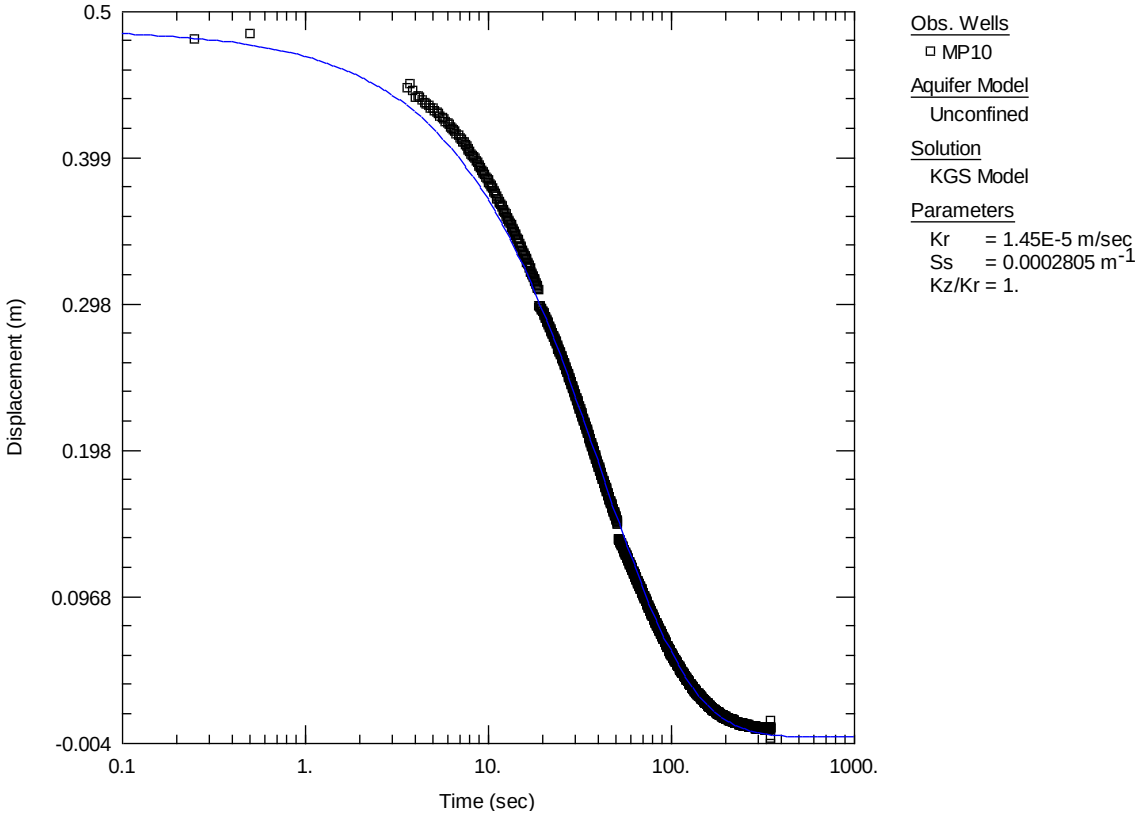

MP 10 Rising head:

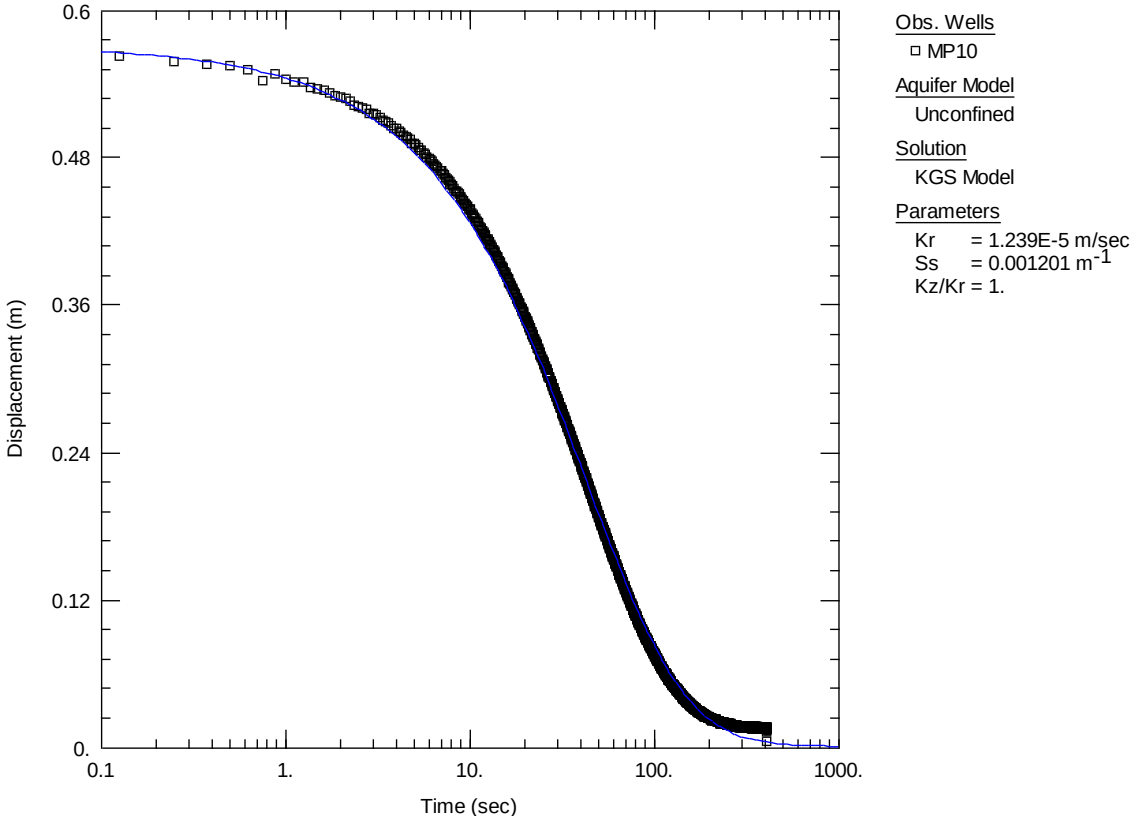

2P Falling head:

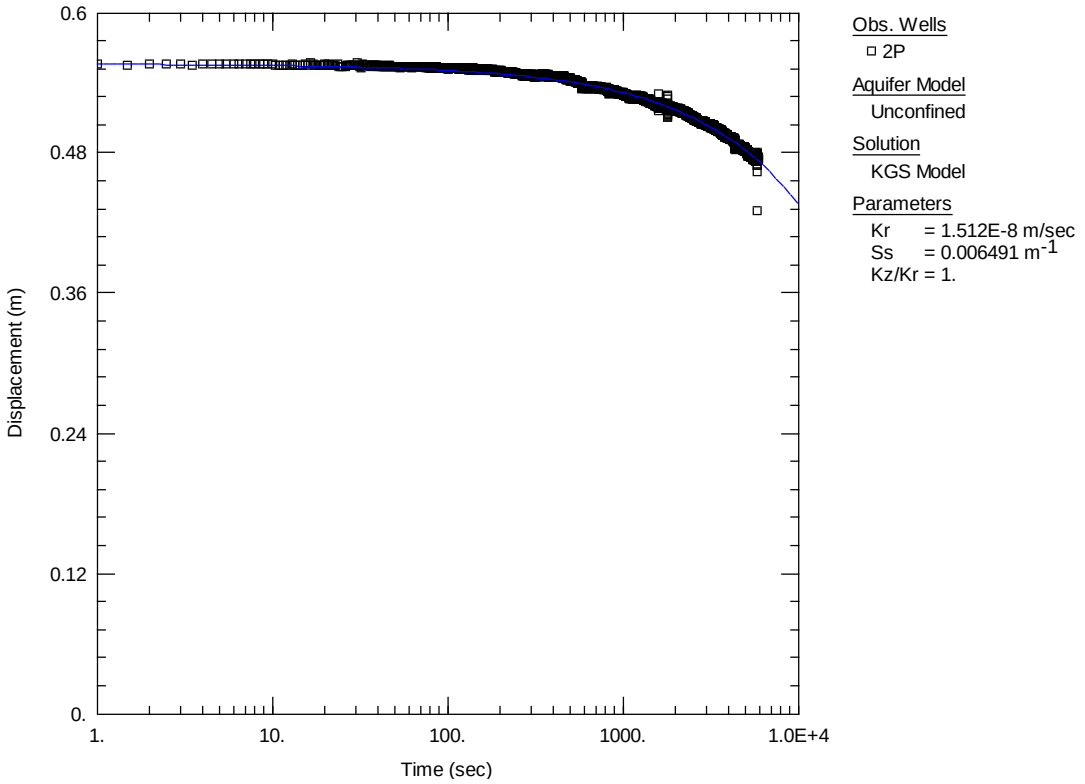

3P Falling head:

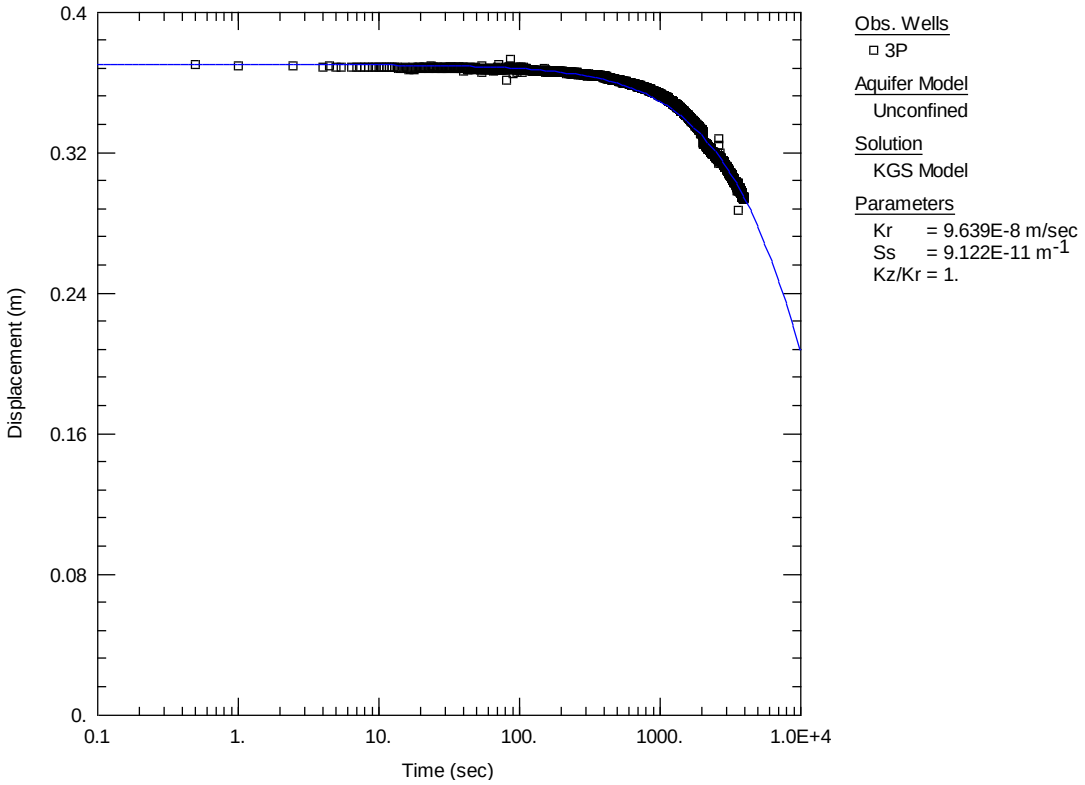

6P falling head (failed to converge):

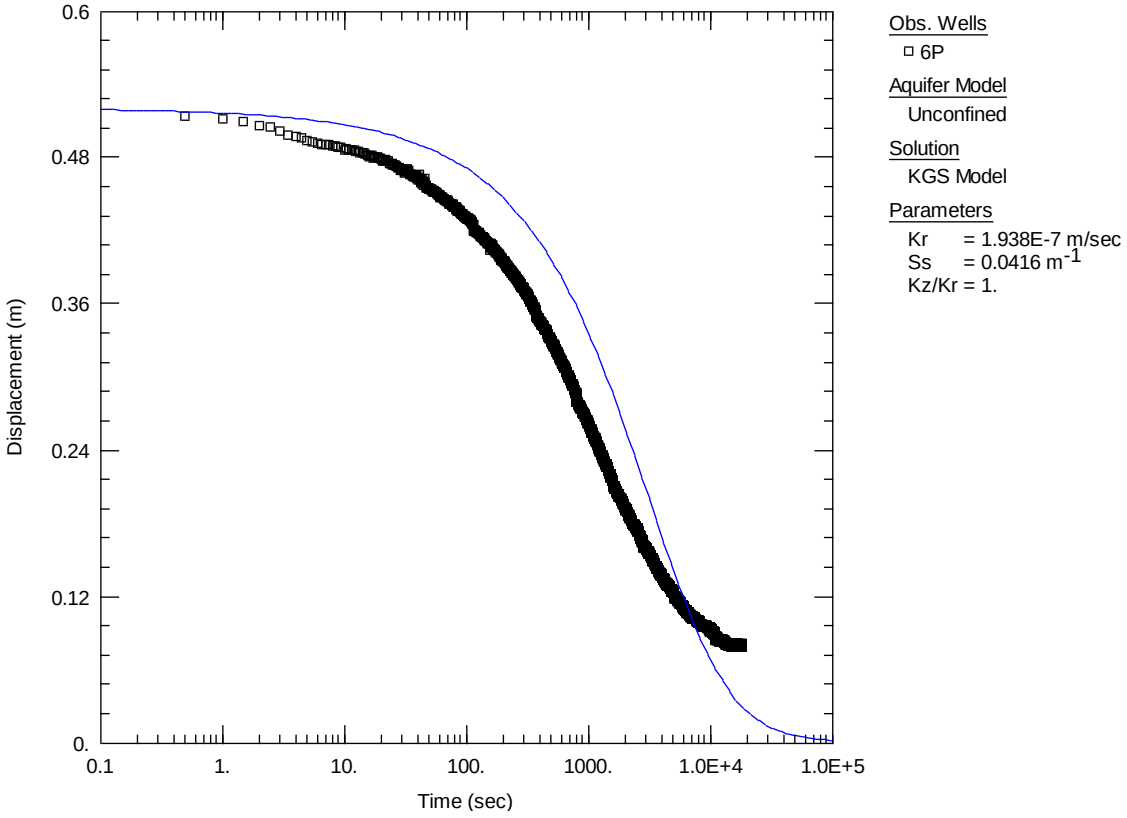

7P Falling head (failed to converge):